Understanding Polarization Distortions for Real-world Quantum Key Distribution

by

Sebastian Thomas Slaman

A thesis
presented to the University of Waterloo
in fulfillment of the
thesis requirement for the degree of
Masters of Science
in
Physics (Quantum Information)

Waterloo, Ontario, Canada, 2020

Author's Declaration

This thesis consists of material all of which I authored or co-authored: see Statement of Contributions included in the thesis. This is a true copy of the thesis, including any required final revisions, as accepted by my examiners.

I understand that my thesis may be made electronically available to the public.

Statement of Contributions

This thesis contains work done in collaboration with others but to which I made the major contribution. The contributions are listed below.

Chapter 1

Sebastian Slaman wrote the Introduction chapter.

Chapter 2

Sebastian Slaman developed the birefringence simulation model and wrote this chapter.

OHB provided FEM stress data used to develop the birefringence model.

Brendon Higgins developed the Poln function used for calculating QBER, compensation unitaries, and density matrices.

Chapter 3

Thomas Jennewein developed the core of the beam steering simulation and it was modified by Sebastian Slaman to model the optics and extract QBER.

Ramy Tannous assisted in taking characterization measurements.

Brendon Higgins developed the Poln function used for calculating QBER, compensation unitaries, and density matrices.

Youn Seok Lee developed MATLAB code used to automate the polarization measurements.

Chapter 4

Sebastian Slaman wrote the Conclusion chapter.

Abstract

The field of quantum key distribution (QKD) has seen many advancements since its conception in 1984. Recently there have been developments towards establishing free space optical links between satellites and earth to enable global QKD networks. Polarization encoded photos are commonly utilized as qubits for these free space links, placing polarization distortion constrains on the optics used.

Two polarization distortion studies were conducted in this thesis. The first is a simulation of stress induced birefringence in the Window Observational Research Facility window on board the International Space Station (ISS). Atmospherics pressure inside the ISS elicits stress on window leading to optical birefringence, which in turn can distort the polarization of photons as they pass through the window. The model studies the birefringent effects for incoming optical beams over different polarizations, diameters and incoming angles.

As part of free space optical quantum links, it can be beneficial to utilize beam steering optics to manage the spatial positioning of various components in the system. Implementing beam steering optics can aid in achieving spatial and maneuverability requirements for ground stations and satellites as they track each other. However, these optics can have an adverse effect on incoming photon polarization states. Because of this, the effects of various different beam steering configurations were characterized experimentally, and compared to a corresponding simulated model.

The studies presented in this thesis have revealed that common optics such as windows and mirrors can distort polarization based quantum signals. The polarization distortion of the studied optics have shown high dependencies on the angular orientation of the incoming optical beam. However, the distortions measured can be noticeably reduced by implementing compensation optics. As a result, their distortions are not detrimental to a quantum link that utilizes them. The studies presented in this thesis are critical to the design of polarization based quantum receivers as they shed light on potential sources of link distortions. This work is part of a large collection of developments bringing the implementation of global quantum key distribution networks closer to reality.

Acknowledgments

First off, I would like to thank Thomas Jennewein, my supervisor. He has provided me with encouragement and support throughout my masters and even before. I am truly grateful for the opportunity to work with him and to be able to benefit from his knowledge throughout the years. I would additionally like to thank the members of my Advisory Committee: Donna Strickland and Roger Melko. I appreciate the guidance they have given and time they have committed to further my learning. I would also like to thank Robert Mann for joining Roger Melko on the Examining Committee for my thesis defense.

Another thank you goes out to all the past and current members Quantum Photonics Lab for their support, advice, and encouragement. I've had a plethora of wonderful interactions throughout my time in the group and the members have helped me grow personally and academically. A thank you goes out to all members of the Fun Office, Aimee Gunther, Ramy Tannous, and Youn Seok Lee for all the support, fun, and squash. It has be a wonderful ride, and I am happy to have spent the journey with you all. I would also like to thank Aditya Srinivasan and Ramy Tannous for help proofreading my thesis.

I would like to thank the various members and staff of the Institute for Quantum Computing. They have be so very helpful in a variety of ways such as guiding me through various forms as well as making sure I have what I need like a functioning office chair. The various monthly gatherings, homework gatherings, and random hallway gatherings have been entertaining and encouraging.

Thank you to my friends near and far that have been with me in this journey. I would like to thank my fellow house-mates; Brad van Kasteren, Carl Tutton, and Zac Gingras for all the fun, games, chats, and friendship. A special thank you goes out to Lori Pollit for always putting a smile on my face, making these past few years a wonderful experience, and encouraging me along the way. I would also like to thank My parents, Michael and Linda, for all the support and love they have given me thought everything I have done. A thank you also goes out to my sisters, Jolene and Rosalind for their encouragement and spunk they add to my life.

I appreciate the support provided to me and the projects I have worked on from the following funding agencies; the Natural Sciences and Engineering Research Council of Canada, the Canadian Foundation for Innovation, the Canadian Space Agency, the province of Ontario, the University of waterloo, and the Institute for Quantum Computing.

I would also like to acknowledge the giants who came before me.

Dedication

To the future

Table of Contents

List of Figures

List of Tables

List of Acronyms and Abbreviations

A:	Anti-diagonal Polarized / Polarization
APT:	Advanced Pointing and Tracking
BB84:	Bennett and Brassard 1984 QKD Protocol
CSA:	Canadian Space Agency
D:	Diagonal Polarized / Polarization
EPR:	EinsteinPodolskyRosen
ESA:	European Space Agency
FEM:	Finite Element Method
H:	Horizontal Polarized / Polarization
HWP:	Half Wave Plate
IQC:	Institute of Quantum Computing
ISS:	International Space Station
L:	Left-circular Polarized / Polarization
QBER:	Quantum Bit Error Ratio
QEYSSat:	Quantum EncrYption and Science Satellite
QKD:	Quantum Key Distribution
QUEST:	Quantum Entanglement Space Test
QWP:	Quarter Wave Plate

R: Right-circular Polarized / Polarization

RMT: Residual Matrix Trace

UW: University of Waterloo

V: Vertical Polarized / Polarization

WORF: Window Observational Research Facility

Chapter 1

Introduction

1.1 Quantum Information

The study of quantum information is a unique field based on the premise of stripping our knowledge of science down to its core and building on what lies there, however strange it may be. Several quantum phenomena such as the Einstein-Podolsky-Rosen (EPR) paradox, Heisenberg uncertainty principal, and quantum teleportation have muddied the waters of classical physics [1–5]. These principals have often been considered a nuisance and treated as sources of noise to be designed around [6]. The field of quantum information is devoted to developing computation and communication tools based on fundamental quantum phenomena like these. One such development is quantum key distribution (QKD), which enables the sharing of secure encryption keys while minimizing the amount of information revealed to an eavesdropper [7–9].

1.1.1 Quantum Key Distribution

The concept of QKD started with Charles Bennett and Gilles Brassard in 1984 with their development of the first QKD protocol which came to be known as the BB84 protocol [7]. Since then, several other protocols for QKD have been developed including the E91 and BBM92 protocols [10, 11].

QKD has the unique ability to distribute secret encryption keys with a level of security based on the nature of reality itself. At the core of QKD, there are two fundamental phenomena of quantum mechanics; the no-cloning theorem and the Heisenberg uncertainty principal [3, 12, 13].

The no-cloning theorem states that the act of duplicating a single quantum state perturbs the original state such that the duplicated and original states are not identical. Because of this, a quantum state can not be truly copied.

A proof of this principal is presented as follows. Suppose there exists a unitary operator ($\boldsymbol{U}$) that can copy the state of a qubit ($|\boldsymbol{\phi_n}\rangle$) onto another 'blank' qubit ($|\boldsymbol{\psi}\rangle$). This operator is required to function correctly on any unknown state. For this example it will attempt to copy two different states, $|\boldsymbol{\phi_1}\rangle$ and $|\boldsymbol{\phi_2}\rangle$, as shown in Equations 1.1 and 1.2.

$$U(|\phi_1\rangle \otimes |\psi\rangle) = |\phi_1\rangle \otimes |\phi_1\rangle \tag{1.1}$$

$$U(|\phi_2\rangle \otimes |\psi\rangle) = |\phi_2\rangle \otimes |\phi_2\rangle \tag{1.2}$$

If these equations hold true, the inner product of the resulting states should also be identical to the inner product of the operator and states before copying, as shown in equation 1.3.

$$(U(|\phi_1\rangle \otimes |\psi\rangle))^\dagger \cdot U(|\phi_2\rangle \otimes |\psi\rangle) = (|\phi_1\rangle \otimes |\phi_1\rangle)^\dagger \cdot (|\phi_2\rangle \otimes |\phi_2\rangle) \tag{1.3}$$

$$\langle\phi_1|\phi_2\rangle \langle\psi|\psi\rangle = \langle\phi_1|\phi_2\rangle \langle\phi_1|\phi_2\rangle \tag{1.4}$$

$$\langle\phi_1|\phi_2\rangle = \langle\phi_1|\phi_2\rangle^2 \tag{1.5}$$

Therefore, for the copying operator to exist, Equation 1.5 would also hold true, meaning that $\langle\boldsymbol{\phi_1}|\boldsymbol{\phi_2}\rangle$ must be either 0 or 1. If it is zero, the states must be orthogonal and if it is one, they must be identical. As stated earlier, the cloning operator must function on any arbitrary state. This means that it should be able to function even if $|\boldsymbol{\phi_1}\rangle$ and $|\boldsymbol{\phi_2}\rangle$ are not identical and not orthogonal. This would invalidate Equation 1.5, proving a copying operator can not exist, therefore a quantum state cannot be duplicated, affirming the no-cloning theorem.

The Heisenberg uncertainty principal states that the there is a natural level of uncertainty inherent in a particle's position and momentum. More specifically, the standard deviation of the particle's possible position ($\boldsymbol{\sigma_x}$) and momentum ($\boldsymbol{\sigma_p}$) are related such

that reducing the uncertainty associated with one, increases the uncertainty of the other. This is more formally depicted as Equation 1.6, where $\boldsymbol{\hbar}$ is the reduced Planck's Constant.

$$\sigma_x \sigma_p \geq \frac{\hbar}{2} \tag{1.6}$$

This uncertainty relation is not limited to only the position momentum pair of observables. It also applies to any pair of complimentary particle properties such as the polarization state of a photon in two orthogonal bases.

1.1.2 Polarized Photons as Qubits

QKD, and the field of quantum information in general, utilizes quantum bits (qubits) to store and represent information, similar to how a digital computer would use bits. A classical bit can either be a 0 or 1, where as the qubit state can have a value of 0, 1 or any complex number in between. These intermediary states are described as being in a superposition of various degrees between 0 and 1. To represent this, a qubit ($|\boldsymbol{\phi}\rangle$) is described as being composed of portions of the $|0\rangle$ and $|1\rangle$ states as presented in Equation 1.7.

$$|\phi\rangle = \alpha\,|0\rangle + \beta\,|1\rangle \tag{1.7}$$

The values of $\boldsymbol{\alpha}$ and $\boldsymbol{\beta}$ are any complex value such that $|\alpha|^2 + |\beta|^2 \leq 1$, and therefore the probability of any measurement is less than or equal to 1. A qubit exists in this superposition state until it is disturbed by a process such as a state measurement. The probability of $|\boldsymbol{\phi}\rangle$ being measured as a $|0\rangle$ or $|1\rangle$ state is $|\alpha|^2$ and $|\beta|^2$ respectively.

The Bloch sphere is a way to geometrically represent and visualize a pure qubit state [14]. It consists of a units sphere with radius 1, and 3 sets of antipodal points on the surface each located along one of the Cartesian axes originating from the sphere's centre. The points that lie along the the +Z and -Z axis correlate with the $|0\rangle$ and $|1\rangle$ states respectively. In this formalism, a state is defined a vector originating form the sphere's centre and pointing outwards, shown as the blue vector in Figure 1.1. Quantum states are described as being either pure or mixed, which have various connotations discussed later as required. The difference between these two state types is based on the length of a qubit's state vector. A pure state qubit is defined as a vector of length 1 and an impure state is represented as having length less than 1. For the sake of simplicity in this thesis, states are assumed to be pure in this thesis unless specifically detonated.

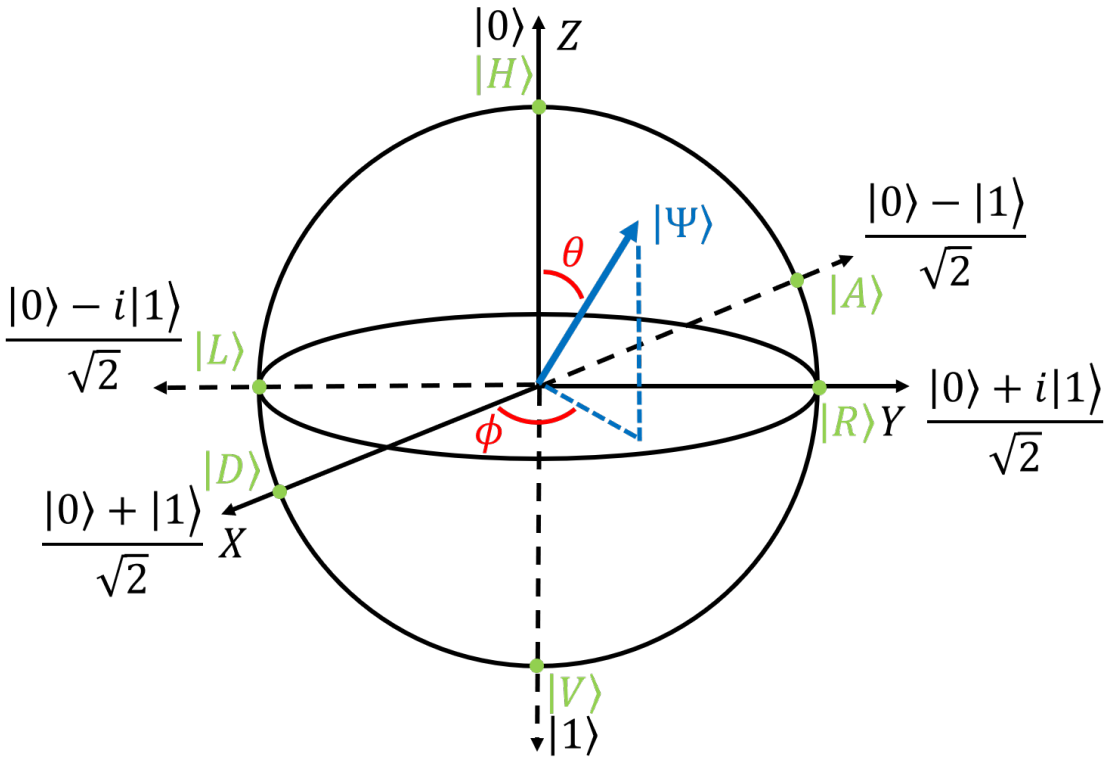

Figure 1.1: *Bloch sphere with Poincaré sphere overlay*

In the Bloch sphere representation, $\boldsymbol{\alpha}$ and $\boldsymbol{\beta}$ are commonly defined for pure states as given in Equation 1.8.

$$\alpha = \cos(\theta/2), \quad \beta = e^{i\phi}\sin(\theta/2) \tag{1.8}$$

For each state on the Bloch sphere there exists an orthogonal state positioned antipodal to the first. For an arbitrary qubit vector, the probability of it being measured in the orthogonal state is equal to one minus the probability of it being measured in the primary state. Because of this unique opposition, these two state positions define what is known as a basis. A common example of this is the $|0\rangle$, $|1\rangle$ basis. Two bases that are perpendicular to each other are referred to conjugate bases. A state aligned in one of these bases has an equal probability of being measured in either state of the other basis. As shown on the Bloch sphere in Figure 1.1, there exist a set of 3 conjugate bases along the Cardinal axes. These 3 conjugate bases are commonly used in quantum mechanics to assign meaning to and quantify qubit orientations.

There exists an infinite number of possible 3 conjugate bases sets. However, the bases existing along the Cardinal axes are commonly used due to their simplicity.

Photons, individual quanta of light, abide by the no-cloning theorem and uncertainty principal and are suitable qubits for QKD. Additionally, photons travel at the speed of light making them appropriate for rapid communication. For these reasons and others, QKD protocols are most commonly implemented using photons as qubits to encode and transmit information. There are several other possible methods for encoding photon qubits with information for QKD such as phase, frequency, and time-bin; however, this thesis focuses on polarization state encoding [15–18].

The Cardinal basis states on the Bloch sphere correlate well with the polarization states of the Poincaré sphere used to describe a photon's possible polarization states. The Poincaré sphere's basis states are given in green overlaid on the Bloch sphere in Figure 1.1, showing their association with the Bloch sphere qubit depiction. For the sake of completeness, it is important to state that the Bloch sphere and the Poincaré sphere can be considered functionally identical with respect to photon polarization qubit. The 3 conjugate bases defined on the Poincaré sphere are based on the standard 6 polarization states: horizontal $|H\rangle$, vertical $|V\rangle$; diagonal $|D\rangle$, anti-diagonal $|A\rangle$; right-circular $|R\rangle$, left-circular $|L\rangle$.

1.1.3 BB84 Protocol

The BB84 protocol is based on the sharing of randomized qubit states from one node (Alice) to another (Bob) such that they can generate a string of bits, referred to as a key, known by only them [7]. The process uses quantum mechanics to minimize the amount of information about the key available to an eavesdropper (Eve). This shared secure key can then be used to encrypt messages so Alice and Bob can exchange private information.

The BB84 protocol can be performed with any type of qubit, however, in this example, polarized photons are uses. Two different bases are required by the protocol. For simplicity, the Rectilinear and Diagonal polarization bases are used in this example. The common polarization bases are given in Table 1.1 for reference.

Table 1.1: The common polarization bases

Basis	0 Bit State	1 Bit State
Rectilinear	Horizontal, $\|H\rangle$	Vertical, $\|V\rangle$
Diagonal	Diagonal, $\|D\rangle$	Anti-diagonal, $\|A\rangle$
Circular	Right-circular, $\|R\rangle$	Left-circular, $\|L\rangle$

After the bases are chosen and bit values are assigned to the orthogonal states in each bases, Alice and Bob can perform the protocol for each photon as follows:

1. Alice randomly selects one of the two bases and a bit to send without knowing which basis Bob will choose. For the sake of this thesis, Alice does so with an equal probability of choosing each basis and each bit, but this is not strictly required.
2. Alice records the bit and basis she selected.
3. Alice then prepares her qubit for transmission by polarizing a photon appropriately.
4. Similarly, Bob randomly chooses a basis in which to measure the photon without knowing which basis Alice chose. He does so with equal probability for each basis, but this is not strictly required.
5. Bob records the basis he selected.
6. Alice transmits the prepared photon.
7. Bob measures the received photon in his chosen basis and records the binary result.
8. Alice and Bob publicly share which basis they used to prepare and measure the photon in.
   (a) If Alice and Bob happened to randomly select the same basis, they keep their binary result and add it to their shared string of bits also known as the sifted key.
   (b) If the basis differ, the bits are discarded because Alice's and Bob's bits are liable to be different as measuring the photon in the incorrect basis will give a random result.

This process is repeated multiple times to populate the sifted key until it is a desirable length. Afterwards, the protocol enters what is know as the classical post processing stage. If there were no disturbances or errors in the photon's transmission and measurement, then Alice and Bob would have identical sifted keys.

Because it is physically impossible to copy the unknown state Alice sends, an eavesdropper, Eve, is forced to make a measurement in the attempt to read and duplicate the photon. To do so, she would intercept the photon between steps 6 and 7 mentioned earlier, and implement a protocol like the following:

1. Eve selects a basis to measure the photon in as she desires, but since she does not know what basis Alice or Bob has selected, her choice can be considered effectively random.

2. Eve then intercepts Alice's transmitted photon and measures it in the basis Eve selected and records the result. Since her basis is not correlated with Alice's the result Eve obtains will be a random half of the time.

3. Based, on her measured bit and basis, Eve appropriately prepares another photon and transmits it to Bob.

Because of Eve's actions on the photon channel, the photons Bob receives would sometimes have a different polarization than what Alice sent causing discrepancies in the sifted key. To test for this, Alice and Bob would share a portion of the sifted key and delete that portion from the final key. By doing so, they can estimate what percentage of their bits disagree. This is commonly referred to as the quantum bit error ratio (QBER).

When Eve intercepts a photon, she has a 50% chance of measuring the photon in the incorrect basis. For each intercepted photon measured in the incorrect basis, Eve sends Bob a photon polarized in the wrong basis. As a result of this, he would have a 50% chance of measuring the photon randomly collapsing to the same polarization Alice sent when he measures the photon.

Because of this, if Eve is intercepting and measuring every bit, the shared string of bits between Alice and Bob would have bit error ratio of 25%. By measuring the QBER, Alice an Bob can therefore determine if Eve was listening in on them, and know know their shared key was insecure and discard it.

If the QBER measured by Alice and Bob is zero, then they know that no one was eavesdropping on them and they can use their shared key to classically encrypt their

information. This encryption can be done using what is known as a one-time-pad or Vernam cypher, which is proven to be secure as long as the key is purely random and only known to the sender and receiver [19] [20].

Due to physical imperfections of the photon's transmission and measurement, the photon may experience polarization distortion. As a result of this, the channel's measured QBER will not be zero even if there are no eavesdroppers. Because of this inherent QBER, the keys Alice and Bob have will not be completely identical. There are classical bit correction methods to remove the discrepancies between the keys; however, this process is not perfect and can result in the leaking of information to Eve [21]. This process comes at the additional cost of reducing the secure key length shared by Alice and Bob [21, 22]. These corrections are performed in what is know as the classical post processing stage of the protocol.

If the natural QBER is too high, the key generation rate can be significantly reduced making it impossible to generate a secure key [23]. If the natural error rate is high, it can also mask some eavesdropping attempts as Eve can choose to only look at a portion of photons gaining some information about the key. She can therefore keep the QBER low enough such that the errors she causes do not seem abnormal. Because of these reasons, it is important for QKD implementations to minimize the channel's naturally induced QBER.

1.1.4 Quantum Bit Error Ratio

Quantum Bit Error Ratio (QBER) is the probability of one input quantum state being measured as the opposite state and therefore resulting in an error as presented in Equation 1.9 [22]. For the QKD scheme used in this thesis, QBER would correspond to the sent polarization being measured as the opposite polarization in the same basis. Therefore, any polarization distortion will inherently effect the QBER.

$$QBER = \frac{P_{error}}{P_{error} + P_{correct}} \tag{1.9}$$

Mathematically, the QBER for a given state, $|\boldsymbol{\psi_n}\rangle$, transmitted through a system $\boldsymbol{M}$ is more rigorously defined in Equation 1.10 where $|\boldsymbol{\psi_o}\rangle$ is the orthogonal polarization in the same basis.

$$QBER = \langle\psi_n| M |\psi_o\rangle \langle\psi_o| M |\psi_n\rangle \tag{1.10}$$

The QKD protocol discussed in this thesis utilizes $|\boldsymbol{H}\rangle$, $|\boldsymbol{V}\rangle$, $|\boldsymbol{D}\rangle$ and $|\boldsymbol{A}\rangle$ polarization states. As a result, the mean QBER for an implementation of this protocol is taken by averaging the QBER over all the input states each state. The total system QBER is then defined as Equation 1.11.

$$QBER = \frac{\langle V| M |H_{in}\rangle \langle H_{in}| M |V\rangle}{4} + \frac{\langle A| M |D_{in}\rangle \langle D_{in}| M |A\rangle}{4} + \frac{\langle H| M |V_{in}\rangle \langle V_{in}| M |H\rangle}{4} + \frac{\langle D| M |A_{in}\rangle \langle A_{in}| M |D\rangle}{4} \tag{1.11}$$

In this definition, each input state QBER is evenly weighted by a factor of one quarter. This is because the protocol is based on the assumption that each state is transmitted through the system with the same probability. Other protocols may have non-uniform distribution of states and in those cases the weighting factors in Equation 1.11 would need to be adjusted accordingly.

Ideally, the optics used to process the photonic states do not distort the polarization, however, in the real world natural optical errors and imperfections exist. Having some amount of QBER can be acceptable; however, the higher the QBER, the lower the secure key generation rate will be.

A theoretical threshold of roughly 11.5% for the entire communication channel exists as the maximum about of acceptable QBER in order to functionally generate a secure key [23]. However, a system with a QBER near the threshold would generate secure key extremely slowly. For a QKD implementation, the practical QBER limit is less than the theoretical. This is due to a verity of effects, such as finite key length [24]. For practical implementations, this limit is estimated to be around 7% for a channel based on experimental data from table 2 in the paper by Bourgoin et. al. [24]. This limit is an estimate, and is highly dependent on the QKD implementation, as such, there is no definite answer for the practical QBER limit.

The 7% experimental QBER limitation is placed on the channel as a whole. Since a channel is composed of multiple different error sources, the QBER limit for each component needs to be much less than 7%. In the context of this work, we defined a maximum threshold of 1% QBER for any component in the system.

1.1.5 Global QKD network

Implementations of QKD in its various forms have existed and been improved upon over the past 30 years [25–30]. QKD has developed from just being able to share keys at less

than a thousand bits in a key distribution session, to over 1.79 Mbit/s [25, 28]. The growth and maturation of QKD has brought it closer to widespread implementation, and towards the development of a global quantum secure network.

There is a strong limitation that plagues QKD implementations and hinders global connections. All QKD systems are limited as to how far they can feasibly transmit the qubit states [31]. There have been various developments that have pushed these distance limits to 144km and 404km via free space and optical fibre respectively [27, 29]. However, at these distances, the signal loss is significant enough that the length of secure key that can be generated is drastically reduced, limiting the practicality of these implementations.

To feasibly implement a global QKD network, QKD implementations need to maintain high qubit exchange rates at long distances. One way to do so is by utilizing quantum repeaters to extend the operational distance of QKD network [32]. However, there are various technical matters, such as their low efficiencies, that need to be dealt with to see their use in a practical setting [33, 34]. Alternatively, instead of performing QKD directly between two earthbound nodes, satellite based quantum links can be implemented to extend the range of QKD [34–36].

Satellite-to-ground QKD was recently achieved boasting a range of up to 1,200 km at a rate of 1.1 kbit/s [37]. This bit rate is 20 orders of magnitude greater than a theorized link of the same distance made over an optical fibre. Due to the orbiting nature of the satellite, it can act as a relay to distribute quantum secure keys between various global locations [38]. This development demonstrated the feasibility of satellite based QKD, and is a step towards the development of a global QKD network.

1.1.6 QEYSSat, Ground To Satellite QKD

The aforementioned satellite QKD scheme is based on a downlink system, however uplink QKD is also feasible [34, 36, 37, 39]. For a downlink system, the signal originates from the satellite and is transmitted down towards the ground station, and for an uplink scheme, it is reversed. Each scheme has its own advantages and disadvantages. A QKD uplink keeps complex single photon sources and data processing on the ground, reducing the satellite cost and allowing for the implementation of multiple different technological photon sources [40]. For instance, weak coherent pulses and entangled sources could be utilized at a ground station with the same satellite hardware [34]. The downlink scheme benefits from reduced photon loss and lower detector dark counts [39, 41]. The expected key generation rate is greater for the downlink than the uplink [39, 42]. This difference is expected to be less than

one order of magnitude. The development of an uplink QKD system is a technologically valid approach as this level of key generation rate reduction is not detrimental.

The Quantum EncrYption and Science Satellite (QEYSSat) mission is a proposed microsatellite, funded primarily by the Canadian Space Agency (CSA). The QEYSSat mission (currently under development) is designed to implement a QKD uplink system [34]. The system consists of two main sub-systems, the ground station, where quantum source resides, and the satellite that caries the detector array. As the satellite passes over the ground station during orbit, the quantum source and detector array are oriented to face each other, such that the 785nm quantum uplink beam reaches the detector array, and the link is maintained [34, 43].

There have been a series of design and research undertakings performed by the Jennewein research group working to accomplish the QEYSSat mission. A short QKD link was established in the lab that emulated the uplink, including information processing restrictions and photon losses [39]. Outdoor QKD experiments were run between a ground station and moving receiver for a proof of concept and to test the system's tracking capabilities [44]. Furthermore, a QKD session was established between a ground station and a airborne receiver that modeled satellite passes with airplane flybys [43]. This series of experiments implemented sources, receivers, and other equipment akin to what would be used in a ground-to-satellite QKD link.

1.2 Polarization Physics

The polarization of light is defined by the oscillations of its electric field over time [45]. These oscillations occur in the plane transverse to the light beam's direction of travel. Monochromatic light is composed of two orthogonal electric field components that oscillate in a sinusoidal fashion [45]. Based on the phase of these two oscillations, the resulting net electric field vector travels a set path in the transverse plane as the light propagates. The polarization is commonly identified as linear, circular, or elliptical, which are ways to describe the path taken by the net electric field vector.

Light can have any polarization as defined by its electric field, but there are six common polarization states as mentioned in Section 1.1.2. There are four linear polarizations; horizontal (H), vertical (V), diagonal (D), and anti-diagonal (A), as well as two circular; right (R) and left (L). The path of the polarizations' net electric field in the transverse plane as it travels is shown in Figure 1.2 for a beam proportionating out of the page.

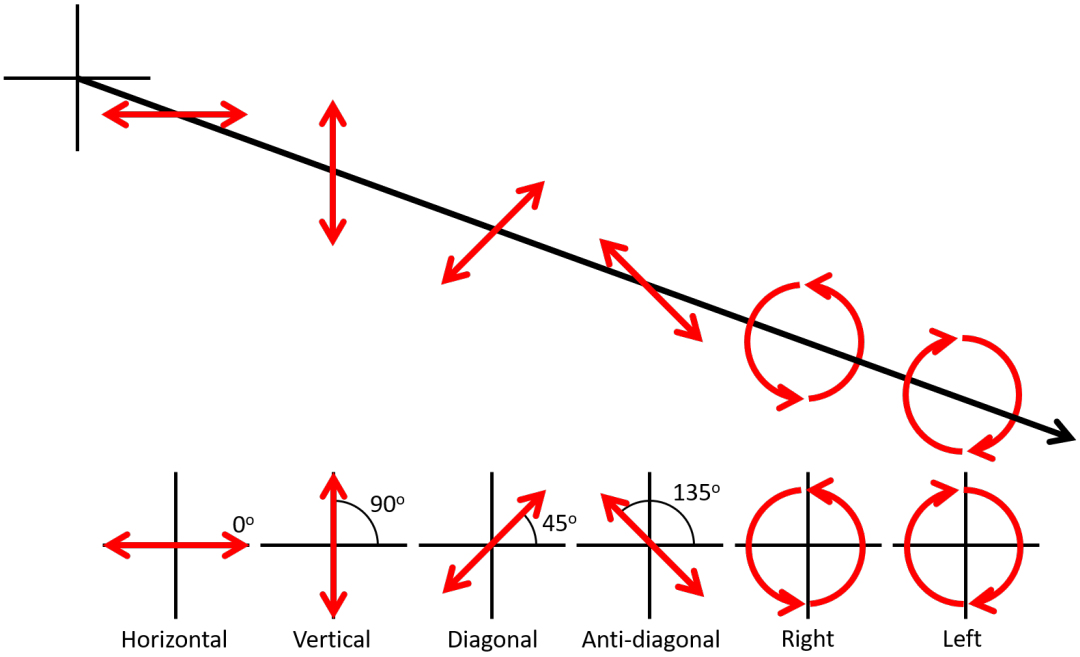

Figure 1.2: *Polarization electric field vector path in the transverse plane and relative orientations of the 6 base polarizations*

The linear polarizations can also be described with S and P designations. In this formalism, the polarization is defined based on a beam of light's reflection or refraction due to a surface. The polarization parallel to the 2D plane defined by the incoming and outgoing beam vectors is referred to as P (parallel) polarized light. The component perpendicular to this plane is denoted as S polarization, (based on the German word for perpendicular, senkrecht) [45]. These polarizations are depicted in Figure 1.3 which the S polarization denoted as coming in and out of the page. Diagonal and anti-diagonal polarizations are respectively defined in this designations as constructive (S+P) or destructive (S-P) combinations of the S and P polarizations.

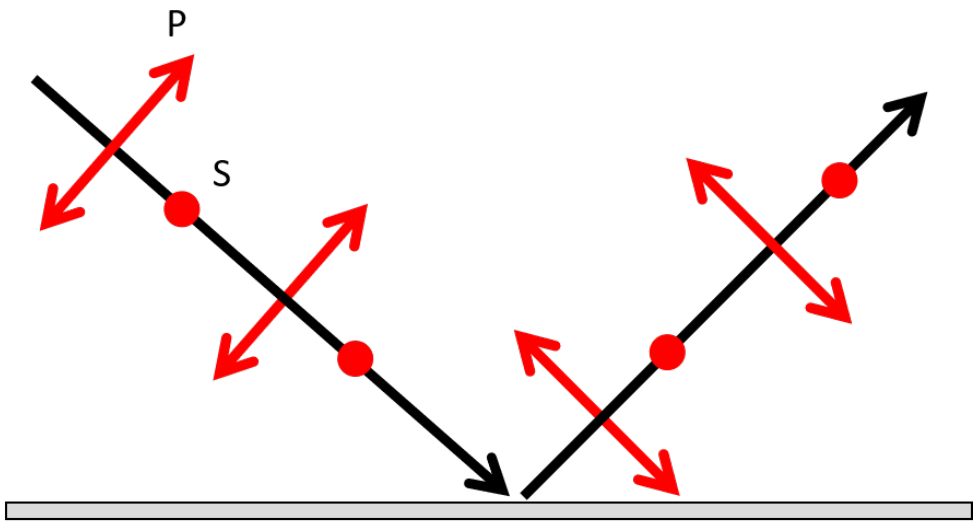

Figure 1.3: *S and P polarizations relative to surface*

1.2.1 Diattenuation

Diattenuation is the effect of a polarization dependent intensity transmittance for a ray of light [46]. This effect can be seen in various materials such as polarizers. Diattenuation can be beneficial in setting a polarization state. However, if a photon channel unintentionally experiences diattenuation, the transmitted states can be distorted, potentially resulting in an increased channel QBER.

1.2.2 Optical Retardance and Birefringence

Optical retardance is the effect of a polarization dependent phase change or optical path length on light as it travels through a medium [46]. Light can experience retardance in various ways such as traversing through a material or reflecting off a surface. Unintended optical retardance in the photon channel can distort the transmitted states and increase the channel's QBER.

One method of inducing optical retardance is through birefringence, which is a material propriety where its refractive index is polarization dependent [47]. By experiencing different refractive indices, one of the two electric field vectors will travel slower than the other inducing a phase difference between them. This in turn changes the resulting polarization. Quarter-wave and half-wave plates use this optical retardance to transform light from one polarization state to another by controlling the phase delay [47].

For a birefringent material, such as a waveplate, there exists a polarization orientation at which the incoming light will experience the lowest refractive index in the material and therefore travel the fastest. There also exists another polarization orientation orthogonal to the first, at which light of that polarization experiences the highest refractive index, and therefore travels the slowest. These two orientations are referred to as the fast axis and slow axis respectively. By tuning the thickness of the birefringent material, the phase delay generated between the fast and slow axes can be tuned to induce a quarter or half wave delay. In this manner, quarter and half wave plates are constructed.

1.2.3 Fresnel Equations

The Fresnel equations describe the polarization dependent reflection and transmission of light as it interacts with the surface of two mediums. A photon traveling from one medium with refractive index $\boldsymbol{n_1}$ reaching a second medium of refractive index $\boldsymbol{n_2}$ has a probability reflecting off the surface or refracting into the second medium. The probabilities of reflecting and refracting are dependent on the photon's polarization relative to the surface, and the refractive index of the two mediums as defined by the Fresnel equations.

Equations 1.12, 1.13 and 1.14 define the complex amplitude reflection ($\boldsymbol{r_s}$, $\boldsymbol{r_p}$) and transmission ($\boldsymbol{t_s}$, $\boldsymbol{t_p}$) coefficients for S and P polarized light respectively [47].

$$r_s = \frac{n_1 \cos\theta_i - n_2 \cos\theta_t}{n_1 \cos\theta_i + n_2 \cos\theta_t} \qquad r_p = \frac{n_2 \cos\theta_i - n_1 \cos\theta_t}{n_2 \cos\theta_i + n_1 \cos\theta_t} \tag{1.12}$$

$$t_s = \frac{2n_1 \cos\theta_i}{n_1 \cos\theta_i + n_2 \cos\theta_t} \qquad t_p = \frac{2n_1 \cos\theta_i}{n_2 \cos\theta_i + n_1 \cos\theta_t} \tag{1.13}$$

$$t_s = r_s + 1 \qquad n_2 t_p = n_1(r_p + 1) \tag{1.14}$$

These coefficients are dependent on the light's incoming angle $\boldsymbol{\theta_i}$ and transmitted angle $\boldsymbol{\theta_t}$ relative to the surface normal. The incoming angle is taken from the photon's trajectory relative to the medium boundary, and Snell's law is used to determine $\boldsymbol{\theta_t}$ as given in Equation 1.15.

$$n_1 \sin\theta_i = n_2 \sin\theta_t \quad \rightarrow \quad \theta_t = \arcsin\left(\frac{n_1}{n_2}\sin\theta_i\right). \tag{1.15}$$

From the complex amplitude coefficients, the probability of reflection and transmission for an incoming photon can be obtained based on Equations 1.16 and 1.17 [47]. This requires breaking down the photon's polarization into it's S and P components.

$$Prob_{rs} = |r_s|^2 \qquad Prob_{rp} = |r_p|^2 \tag{1.16}$$

$$Prob_{ts} = \frac{n_2 \cos\theta_t}{n_1 \cos\theta_i} |t_s|^2 \qquad Prob_{tp} = \frac{n_2 \cos\theta_t}{n_1 \cos\theta_i} |t_p|^2 \tag{1.17}$$

The additional fraction ahead of the transmission term in Equation 1.17 accounts for the impedance difference between the two mediums.

1.2.4 Jones Calculus

Jones calculus is a method for describing polarized light with vectors and linear optic elements with two-by-two matrices [48]. The effects of an optical element on polarized light is determined by taking the product of the optic's Jones matrix with the light's Jones vector producing a new Jones vector for the resulting light. Jones calculus is a simplified polarization calculus that is only valid for light that is fully polarized.

The Jones vector definition assumes the light propagation direction is along the positive Z axis [48]. Therefore, the electric field only oscillates in the X-Y plane. With this definition, horizontal polarization is defined along the X axis and vertical polarization along the Y axis. The two elements of the Jones vector $\binom{E_x}{E_y}$ represent the x and y components of the electric field vector's amplitude and phase for the light wave [48]. The Jones vector representation of the six standard polarization states are given in Table 1.2.

Table 1.2: Polarization state representations

Polarization	Jones Vector	Ket	Alternate Ket	Density Matrix
Horizontal	$\begin{pmatrix} 1 \\ 0 \end{pmatrix}$	$\|H\rangle$	$\frac{1}{\sqrt{2}}(\|D\rangle + \|A\rangle)$	$\begin{bmatrix} 1 & 0 \\ 0 & 0 \end{bmatrix}$
Vertical	$\begin{pmatrix} 0 \\ 1 \end{pmatrix}$	$\|V\rangle$	$\frac{1}{\sqrt{2}}(\|D\rangle - \|A\rangle)$	$\begin{bmatrix} 0 & 0 \\ 0 & 1 \end{bmatrix}$
Diagonal	$\frac{1}{\sqrt{2}}\begin{pmatrix} 1 \\ 1 \end{pmatrix}$	$\|D\rangle$	$\frac{1}{\sqrt{2}}(\|H\rangle + \|V\rangle)$	$\frac{1}{2}\begin{bmatrix} 1 & 1 \\ 1 & 1 \end{bmatrix}$
Anti-diagonal	$\frac{1}{\sqrt{2}}\begin{pmatrix} 1 \\ -1 \end{pmatrix}$	$\|A\rangle$	$\frac{1}{\sqrt{2}}(\|H\rangle - \|V\rangle)$	$\frac{1}{2}\begin{bmatrix} 1 & -1 \\ -1 & 1 \end{bmatrix}$
Right Circular	$\frac{1}{\sqrt{2}}\begin{pmatrix} 1 \\ -i \end{pmatrix}$	$\|R\rangle$	$\frac{1}{\sqrt{2}}(\|H\rangle - i\|V\rangle)$	$\frac{1}{2}\begin{bmatrix} 1 & i \\ -i & 1 \end{bmatrix}$
Left Circular	$\frac{1}{\sqrt{2}}\begin{pmatrix} 1 \\ i \end{pmatrix}$	$\|L\rangle$	$\frac{1}{\sqrt{2}}(\|H\rangle + i\|V\rangle)$	$\frac{1}{2}\begin{bmatrix} 1 & -i \\ i & 1 \end{bmatrix}$

A selection of common polarization elements and their Jones matrices are given in Tables 1.3 and 1.4. These matrices are defined based how the optics would act the incoming light's polarization in an ideal manner. For reference, an optic that does not effects the lights polarization, has a Jones matrix of the identity.

Table 1.3: Polarizer Jones matrices

Optical Element	Jones Matrix	Optical Element	Jones Matrix
Horizontal Polarizer	$\begin{bmatrix} 1 & 0 \\ 0 & 0 \end{bmatrix}$	Vertical Polarizer	$\begin{bmatrix} 0 & 0 \\ 0 & 1 \end{bmatrix}$
Diagonal Polarizer	$\frac{1}{2}\begin{bmatrix} 1 & 1 \\ 1 & 1 \end{bmatrix}$	Anti-diagonal Polarizer	$\frac{1}{2}\begin{bmatrix} 1 & -1 \\ -1 & 1 \end{bmatrix}$
Right Circular Polarizer	$\frac{1}{2}\begin{bmatrix} 1 & i \\ -i & 1 \end{bmatrix}$	Left Circular Polarizer	$\frac{1}{2}\begin{bmatrix} 1 & -i \\ i & 1 \end{bmatrix}$

Table 1.4: Jones matrices for quarter-wave and half-wave plates

Optical Element	Arbitrary θ	$\theta = 0$
Quarter-wave plate	$e^{\frac{-i\pi}{4}}\begin{bmatrix} \cos^2\theta + i\sin^2\theta & (1-i)\cos\theta\sin\theta \\ (1-i)\cos\theta\sin\theta & \sin^2\theta + i\cos^2\theta \end{bmatrix}$	$e^{\frac{-i\pi}{4}}\begin{bmatrix} 1 & 0 \\ 0 & i \end{bmatrix}$
Half-wave plate	$e^{\frac{-i\pi}{2}}\begin{bmatrix} \cos^2\theta - \sin^2\theta & 2\cos\theta\sin\theta \\ 2\cos\theta\sin\theta & \sin^2\theta - \cos^2\theta \end{bmatrix}$	$e^{\frac{-i\pi}{2}}\begin{bmatrix} 1 & 0 \\ 0 & -1 \end{bmatrix}$

The angle of the wave plate ($\boldsymbol{\theta}$) is given about the axis of propagation, measured from the positive X axis.

Aside from the standard optics and polarizers, Jones matrices can be created to define arbitrary birefringent materials. This makes Jones calculus a simple, but powerful tool for calculating birefringence [49].

1.2.5 Three-dimensional Polarization Ray Tracing Calculus

Jones calculus is only valid for optics traveling along a singular optical axis. However, there are many systems where the optical axis can change, such as telescopes with beam folding systems, making Jones calculus insufficient in these areas. Because of this, the Jones

matrix formalism needs to be extended into three dimensions, leading to three-dimensional polarization ray tracing calculus [50]. This method can be used to calculate the transmitted and reflected light, but for conciseness, only the light reflections are addressed here.

This formalism utilizes three-by-three matrices and vectors to define optics and light polarization in three-dimensional space. The Jones vector is replaced by the electric field vector $\boldsymbol{E}$ and the light's propagation direction is denoted as $\hat{\boldsymbol{k}}_{\boldsymbol{0}}$, both defined in the global reference frame.

$$E = \begin{pmatrix} E_x \\ E_y \\ E_z \end{pmatrix} \tag{1.18}$$

When the light strikes a surface, the polarization alteration is calculated in a local reference frame using the Fresnel equations [50, 51]. The complex amplitude components are used define the three-dimensional Jones-like matrix $\boldsymbol{J_n}$ given in Equation 1.19. This matrix is translated to the global reference frame by $\boldsymbol{M_{out,n}}$ and $\boldsymbol{M_{in,n}^{-1}}$ to form a ray tracing matrix $\boldsymbol{P_n}$ as show in Equation 1.20 for each nth optical element [52].

$$M_{out} = \begin{bmatrix} \hat{s}'_x & \hat{p}'_x & \hat{k}'_x \\ \hat{s}'_y & \hat{p}'_y & \hat{k}'_y \\ \hat{s}'_z & \hat{p}'_z & \hat{k}'_z \end{bmatrix} \qquad J = \begin{bmatrix} r_s & 0 & 0 \\ 0 & r_p & 0 \\ 0 & 0 & 1 \end{bmatrix} \qquad M_{in}^{-1} = \begin{bmatrix} \hat{s}_x & \hat{s}_y & \hat{s}_z \\ \hat{p}_x & \hat{p}_y & \hat{p}_z \\ \hat{k}_x & \hat{k}_y & \hat{k}_z \end{bmatrix} \tag{1.19}$$

The vectors $\hat{\boldsymbol{s}}$ and $\hat{\boldsymbol{p}}$ are defined by the surface's S and P polarization vectors for an optic based on the incoming light's propagation direction $\hat{\boldsymbol{k}}$. Similarly, $\hat{\boldsymbol{s}}'$, $\hat{\boldsymbol{p}}'$, and $\hat{\boldsymbol{k}}'$ are defined for the surface based on the reflected outgoing light. All six of these vectors are defined in the global reference frame.

The resulting electric field vector $\boldsymbol{E}'$ after passing through a series of optics is calculated by the product sum of all the $\boldsymbol{P_n}$ ray tracing matrices and $\boldsymbol{E}$ as shown in Equation 1.20.

$$E' = \prod_{n=0}^{N} P_n \cdot E \qquad P_n = M_{out,n} \cdot J_n \cdot M_{in,n}^{-1} \tag{1.20}$$

Based on this formalism, the theoretical polarization of a ray as it passes through linear optics in three dimensional space can be calculated.

1.3 Mechanical Stress

1.3.1 Finite Element Method

The Finite Element Method (FEM) is a numerical method for calculating a series of variables at several points over a defined domain. Instead of developing equations that define the parameters throughout the entire domain, only a finite set of points are used. This method is used when it is unfeasible or impossible to define the whole domain. Such is the case when calculating the mechanical stress or birefringence throughout an object.

An object can experience a multitude of different mechanical stresses based on the various external and internal forces exerted on it. The stress an object experiences is directly proportional to the forces exerted on it. Since in reality the applied forces are often distributed non-uniformly, the internal stresses vary throughout the object. Because of this the FEM is highly suitable for modeling the stresses in such system.

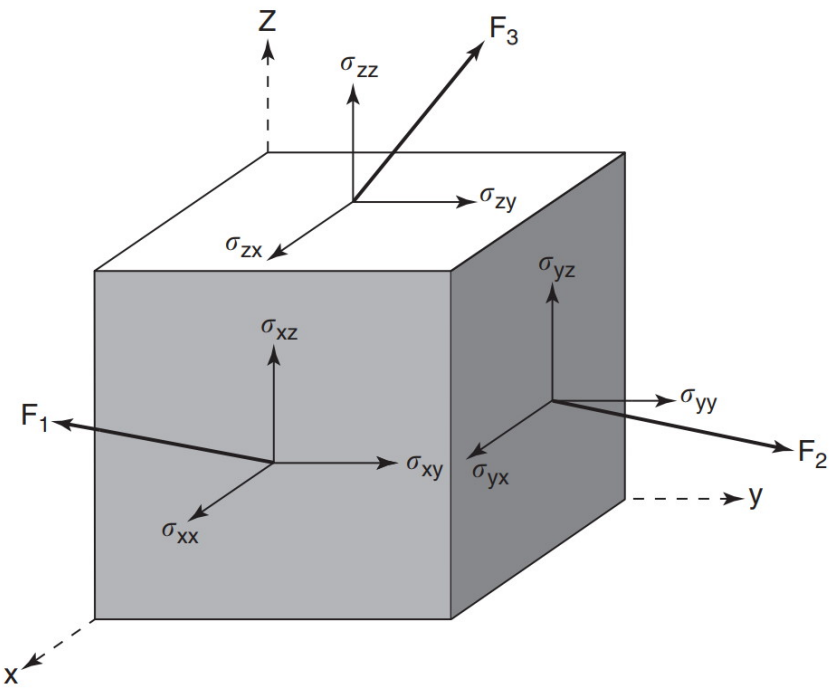

Figure 1.4: *Elemental stress cube [53]*

Each finite element of stress in the object is expressed as a block which experiences forces acting on all 6 sides. Using the assumption that the object is not accelerating, forces acting in opposite directions are equal in strength. As a result, the stress is only required to be defined for 3 faces of the element block, as shown in Figure 1.4. The stress

experienced by the faces can have any orientation in 3D space, and therefore requires 3 separate variables per face. Each element's stress ($\boldsymbol{\sigma}$) is then defined as a 3×3 matrix shown in Equation 1.21

$$\sigma = \begin{bmatrix} \sigma_{xx}, & \sigma_{yx}, & \sigma_{zx} \\ \sigma_{xy}, & \sigma_{yy}, & \sigma_{zy} \\ \sigma_{xz}, & \sigma_{yz}, & \sigma_{zz} \end{bmatrix} \tag{1.21}$$

Each stress component is given a subscript with 2 descriptors. The first represents which face the stress is acting on and the second signifies the direction the stress is acting in. 6 of the 9 stress components act parallel to the surface they are applied on, and are referred to as shear stresses. An imbalance of forces that cause the shear stresses would result in a rotation of the element. Because it is assumed that the element is not experiencing angular acceleration, these forces have to be balanced, giving rise to Equation 1.22. This simplifies Equation 1.21 to Equation 1.23.

$$\sigma_{xy} = \sigma_{yx} \qquad \sigma_{xz} = \sigma_{zx} \qquad \sigma_{yz} = \sigma_{zy} \tag{1.22}$$

$$\sigma = \begin{bmatrix} \sigma_{xx}, & \sigma_{xy}, & \sigma_{xz} \\ \sigma_{xy}, & \sigma_{yy}, & \sigma_{yz} \\ \sigma_{xz}, & \sigma_{yz}, & \sigma_{zz} \end{bmatrix} \tag{1.23}$$

1.3.2 Voigt Notation

The simplified matrix form give in Equation 1.23 can be further reduced into vector notation accounting only for the 6 unique variables [54]. This vector form, given in Equation 1.24, is referred to as Voigt notation.

$$\sigma = \begin{bmatrix} \sigma_{xx}, & \sigma_{yy}, & \sigma_{zz}, & \sigma_{yz}, & \sigma_{xz}, & \sigma_{xy} \end{bmatrix} \tag{1.24}$$

The first 3 variables given in the Voigt vector account for the tension and compression stresses, those acting normal to the surface they are applied on. The next 3 account for the shear stresses, those acting parallel to the surface they are applied on.

1.3.3 Stress Induced Birefringence

Some materials are naturally optically isotropic due to their crystal structure, meaning that their index of refraction does not vary with incoming beam direction. These materials, such as fused silica, have no or minimal inherent birefringence. However, when the materials experience mechanical stress their crystal structure becomes anisotropic, causing birefringence [55]. The amount of birefringence and directionality is dependent on the strength and orientation of the applied stress.

Chapter 2

Stress Induced Birefringence and QBER

This chapter focus on the stress induced birefringence experienced by the Window Observational Research Facility (WORF) window located on the International Space Station (ISS). The transmission of polarization states for photonic quantum signals through the WORF window are modeled to determine how the birefringence distorts the various states. The simulation model of the window I developed indicates that there are noticeable distortions of the incoming polarization states and the distortions have a high degree of angular and positional dependence. However, the stimulation results indicate that these aberrations are small and can be compensated for such that a transmitted signal experiences minimal distortions.

A short discussion on the simulation methods and results given in this chapter was presented earlier in a 2018 article [56].

2.1 Background

2.1.1 Space QUEST

It has been predicted that quantum entanglement is limited to small scales and may be affected by specific gravitational conditions due to general relativity [57, 58]. The proposed Space QUEST (Space-Quantum Entanglement Space Test) mission from the European Space Agency aims to test quantum entanglement correlations over long distances [57, 59]. As such the project, aims to experimentally test decoherence of polarization entangled photons due to gravity. Furthermore, the mission also aims to tests satellite based QKD to further the development of quantum communication on the global scale.

2.1.2 WORF Window

The Space QUEST mission proposes to share polarization entangled photon pairs between earth and the International Space Station (ISS) [59, 60]. A quantum ground station will detect one photon of the pair locally and transmit the other to a receiver in the WORF on board the ISS [59].

To reach the receiver, the incoming light has to pass through the WORF window as shown in Figure 2.1 and 2.4 [55]. The WORF window does not inherently have a significant impact on light polarization. The material used is optically isotropic, meaning it transmits light with no polarization bias or affect [55]. However, the internal atmospheric pressure of the ISS exerts mechanical stress onto the primary pressure pane, causing its crystal structure to become anisotropic. This material distortion produces birefringence, which could distort the quantum signals passing through the window.

In future context, when references are made to the window, they refer to the primary pressure pane shown in Figure 2.1.

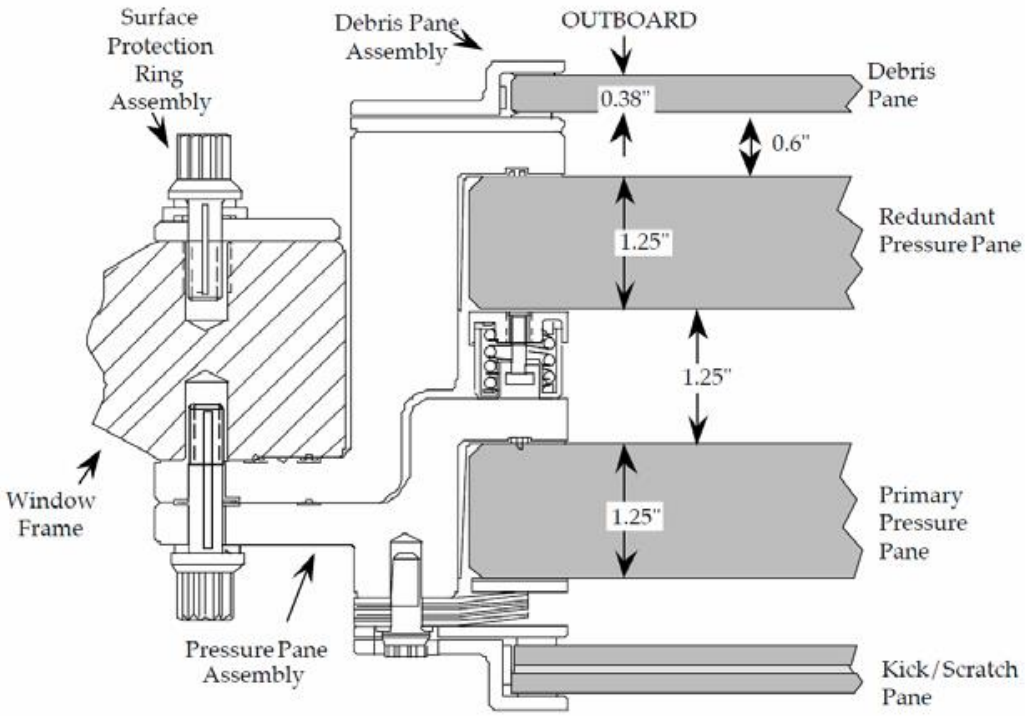

Figure 2.1: *WORF window pressure pane structure schematic [55]*

Because the window has the potential to distort the incoming optical signal, it could

be beneficial to mount the receiver to the exterior of the ISS. However, there is a variety of other factors to take into account. Keeping the experimental receiver inside the ISS would reduce the mission cost, and expedite the timeline. Furthermore, the environment inside the ISS is more thermally and environmentally stable. Because of these reasons, it is beneficial to keep the receiver inside the ISS as long as the WORF window polarization distortion is minimal.

The amount of distortion due to the window was an unknown factor for the Space QUEST mission. If the distortions are too strong, the mission could not continue with the receiver looking out through the WORF window. This birefringence study, was taken to determine the validity of keeping the telescope inside the ISS to aid in designing the receiver system.

2.1.3 Simulation Mesh

The birefringence calculation is based on a FEM stress model of the WORF window obtained from OHB [61]. This model defines the stress along a 2D slice of the window that pases through its centre as shown in green in Figure 2.2. To construct a stress mesh over the full window, the defined slice can be rotated about the window's centre axis. This is possible because the window and the stresses experienced by the window are rotationally symmetric. Rotation of each element's stress is performed in conjunction with the slice rotation to properly orient the stresses of each element in the same global reference frame.

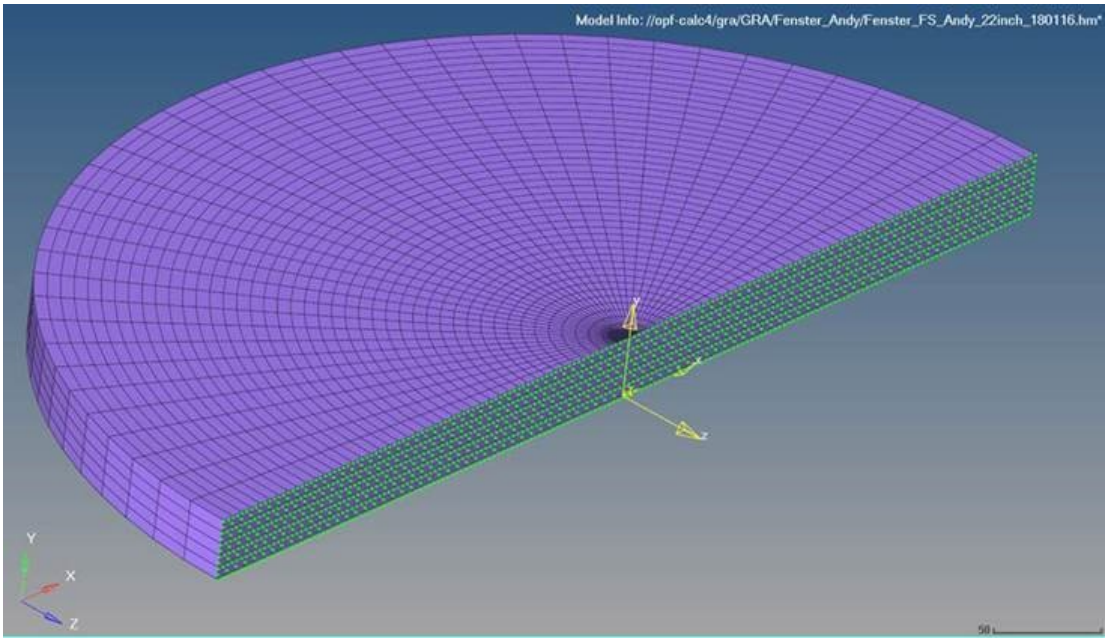

Figure 2.2: *The original mechanical stress mesh shown for half the window in purple. The 2D slice of stress the mesh is based on is shown in green [61].*

In this original mesh, each element spatially corresponds to a wedge fragment. As a result of this, the size of each FEM element varies throughout the window, and a singularity is formed at its centre. This mesh stricture would complicate the ray tracing calculations as it requires a strict understanding of how a ray exits one element and enters another.

By linear extrapolation between data points and rotation, the stress slice can be used to define the stress at any point in the window. This method was used to construct a rectangular based block mesh that approximates the cylindrical shape of the window. This results in a simpler, easier to implement, block mesh. The outer edge of the mesh is jagged due to the circle approximation. This is acceptable because the outer regions of the window are ignored as they are blocked by the mechanical assembly holding the window as shown in Figure 2.1.

The incoming beam will not always be normal to the surface of the mesh. Because of this, the incoming rays could enter an element through its top surface and exit via a side surface. This could cause further complications in the simulation. However, the birefringence is inherently proportional to the ray's path length in each element as per Equation 2.14. As a result, transitioning between elements horizontally is accounted for by the length in each element.

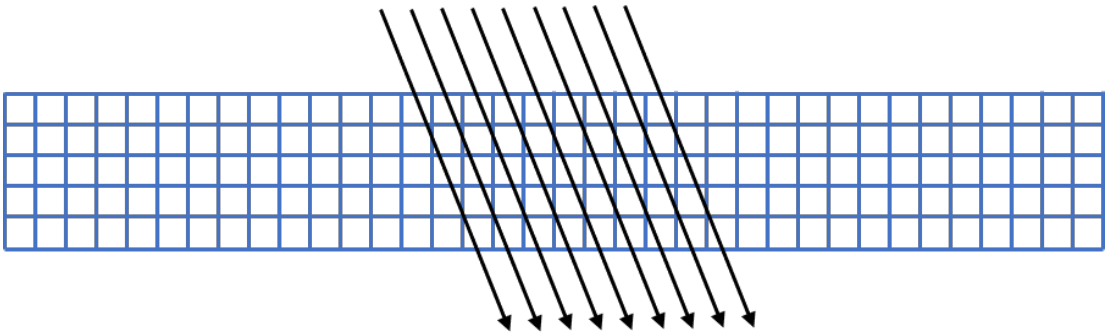

Figure 2.3: *FEM rays translating as they penetrate through the mesh*

For the simulations, a mesh size of 601 × 601 × 80 was used. Due to the shape of the window and the mesh size, each element is a rectangular-prism block and not a prefect cube. This allows for variable directional resolution which was used to optimize of the simulation's accuracy and computational time.

2.2 Model Methodology

Figure 2.1 depicts the various windows panes that make up the WORF window. For the purpose of the simulation, only the primary pressure pane is considered. This is because it is the only pane that is pressurized and therefore the only one that should experience stress. It is assumed that the stresses and birefringence in the other panes are negligible.

The model assumes a telescope with a 10cm aperture fixed 30cm from the outside of the primary pressure pane. To adjust the incoming angle, the telescope is tilted about aperture's centre such that it remains centred and a fixed distance away, causing the region of the window it sees to translate. The light was taken to have a wavelength of 810nm in a vacuum, and the window's material was given as fused silica [62, 63]. These parameters hold true for most of the simulation results. However, some results are based on modifications of the aperture diameter, or translation of the telescope receiver parallel to the window.

The incoming beam angle ($\boldsymbol{\theta}$) is defined as the angle between the incoming beam and the window's normal. Since the window is rotationally symmetric about the centre, the beam's angle about the centre does not interact with the birefringence. Because of this, the model only calculates the telescope tilt about the Y axis such that its region of observation translates along the X axis.

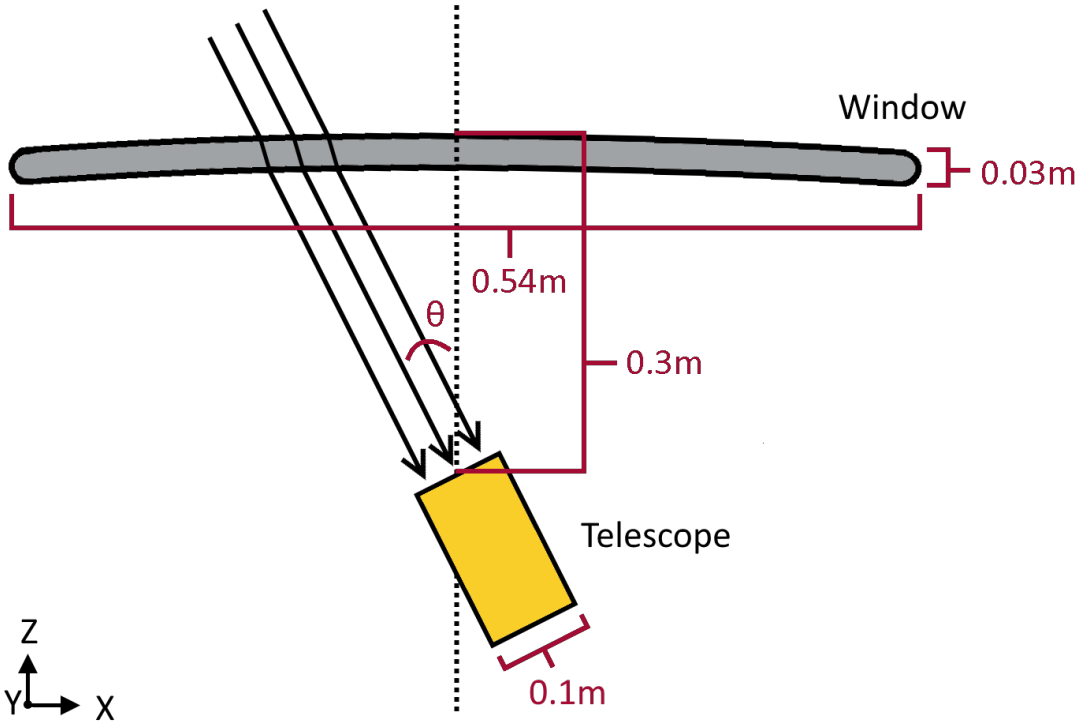

Figure 2.4: *Simulated telescope orientation relative to window*

The curvature of the window shown in Figure 2.4 is it indicate the internal pressure and stress it experiences. For the purpose of the simulations, it is approximated to have flat smooth surfaces. Including the curvature would further increase the simulation's complexity and should only have a minimal effect on the results.

It is important to note that the polarizations referenced in this simulation are defined based on the window's reference frame. It is such that the H and V polarizations are equivalent to the S and P polarizations respectively with reference to the incoming beam and the windows outer surface. Furthermore, the incoming beam is assumed to be collimated and uniformly dispersed over the full window such that the collection of the beam is only limited by the telescope's aperture.

2.2.1 Model Calculations

The birefringence model presented is based on a numerical method developed previously by K Doyle [54, 64].

The window's birefringence is calculated from an FEM model of the stress. As a result, the window is considered to consist of a 3 dimensional mesh of finite birefringent

elements. The birefringence for each element can be represented as a Jones matrix ($\boldsymbol{J_e}$). As a ray passes through the window, it will penetrate through a series of elements and therefore experience the birefringence from each element. The total birefringence ($\boldsymbol{J_T}$) a ray experiences is calculated my multiplication of each element's Jones matrix.

$$J_T = J_n \cdot J_{n-1} \cdots J_1 \cdot J_0 \tag{2.1}$$

Using Jones calculus, the QBER Equation 1.11 is translated to Equation 2.2 where $\boldsymbol{H}$, $\boldsymbol{V}$, $\boldsymbol{D}$, and $\boldsymbol{A}$ are the Jones vectors from the input states given in Table 1.2.

$$\begin{aligned} QBER = &\frac{(V' J_T H) \cdot (V' J_T H)'}{4} + \frac{(H' J_T V) \cdot (H' J_T V)'}{4} \\ &+ \frac{(A' J_T D) \cdot (A' J_T D)'}{4} + \frac{(D' J_T A) \cdot (D' J_T A)'}{4} \end{aligned} \tag{2.2}$$

The stress experienced by an element in the global reference frame is defined by the three-by-three matrix $\boldsymbol{\sigma}$. This can be redefined in the principal strain axis, creating a new stress matrix $\boldsymbol{\sigma_{PS}}$. In this new reference frame, the element only experiences a combination of compression and tension stresses, but not any shear stress. This simplifies $\boldsymbol{\sigma_{PS}}$ by reducing it to a diagonal matrix with its values being the eigenvalues of $\boldsymbol{\sigma}$. The $\boldsymbol{E}$ matrix is used to translate between the window's coordinate system and the element's principal strain reference. It is composed of the respective eigenvectors of $\boldsymbol{\sigma}$ such that Equation 2.3 is satisfied.

$$\sigma \cdot E = E \cdot \sigma_{PS} \tag{2.3}$$

In this context, $\boldsymbol{E}$ effectively acts as a rotation matrix to convert the stress between coordinate systems. This is easily demonstrated by rearranging Equation 2.3 into Equations 2.4 and 2.5.

$$E' \sigma \cdot E = \sigma_{PS} \tag{2.4}$$

$$\sigma = E \cdot \sigma_{PS} \cdot E' \tag{2.5}$$

The translation of stress to the primary strain axis is required, as the birefringence is independent of the external reference frame. The change in birefringence ($\boldsymbol{\Delta B_{PS}}$) is

calculated based on the piezo-optic tensor ($\boldsymbol{q}$) and $\boldsymbol{\sigma_{PS}}$ as determined by the photo-elastic effect [65].

$$\Delta B_{PS} = q \cdot \sigma_{PS} \tag{2.6}$$

The piezo-optic tensor is used to define how stress acting on a material affects its birefringent properties [66]. It's parameters ($\boldsymbol{q_{11}}$, $\boldsymbol{q_{12}}$, and $\boldsymbol{q_{44}}$) are defined based on the material's crystal stricture.

$$q = \begin{bmatrix} q_{11} & q_{12} & q_{12} & 0 & 0 & 0 \\ q_{12} & q_{11} & q_{12} & 0 & 0 & 0 \\ q_{12} & q_{12} & q_{11} & 0 & 0 & 0 \\ 0 & 0 & 0 & q_{44} & 0 & 0 \\ 0 & 0 & 0 & 0 & q_{44} & 0 \\ 0 & 0 & 0 & 0 & 0 & q_{44} \end{bmatrix} \tag{2.7}$$

To calculate $\boldsymbol{\Delta B_{PS}}$, $\boldsymbol{\sigma_{PS}}$ is translated into Voigt notation and Equation 2.6 is expanded to become Equation 2.8.

$$\Delta B_{PS} = \begin{bmatrix} \Delta B_{PS,xx} \\ \Delta B_{PS,yy} \\ \Delta B_{PS,zz} \\ \Delta B_{PS,yz} \\ \Delta B_{PS,xz} \\ \Delta B_{PS,xy} \end{bmatrix} = \begin{bmatrix} q_{11} & q_{12} & q_{12} & 0 & 0 & 0 \\ q_{12} & q_{11} & q_{12} & 0 & 0 & 0 \\ q_{12} & q_{12} & q_{11} & 0 & 0 & 0 \\ 0 & 0 & 0 & q_{44} & 0 & 0 \\ 0 & 0 & 0 & 0 & q_{44} & 0 \\ 0 & 0 & 0 & 0 & 0 & q_{44} \end{bmatrix} \begin{bmatrix} \sigma_{xx} \\ \sigma_{yy} \\ \sigma_{zz} \\ \sigma_{yz} \\ \sigma_{xz} \\ \sigma_{xy} \end{bmatrix} \tag{2.8}$$

The of result of Equation 2.8 is a vector with 6 components. For further calculations it is translated to the following 3 by 3 matrix using Voigt notation.

$$\Delta B_{PS} = \begin{bmatrix} \Delta B_{PS,xx} & \Delta B_{PS,xy} & \Delta B_{PS,xz} \\ \Delta B_{PS,xy} & \Delta B_{PS,yy} & \Delta B_{PS,yz} \\ \Delta B_{PS,xz} & \Delta B_{PS,yz} & \Delta B_{PS,zz} \end{bmatrix} \tag{2.9}$$

This birefringence is calculated in the principal strain axis, and therefore needs to be translated to the incoming ray's reference frame. This is done in multiple steps since the incoming ray's reference frames is not necessarily aligned with window's reference frame. An additional rotation matrix $\boldsymbol{R_\theta}$ is required for the operation. Because the window is rotationally symmetric about its centre axis, $\boldsymbol{R_\theta}$ is only dependent or the ray's angle $\boldsymbol{\theta}$

relative to the window's central axis normal to the surface. This rotation is set to be taken about the Y axis as stated in Section 2.2.

$$\Delta B = R_\theta \cdot E \cdot \Delta B_{PS} \cdot E' \cdot R'_\theta \tag{2.10}$$

At this point $\boldsymbol{\Delta B}$ is aligned such that the Z axis is parallel with the ray's direction of travel. For determining the birefringence of the ray, it is beneficial to rotate $\boldsymbol{\Delta B}$ into its own principal reference frame by the matrix $\boldsymbol{R_\gamma}$ such that the off diagonal terms are zero. This rotation is performed about the Z axis by angle $\boldsymbol{\gamma}$ in 3 dimensions ($\boldsymbol{R_{\gamma,3D}}$) and 2 dimensions ($\boldsymbol{R_{\gamma,2D}}$). It simplifies the Jones matrix determination by reducing it to a diagonal matrix in the beam's principal reference frame.

$$\gamma = \frac{1}{2}\tan^{-1}\left(\frac{2\Delta B_{xy}}{\Delta B_{xx} - \Delta B_{yy}}\right) \tag{2.11}$$

$$\Delta B_P = R_{\gamma,3D} \cdot \Delta B \cdot R'_{\gamma,3D} \tag{2.12}$$

The Jones matrix in the beam's principal frame is determined from the relative phase difference between the X axis and Y axis, which is caused by the change in refractive index induced by the birefringence.

The experienced change of refractive index ($\boldsymbol{\Delta n_x}$, $\boldsymbol{\Delta n_y}$) along each axis is determined by Equation 2.13 where $\boldsymbol{n_0}$ is the unstressed refractive index of the material.

$$\Delta n_x = -\frac{1}{2}n_0^3 \Delta B_{P,xx} \quad and \quad \Delta n_y = -\frac{1}{2}n_0^3 \Delta B_{P,yy} \tag{2.13}$$

The phase delay in either axis ($\boldsymbol{\delta_x}$, $\boldsymbol{\delta_y}$) is proportional to the $\boldsymbol{\Delta n_x}$ or $\boldsymbol{\Delta n_y}$, and the ray's path length in the element ($\boldsymbol{L}$). It is also inversely proportional to the light's wavelength in the medium ($\boldsymbol{\lambda_m}$) [67].

$$\delta_x = \frac{2\pi \Delta n_x L}{\lambda_m} \quad and \quad \delta_y = \frac{2\pi \Delta n_y L}{\lambda_m} \tag{2.14}$$

The element's Jones matrix for the polarization distortion in the beams principal reference frame ($\boldsymbol{J_P}$) is calculated from the X and Y phase shifts. Because there are only X and Y components in this reference frame, the calculation is simplified to Equation 2.15.

$$J_P = \begin{bmatrix} e^{i\delta_x} & 0 \\ 0 & e^{i\delta_y} \end{bmatrix} \tag{2.15}$$

To orientate the element's Jones matrix correctly relative to the beam's incoming orientation and the window, it is rotated back via $\boldsymbol{R_{\gamma 2D}}$. This rotation matrix is the two-dimensional equivalent of the $\boldsymbol{R_{\gamma 3D}}$ transformation about the Z axis. It inverses the $\boldsymbol{\gamma}$ rotation to obtain $\boldsymbol{J_e}$, the elements Jones matrix.

$$J_e = R'_{\gamma,2D} \cdot J_{principal} \cdot R_{\gamma,2D} \tag{2.16}$$

From the collection of $\boldsymbol{J_e}$, the $\boldsymbol{J_T}$ for a ray can be obtained via Equation 2.1. The ray's experienced QBER can then be calculated by Equation 2.2. The QBER distribution for an incoming optical beam can be calculated by mapping the collection of relevant rays appropriately. This method was used to calculate the various results found in the following Section 2.3.

2.3 Simulation Results

2.3.1 Window QBER

At an incoming beam angle of 0°, the birefringence induced onto the beam is insignificant, which agrees with previously established research [68]. The variation in QBER across the window in Figure 2.5a is mostly due to rounding and computational errors caused by artifacts in the simulation. The centre peak is a primary example of a simulation artifact. It is likely caused by the original stress grid definition and its circular symmetry resulting a singularity at the centre.

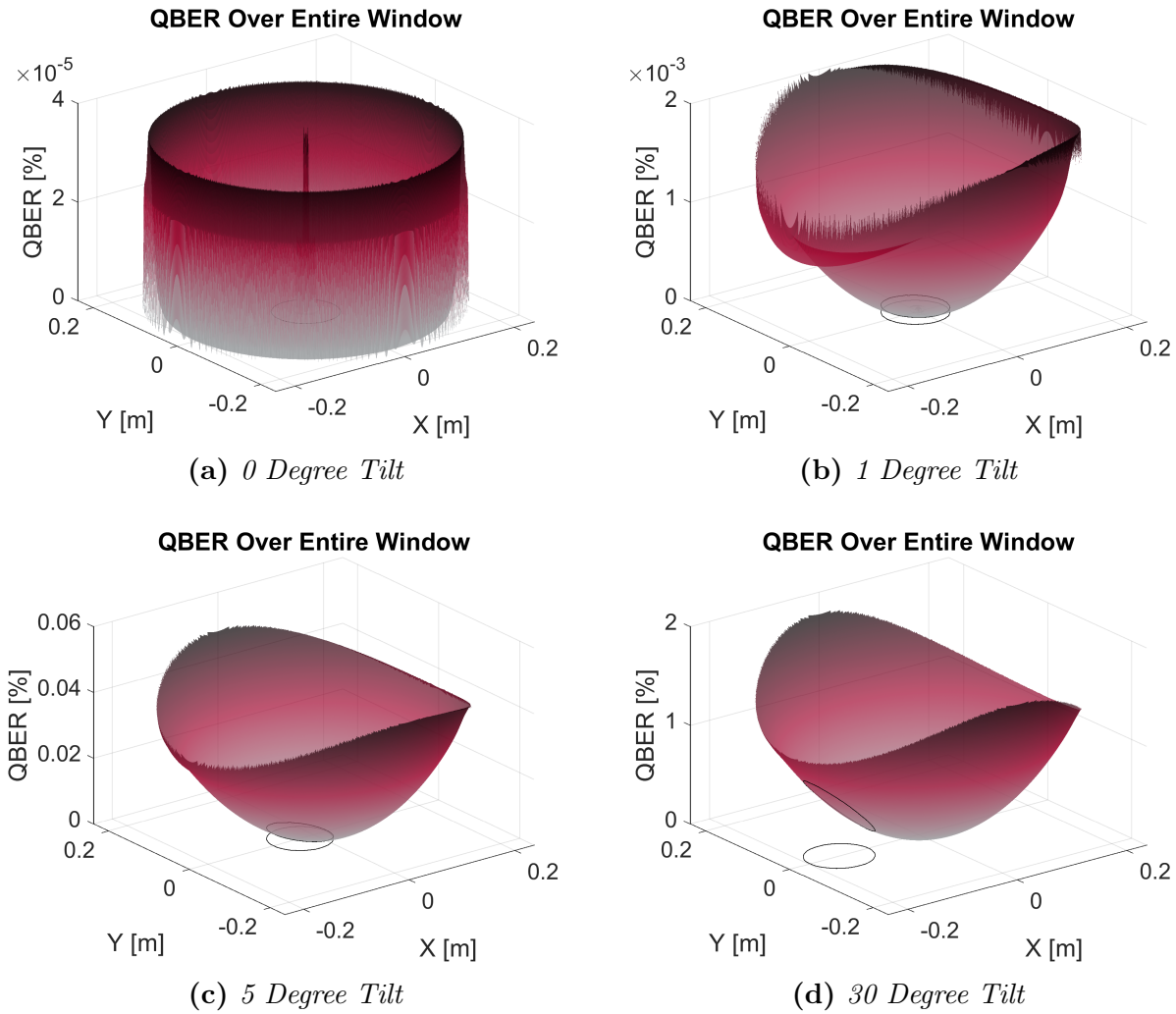

(a) *0 Degree Tilt* **(b)** *1 Degree Tilt*

(c) *5 Degree Tilt* **(d)** *30 Degree Tilt*

Figure 2.5: *The plots indicate the QBER experienced by the incoming ray as a function of where it strikes the outside of the primary pressure pane for 4 different incoming tilt angle. The black circles indicate the region of observation for the 10cm telescope and its projection onto the xy plane.*

The simulation only calculates the birefringence in a circular region at the centre of the window with a radius 85% of the window's radius. This is because there are extreme stresses stresses at the edge that can cause significantly higher birefringence then the rest of the window, cluttering the plots and making it harder to view the rest of the window. The 85% threshold cleans up most of this effect. However it is still apparent in Figure 2.5a and partly in 2.5b. Furthermore, the outer edges of the window are partially covered by the mechanical fixture holding it in place, blocking any light that would pass through it.

As the incoming beam angle is increased, the overall QBER induced onto the ray by

the window increases. This is more prevalent for rays farther from the window's centre. Even at small incoming angles, the general inverse dome patten of the QBER can be seen even though the actual QBER values are still relatively low.

The increased in tilt has two main effects. The first is the inherent increase of birefringence throughout the whole window, and the other is the translation of the telescope's observation region. The observation region translation brings window regions of higher stress into the telescope's view, leading to an increase of birefringence as seen in Figure 2.5c. At large angles, the second affect has a stronger effect on the average QBER observed by the telescope.

2.3.2 Polarization Bias

As can be seen in Figure 2.5, the QBER over the window is not radially symmetric. The main reason for this is the polarization dependence of the QBER. As demonstrated in Equation 1.11, the overall QBER experienced by a ray is taken to be the average QBER experienced by the 4 different input states S, P, S+P, and S-P. The window birefringence affects the rectilinear and diagonal bases differently, leading to a potential polarization bias where one basis or polarization experiences more or less QBER than another.

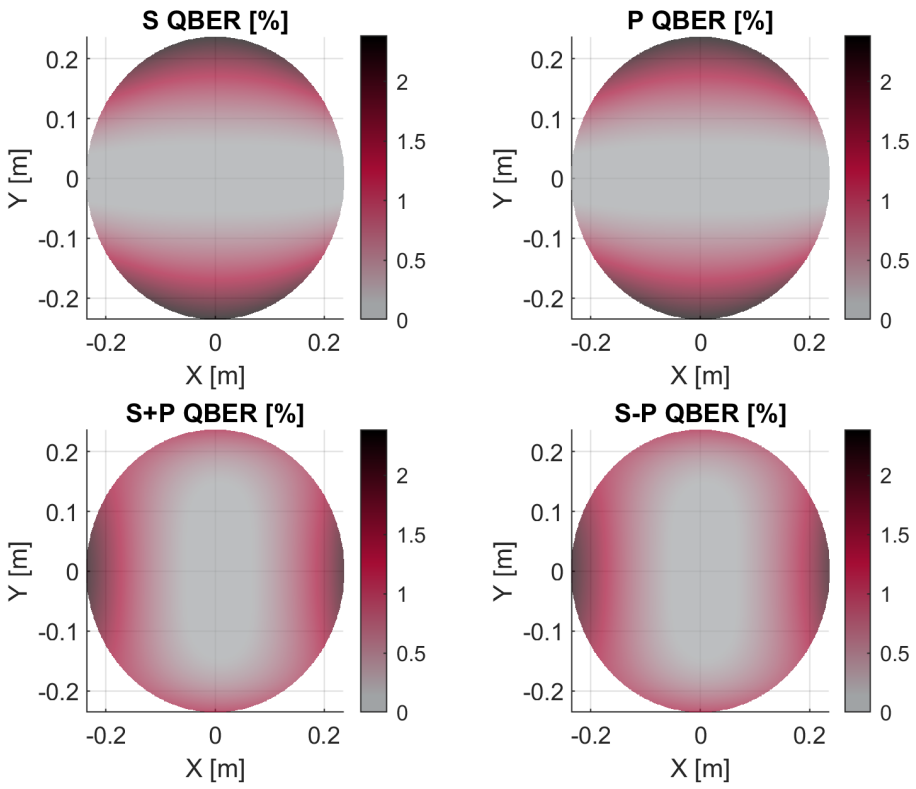

Figure 2.6: *Polarization dependent QBER for* 30° *tilt*

All of the 4 polarization states share identical window QBER distributions with their corresponding orthogonal polarizations. As the incoming beam is rotated about the Y axis, it translates along the X axis. This translation does not directly affect the rectilinear basis QBER in a significant manner as the QBER in the rectilinear basis only has slight scaling along the X axis. However, the diagonal basis shows a significant increase in QBER farther away from centre of the X axis, leading to a significant QBER bias at higher incoming tilt angles. These trends can be seen at other incoming tilt angles as well; however, only the 30° case is given in 2.6 as it best demonstrates this property.

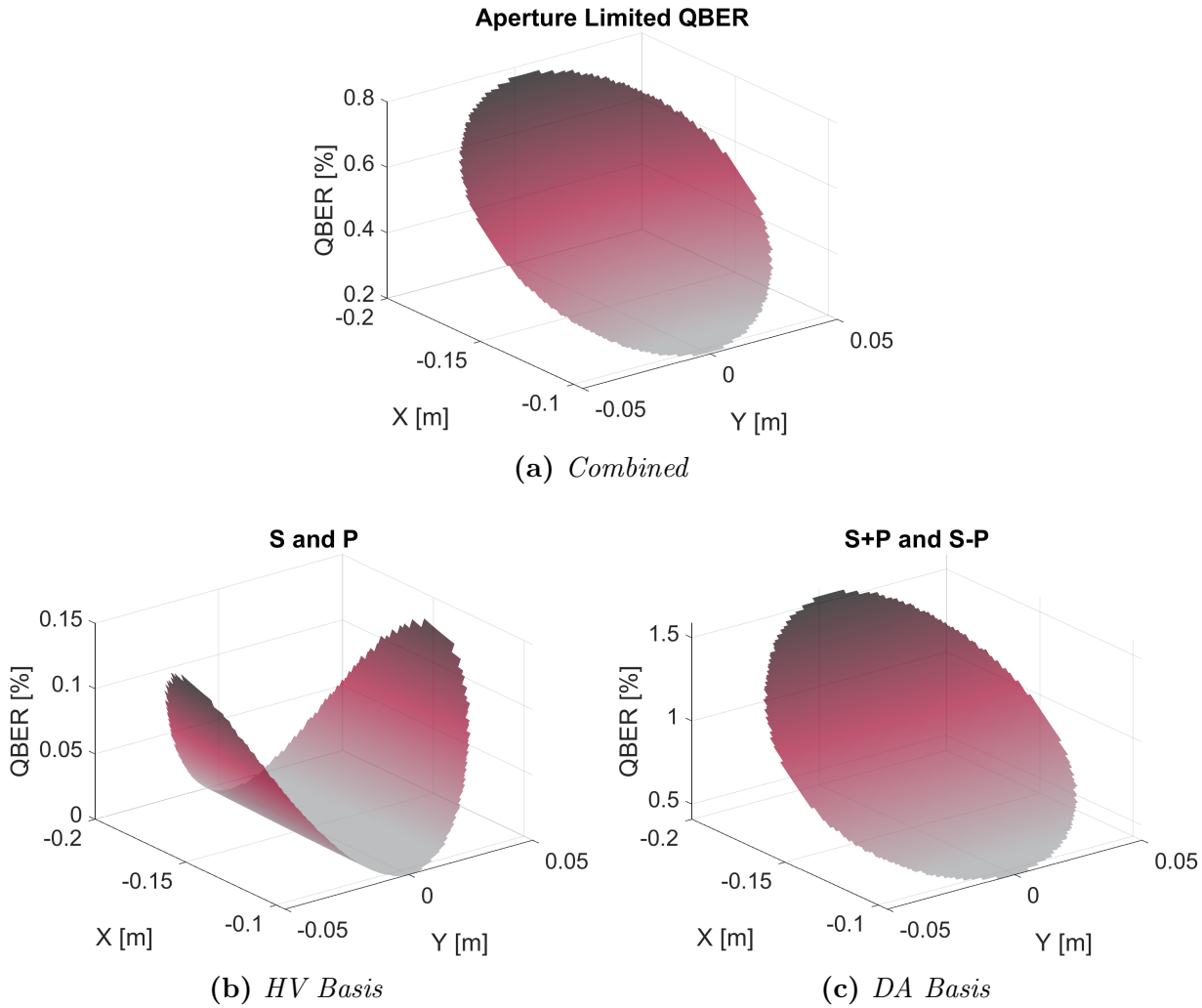

(a) *Combined*

(b) *HV Basis*

(c) *DA Basis*

Figure 2.7: *Polarization dependent QBER for* 30° *tilt limited by 10 cm aperture*

The maximum possible QBER for an aperture limited 30° tilted incoming beam is 0.15% and 1.5% in the HV basis and DA basis respectively. This order of magnitude difference further demonstrates that the overall QBER is dominated by the diagonal basis reinforcing the polarization bias.

2.3.3 Error Compensation

It has been demonstrated that the incoming angle can cause a significant increase in the window's QBER. Furthermore, it can lead to a polarization basis bias potentially affecting the Protocol's security. Several methods exist to compensate for and reduce these effects, decreasing the QBER and polarization bias induced by the window.

2.3.3.1 Self Compensation

As the incoming beam transmits through the window, each of its individual rays pass through 80 different simulated elements. This is treated as the beam effectively passing through 80 birefringent layers as it transverses the window. The incoming rays enter at layer 0 and exit at layer 80, shown in Figure 2.8 and 2.10 as traveling from the bottom up. The QBER given for each layer in the figures correspond to the accumulated birefringence experienced by the ray as it transversed the window up to that point.

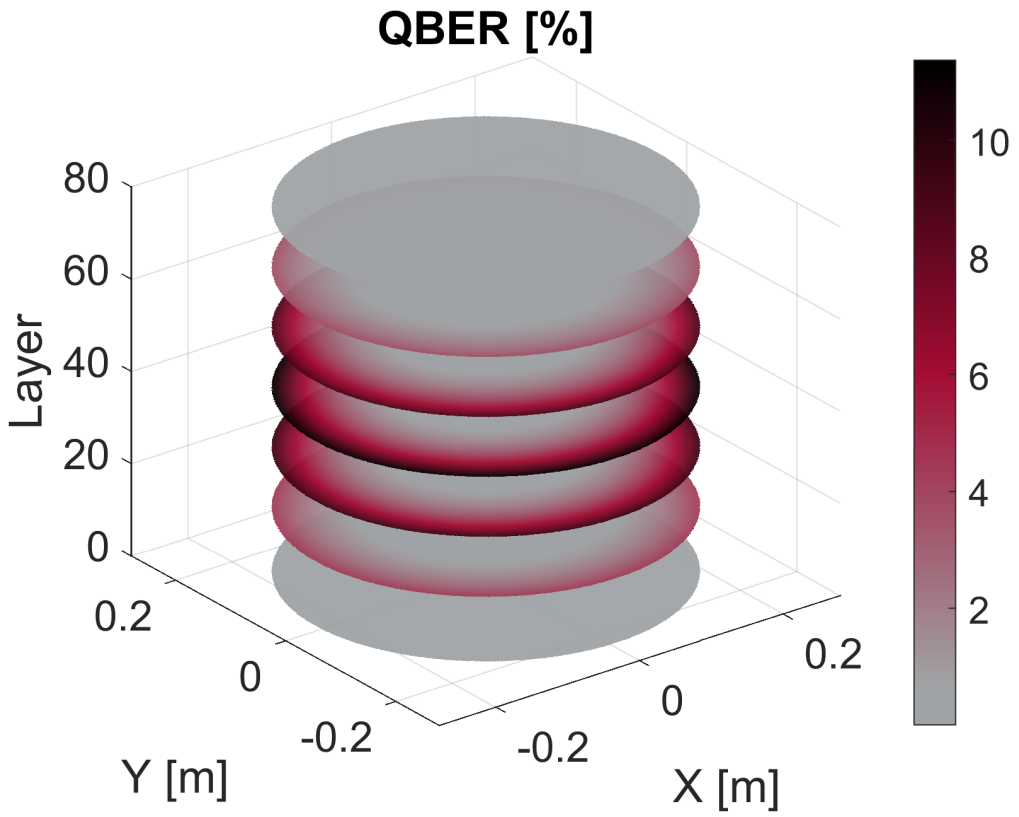

Figure 2.8: *QBER of the incoming beam as it transverses the window at a tilt of* 0°. *Only 7 layers out of the 80 are shown as to visually simplify the figure.*

The QBER for the rays in Figure 2.8 can be as large as 11% at the edges of layer 40. This demonstrates that the stress does have an effect on the beam even at normal incidence. However, after the beam has fully transversed the window, the net birefringence experienced by the beam is negligible as demonstrated by Figure 2.5a. This implies that the window has a passive self compensating effect, reducing its induced birefringence.

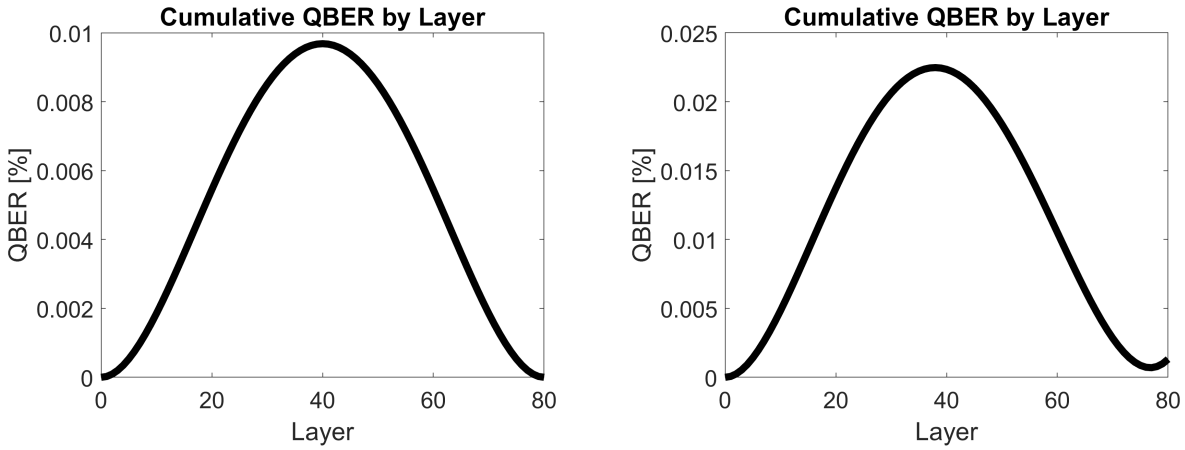

(a) 0° *Tilt*

(b) 5° *Tilt*

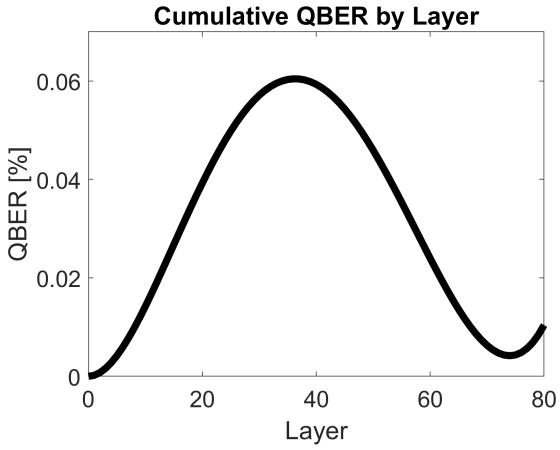

(c) 10° *Tilt*

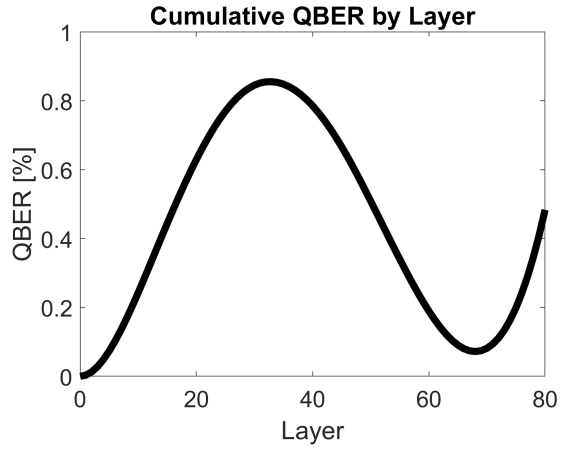

(d) 30° *Tilt*

Figure 2.9: *Average QBER of a 10cm aperture limited beam as it passes through the window at various incoming beam angles*

It is assumed that the incoming beam's optical power is evenly distributed over the window and therefore the telescope as well. Because of this, the QBER seen by the telescope is calculated based on the uniform average of all rays that enter the telescope's aperture.

At 0° tilt, the QBER is highly symmetric about the centre plane of the window, and the self compensation is very effective. As the tilt increases, the compensation effects are lessened, resulting in the window imparting a non-negligible QBER onto the beam. Even at higher angles, the compensation effect is still present. The peak QBER occurs near layer 40 for small incoming tilt angles, but shifts to earlier on at higher angles. As the ray penetrates deeper into the window the compensation is only partially effective and the QBER increases again for larger incoming angles.

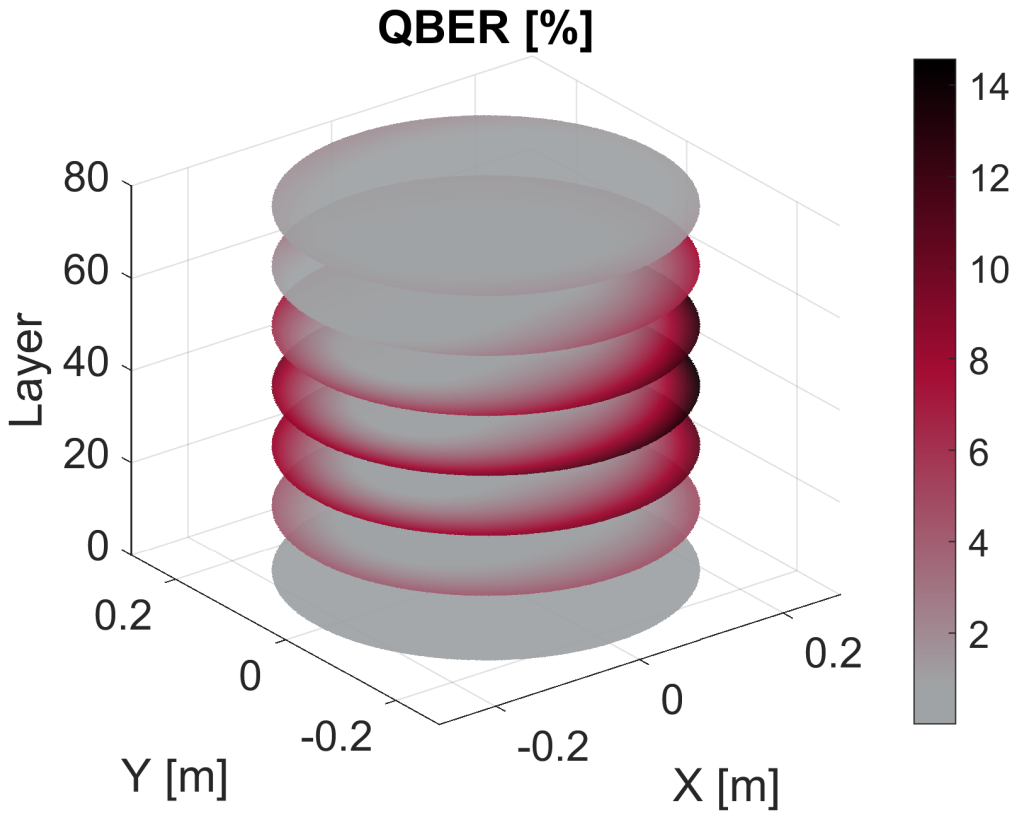

Figure 2.10: *QBER of the incoming beam as it transverses the window at a tilt of* 30°. *Only 7 layers out of the 80 are shown as to visually simplify the figure.*

The self compensation effect is theorized to be caused by the opposing stresses on the inner-side, layers 40-80, and outer-side, layers 0-40, of the window. The internal atmospheric pressure generates an outward force on the window causing it to bow outward. This in turn stretches the window's outer-side of and compresses its inner-side. As a result, the stresses at the front and back of the window have similar magnitudes, but are oriented in opposite directions. Figure 2.11 demonstrates this property for the window's radial stresses. This stress anti-symmetry generates anti-symmetric birefringence. Any polarization distortion experienced by a ray as it penetrates through the window is compensated by the opposing distortion in the later half of the window, leading to self compensation.

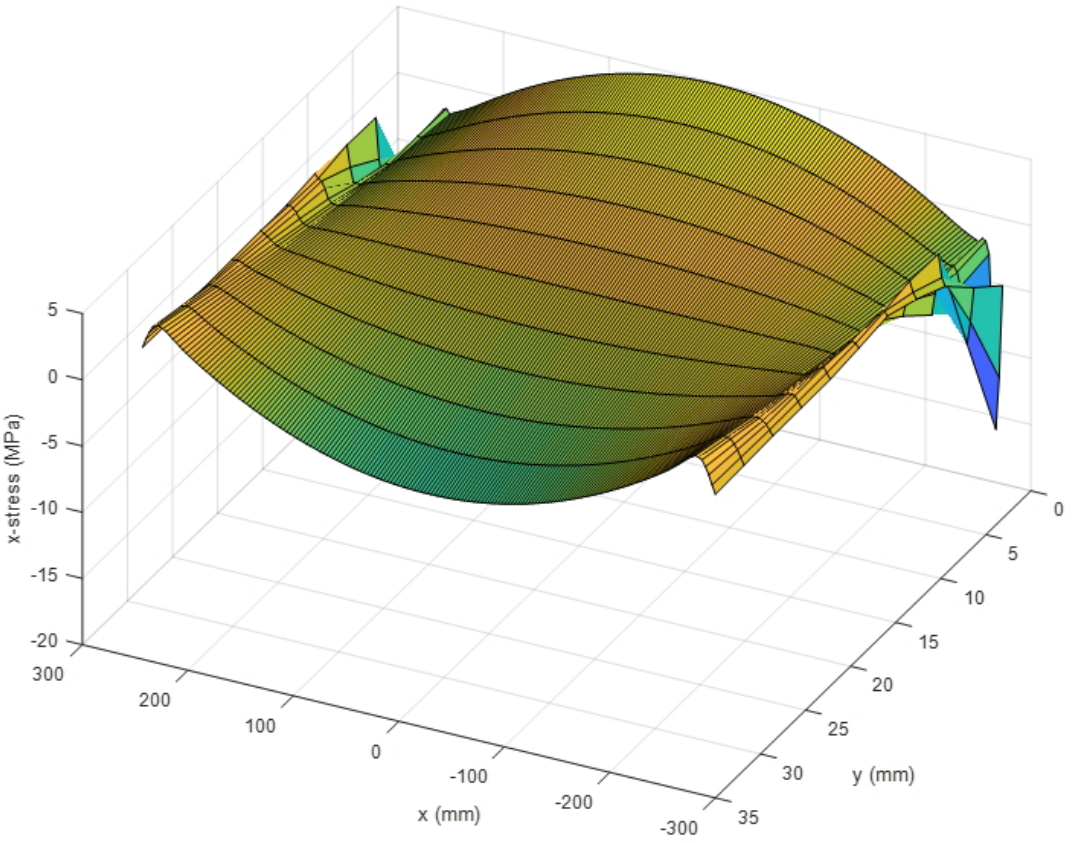

Figure 2.11: *The radial stress experienced by the window given as a slice passing through the centre of the window. This graph is used as a representative example of the stresses experienced by the window. The x-axis indicates the radial distance from centre. Low y values indicate the outer-side of the window and larger values correspond to the inner-side.*

As the incoming angle differs more from normal, the incoming rays experience an effective translation as it passes through the window. The higher the angle, the greater the ray translation. Because the X and Y position of where the ray exits the window is different than where it entered, there will be a deviation in the stress's magnitude and orientation at each location. This results in a reduction of the birefringent anti-symmetry and consequently a weaker self compensation effect at higher angles as simulated in Figure 2.9. There is still some partial compensation as the stresses tend to very gradually. Even though the birefringence of the window itself does not change, the total experienced birefringence and QBER can be affected dramatically by the incoming angle.

Figure 2.11 shows that the stresses near the centre of the window (short radial distances) tend to very gradually. As the stress location moves further from centre, the change in stress increases more rapidly. Because of this, the variation of entrance and exit location of

a ray has a more disruptive effect on the natural self compensation. This gives rise to the window QBER plots having an inherent bowl-like structure such as those given in Figure 2.5.

Stresses in the central region of the window are relatively smooth where as the edge stresses can vary rapidly. These extreme stress edge effects are due to clamping of the window holding it in place. The stresses are liable to induce abnormally high amounts of birefringence. They are the reason why only the inner 85% of the window is simulated as to not overshadow any underlying trends in the rest of the window.

2.3.3.2 Unitary Compensation

The total birefringence a ray experiences is simulated to act in the form of a Jones matrix ($\boldsymbol{J_T}$). The resulting polarization state of the ray after it passes through the window is determined by multiplying it by $\boldsymbol{J_T}$.

To mathematically reduce or remove the effects of $\boldsymbol{J_T}$, another 2×2 matrix can be applied to compensate. Ideally, this matrix $\boldsymbol{J'_T}$ would be able to fully compensate for $\boldsymbol{J_T}$. However, there are some limitations on creating a compensation matrix in reality. The way said matrix could be implemented would be via a series of known birefringent materials, such as waveplates.

Using waveplates restricts the compensation matrix to be a unitary and not an arbitrary matrix. A quarter waveplate followed by a half-wave plate and another quarter-wave plate can be used to create any arbitrary Jones unitary by rotating them about the optical axis to various angles.

Ideally each ray could be compensated for individually with its own unitary matrix. Practically, this would be a highly complex process, as it would require a dynamically adjustable birefringent optic with spatial variance. This device would need to alter the birefringence over the receiver aperture on the fly as it tracks the ground station. This could potentially be done with complex high resolution liquid crystal elements. Furthermore, it would constantly require updated information about the birefringence it is trying to actively compensate for. Implementing this form of compensation would present its own additional challenges and costs.

To implement the correction matrix more feasibly, one set of waveplates could be used over the whole beam collected by the telescope. As a result, only one matrix can be used to compensate all the rays that are collected by the telescope, and the rays cannot be corrected for individually. This form of compensation is based on a first order approximation of the birefringence.

In the simulation, the calculated $\boldsymbol{J_T}$ are very close to unitary, so theoretically they can be fully compensated for. However, since only one unitary can be applied, to optimally correct for the birefringence, the unitary must compensate for the average $\boldsymbol{J_T}$. Because the average $\boldsymbol{J_T}$ is not necessarily unitary, it is not possible for a unitary to perfectly compensate for the window's birefringence.

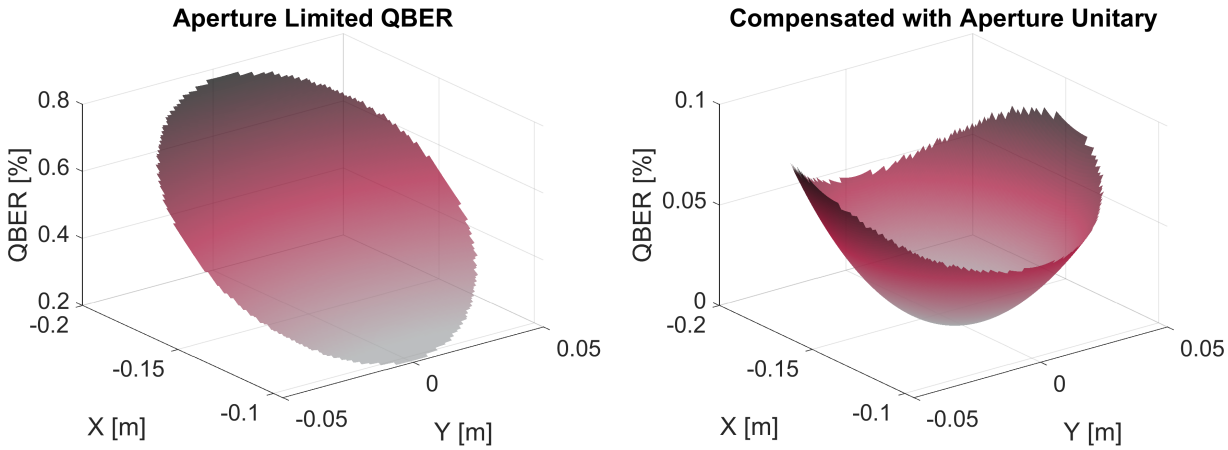

(a) *Without Unitary Compensation* **(b)** *With Unitary Compensation*

Figure 2.12: *QBER for* 30° *tilt limited by 10 cm telescope aperture*

With the compensation unitary applied, the QBER is reduced throughout the entire region of observation as shown in Figure 2.12. By compensating for the average ray, the unitary is effectively optimized to compensate for the central ray, as it is the most similar to the average. As a result, the compensated QBER plot will consistently have a minimum near its centre, causing a bowl like structure in the QBER plots.

2.3.3.3 Translation Compensation

Due to the lower variation of stress near the window's centre, it has less angular dependent stress induced birefringence than the edges do. However, due to the fixed telescope position, the telescope's region of observation shifts to the edge of the window forcing it to view regions of higher QBER when the incoming angle is increased. By mechanically translating the telescope as it rotates, the region of observation can remain in the centre of the window, eliminating the translation induced birefringence as shown in Figure 2.13.

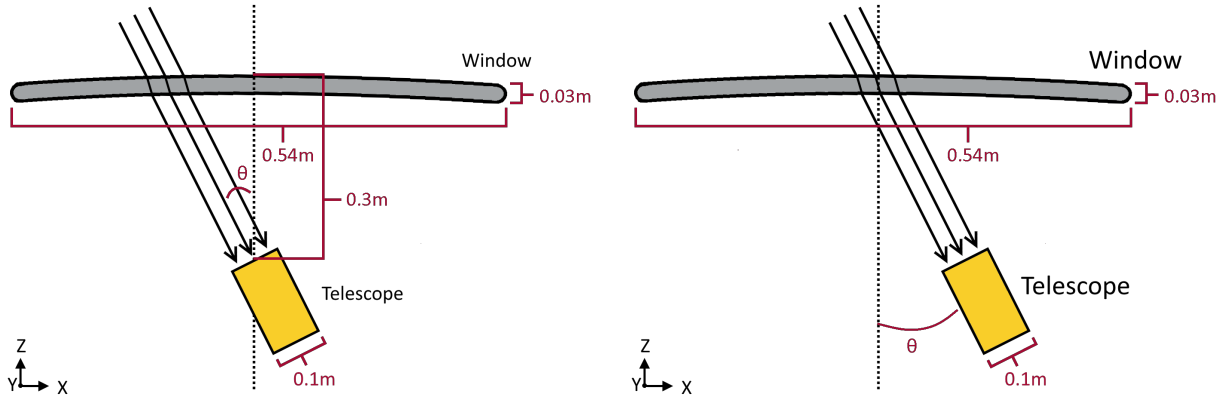

(a) *Fixed Telescope Position* **(b)** *Translated Telescope*

Figure 2.13: *Telescope translation compensation*

Translation compensation has a very similar effect on the QBER distribution as the compensation unitary does. They both transform the uncompensated QBER structure to a bowl-like stricture. The most significant reduction in QBER occurs when both active compensation mechanisms are applied as shown in Figure 2.14.

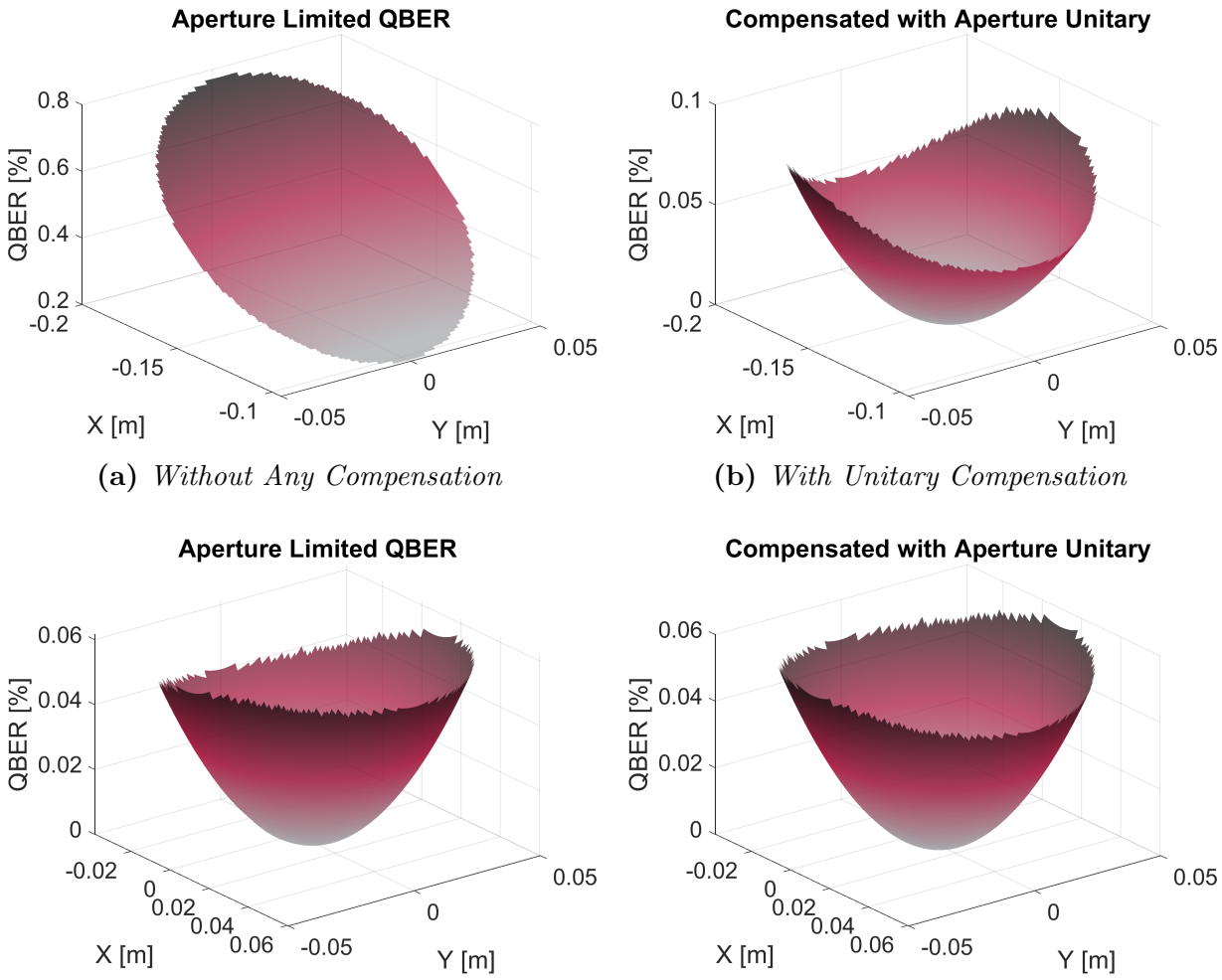

(a) *Without Any Compensation*

(b) *With Unitary Compensation*

(c) *With Translation Compensation*

(d) *With Unitary and Translation Compensation*

Figure 2.14: *Comparison of unitary and translation compensation*

2.3.4 Aperture Diameter Effects

Having a larger telescope aperture is generally beneficial as it can collect more light, increasing the received optical power. However, it can also increase the average QBER over the telescopes region of observation. Since the telescope is able to view more of the window, it is naturally forced to view regions that are closer to the edge of the window which induce higher QBER as shown in Figure 2.5d. This in turn increases the telescope's averaged observed QBER.

The increase in aperture affects the rectilinear basis more than the diagonal basis because the QBER increases in both directions along the Y axis in HV basis as depicted in

Figure 2.6 and Figure 2.7. Because the HV basis QBER distribution curves up in both the positive and negative Y axis, while remaining consistent along the X axis the QBER can only increases with aperture diameter. For a fixed angle increasing the aperture diameter exposes regions of both more and less QBER resulting in only a slight increase in overall DA QBER as shown in Figure 2.15.

Increasing the aperture diameter also reduces the effectiveness of the compensation unitary. The larger area of coverage means that there will be a greater difference between the birefringence experienced by any one ray and the average. This is important as there would practically be unitary compensation optics in a QKD implementation, and the final QBER would be determined post compensation.

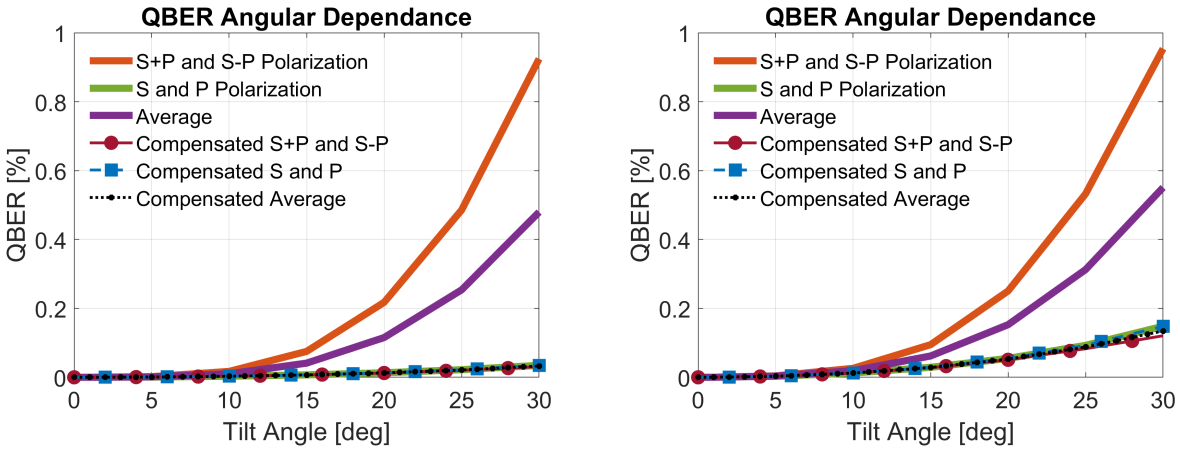

(a) *10cm Aperture* **(b)** *20cm Aperture*

Figure 2.15: *Aperture dependent QBER at various incoming angles for 10 cm (left) and 20 cm (right) apertures. Unitary correction is used for the compensated values presented*

It is interesting to note that the average QBER in the rectilinear basis is unaffected by the unitary compensation. This is indicative of the HV basis already having a minimum QBER at the centre of the aperture. Additionally, the compensated diagonal basis QBER drops below that of the rectilinear QBER. This shows that the curvature of the DA basis QBER is less than that of the HV basis as the curvature is what truly limits the corrected QBER. These proprieties are more apparent in at the larger aperture as shown in Figure 2.15

The average QBER experienced by the beam at middle of the window is significantly higher for a larger aperture. Additionally, the self compensation effect is more prevalent relatively. However, it is not enough to bring the final QBER experienced by a beam below that of one collected by a smaller aperture.

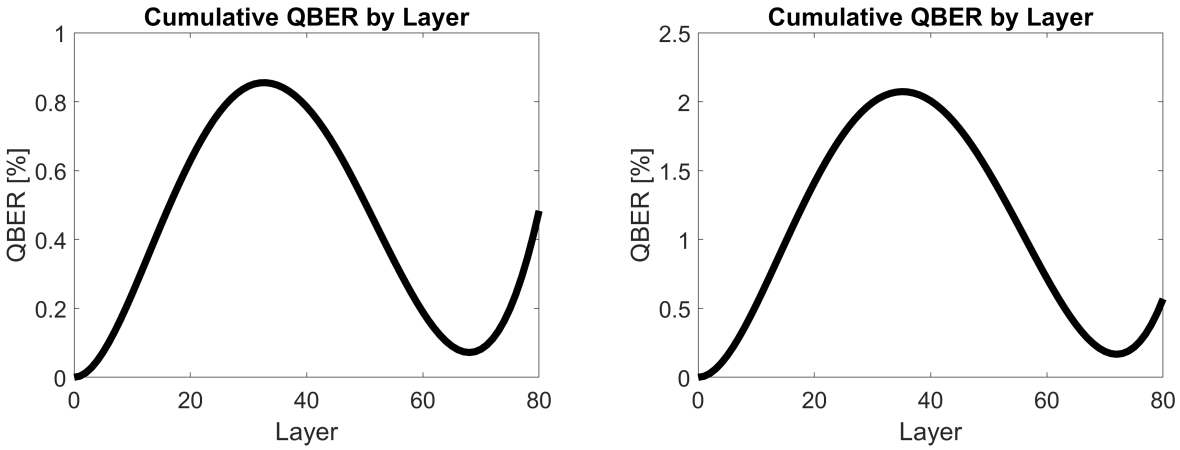

(a) *10cm Aperture* **(b)** *20cm Aperture*

Figure 2.16: *QBER throughout the window layers for a* 30° *incoming beam angle*

2.4 Conclusion

As the incoming beam is tilted away from normal, the window's induced QBER increases exponentially before and after applied compensation. This can cause a noticeable QBER increase at large incoming beam angles from normal, reaching almost 0.5% near 30° tilt for a 10cm aperture limited beam as shown in Figure 2.16a. However, the QBER can be significantly reduced with applied compensation. By compensating for the Window's birefringence with unitary and translation compensation, the QBER can be reduced by a factor of 15 to below 0.03% as presented in Figure 2.17. The compensated QBER is significantly lower that the 1% component threshold. This indicates that even at large incoming angles, the polarization distortion caused by the WORF window can be tolerated. As a result, it is viable to have the quantum receiver located inside the ISS.

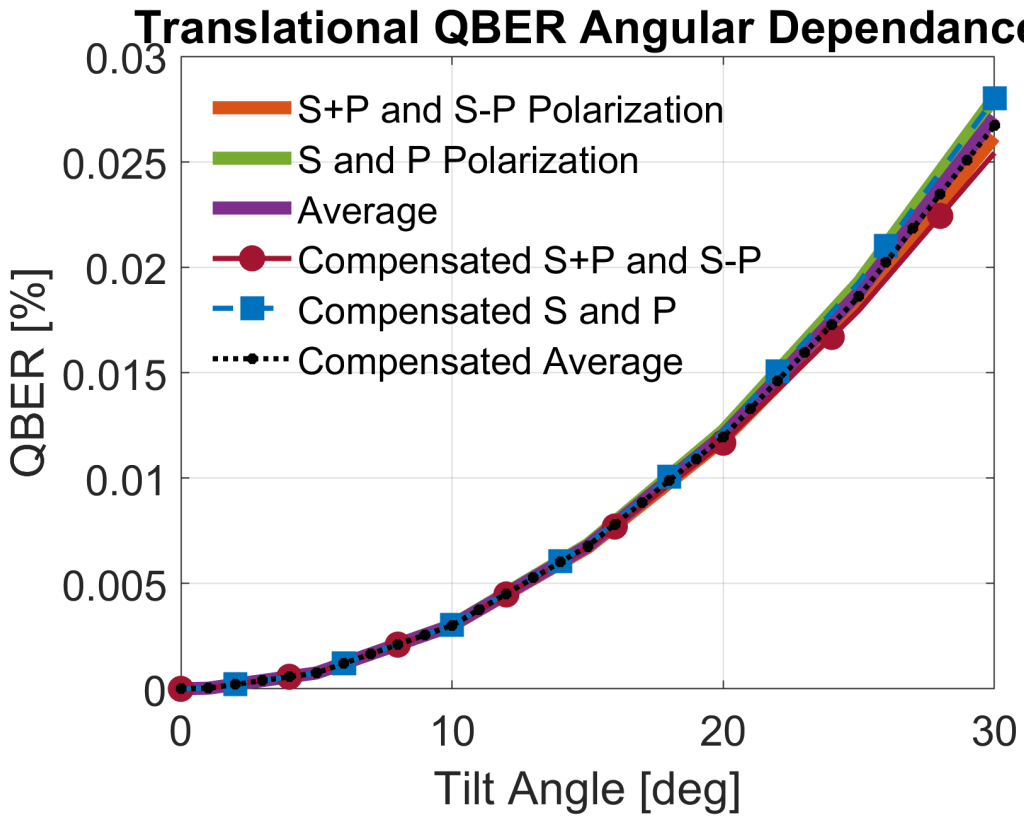

Figure 2.17: *QBER angular dependence limited by 10 cm aperture with just translation compensation (thick solid lines) as well as with unitary and translation compensation (thin dotted lines)*

The diagonal basis experiences birefringent effects significantly more than the rectilinear basis due to the orientation of stress in the window. This produces a strong polarization bias in the uncompensated QBER at large angles. However, after applied unitary and translation compensation, the bias can be significantly reduced and almost completely negated. See Figure 2.17.

Having a smaller aperture reduces the average uncompensated QBER only slightly. However, halving the aperture diameter can reduced the compensated QBER by over twofold. This means that aperture diameter is more important at large tilt angles.

Chapter 3

Optical Beam Steering

In general mirrored surfaces tend to reflect more s-polarized light than p-polarized light, which can distort the reflected polarization [69]. Additionally, perturbations of incoming beam angle may cause varying degrees of polarization distortion, reducing the effects of active compensation. As defined by the Fresnel equations, reflective surfaces act differently based on the incoming beam's polarization relative to the surface. Therefore, variations of incoming angles on a surface can effect a reflected beam's polarization state.

Long distance freespace QKD requires relatively complex receivers to collect, process and measure the possible incoming states [24]. To maintain the link over such distances, large telescopes are beneficial to collect the transmitted light [39]. Due to diffraction, the light reaching the receiver aperture will not be a purely collimated beam. As a result of this, the collected light will have slight variations of incoming angle relative to telescope's central axis. Due to the magnification required to collect the incoming beam, it will also experience angular magnification. This results in increased angular variations of the incoming light within the receiver. Furthermore, for reasons such as space conservation, the beam may not be collimated as it transverses some internal receiver telescope optics. Because of these effects, the light is liable to strike the internal optics at various non-ideal angles.

A telescope receiver size can be reduced by utilizing optics with short focal lengths to avoid beam folding; however, there are physical limitations. To have a short focal length, the lens must be relatively thick, which is more complex to manufacture and at a point, impossible for very short focal lengths. Additionally, lenses with shorter focal lengths tend to have more optical aberrations.

The combination of incoming beam angle variation and polarization reflection biases has the potential to significantly distort polarization encoded signals. Because of this I've

experimentally characterized and simulated a selection of beam steering optic configurations to study their polarization distortion. The objective of this study is to analyze the viability of each optic for implementation a quantum receiver. This research will give knowledge that is critical to the design of a quantum communication receiver as it gives insight to a system's expected error. It helps understand the magnitude of polarization based errors and shed light on potential design pitfalls.

3.1 Background

In order to process and measure the incoming beam on the receiver, it is common to use beam steering optics such as beam splitters and pentaprisms [24, 40, 43, 44]. Figure 3.1 is given as an example of internal QKD receiver optics developed previously by other members of the Jennewein research group [24, 44]. This configuration utilizes a pentaprism and beam splitter respectively to divide and reflect the beam by 90°.

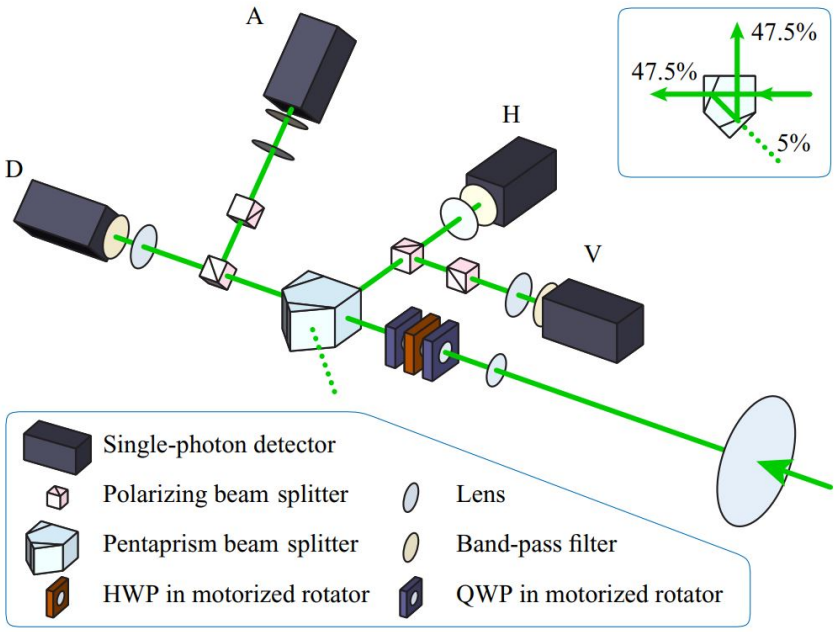

Figure 3.1: *Receiver example schematic previously developed to emulate a satellite QKD receiver for testing the feasibility of a QKD uplink. Reprinted figure with permission from Jean-Philippe Bourgoin, Nikolay Gigov, Brendon L Higgins, Zhizhong Yan, Evan Meyer-Scott, Amir K Khandani, Norbert Lütkenhaus, and Thomas Jennewein, Phys. Rev. A, Vol 92, 052339-1 and 2015. Copyright 2015 by the American Physical Society. Original available at: http://dx.doi.org/10.1103/PhysRevA.92.052339 [24]*

There are multiple beam steering optics that can be utilized to fulfill similar roles. The objective of this experimental chapter is to characterize potential beam steering optics that could be utilized to reflect an incoming beam 90°. This characterization data is then to be utilized when designing future QKD receiver systems.

The QKD receiver schemes referenced above utilize beam steering optics that both reflect and transmit a portion of the incoming beam. There are also other reflective optics used in a receiver system to route the incoming light appropriately and conserve space. This experimental study focuses on reflective optical path for simplicity.

3.2 Characterized Optics

Four different optical setups were selected as potential beam steering candidates. Diagrams of the various setups are given in Figure 3.2. The four different configurations are the single mirror (3.2a), double mirror (3.2b), pentaprism (3.2c & 3.2d), and periscope assembly (3.2e). Two different optical diagrams are given for the pentaprism as different pentaprisms were used in the manual and automated characterization experiments.

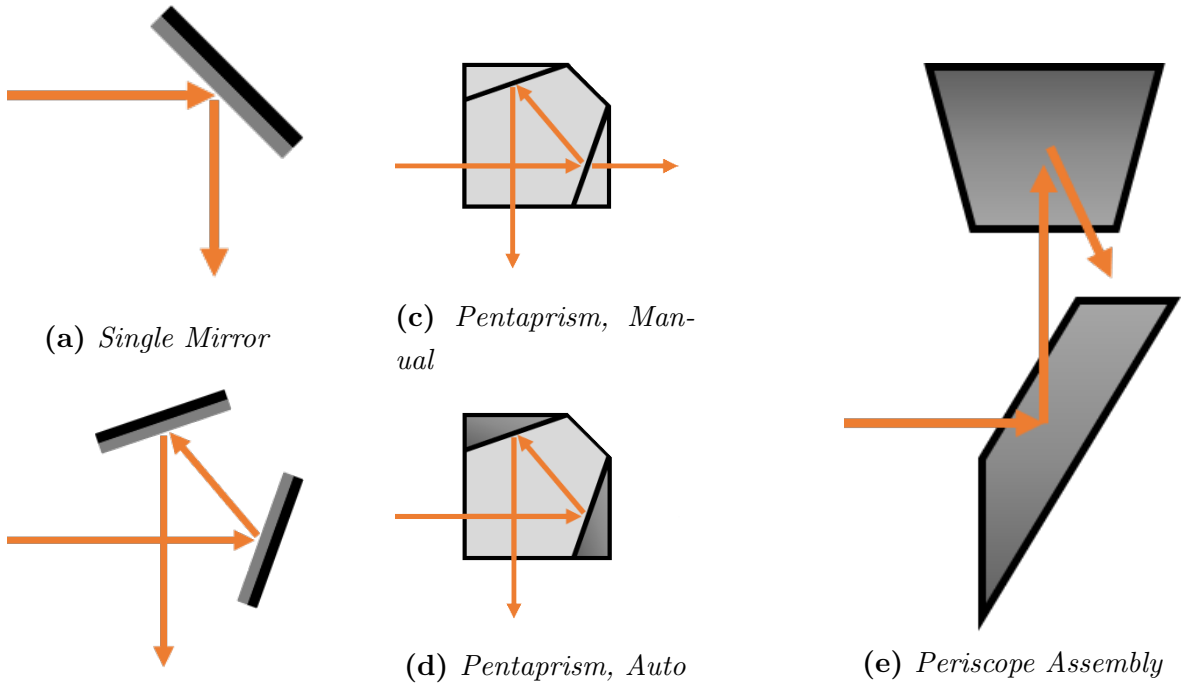

(a) *Single Mirror*

(b) *Double Mirror*

(c) *Pentaprism, Manual*

(d) *Pentaprism, Auto*

(e) *Periscope Assembly*

Figure 3.2: *Characterized beam steering configurations*

Each optic steers the beam by a set of reflections, and when reflected, the beam's

electromagnetic field can experience a phase shift based on its incoming orientation. This results in a change of the beam's outgoing polarization. Therefore, the incoming and outgoing beams may have different polarizations. Elementary descriptions on how each optic's reflections affect the beam's polarization are given in their respective sections below and in Figure 3.3. This phenomenon is described in more detail by the Fresnel Equations given in Section 1.2.3 [47].

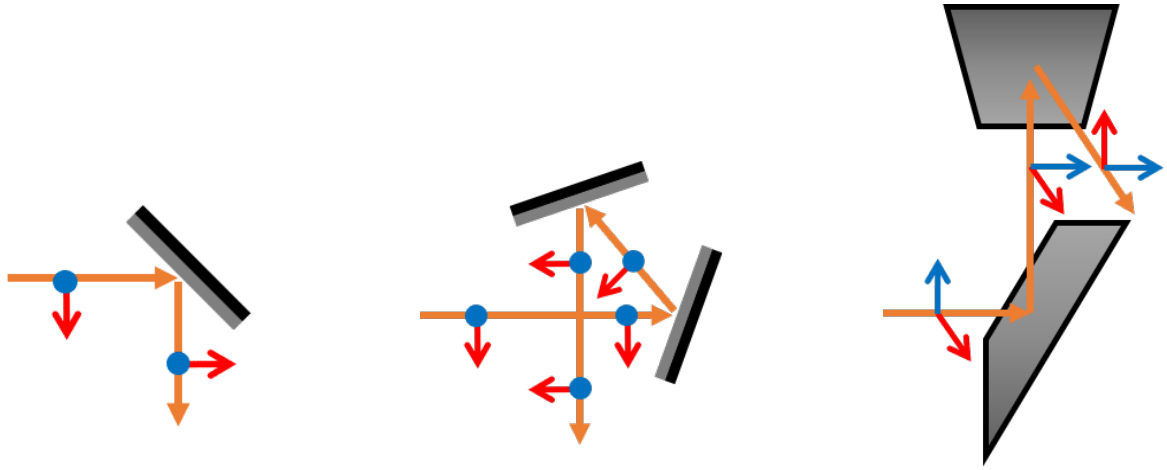

(a) *Single Mirror*

(b) *Double Mirror and Pentaprism*

(c) *Periscope Assembly*

Figure 3.3: *Polarization reflections of beam steering configurations. The blue arrow or dot represents the direction of the incoming V polarization while the red arrows indicate the direction of the incoming H polarization. Figures (a) and (b) are presented with a top-down view while (c) is presented at an angled side view due to the 3-dimensional beam steering for the periscope assembly.*

Each optic was characterized over three different horizontal (pan) angles and three different vertical (tilt) angles. Each optic has a limited field of view in each direction. Because of this, the rage of incoming angles are restricted. Each optic was characterized at the expected incident angle as well as at the edges of its field of view. The exception to this rule is the single mirror case as it would realistically have a large field of view. However, it is not expected that the single mirror would be utilized at the edges of its field of view for this particular use, so smaller angles were chosen. Each optic did not have the same maximum field of view and therefore they were not all characterized over the same incoming angles. The incoming angles tested for each optic relative to its ideal centre angle are given in Table 3.1.

Table 3.1: Incoming angular ranges used for the tested sample optics

Optic	Pan Angles	Tilt Angles
Straight Path	$(0°)$	$(0°)$
Pentaprism, Manual	$(7°, 0°, -7°)$	$(4°, 0°, -4°)$
Pentaprism, Auto	$(4°, 0°, -4°)$	$(4°, 0°, -4°)$
Periscope Assembly, Manual	$(2°, 0°, -2°)$	$(4°, 0°, -4°)$
Periscope Assembly, Auto	$(3°, 0°, -3°)$	$(3°, 0°, -3°)$
Single Mirror	$(4°, 0°, -4°)$	$(4°, 0°, -4°)$
Double Mirror	$(4°, 0°, -4°)$	$(4°, 0°, -4°)$

The optics characterized were commercial off-the-shelf components. These sample optics were tested to gain an understanding of how each beam steering system would distort an incoming signal. While in an actual quantum receiver implementation many components may be changed to specially selected components or custom coated parts, the underlying fundamentals will remain the same.

3.2.1 Single Mirror

The simplest beam steering optic is a single mirror (3.2a) orientated 45° to the incoming beam. This configuration results in a 90° beam reflection. However, if the incident angle is varied, the beam will be reflected by more or less than 90°.

When the incoming beam strikes the single mirror, the V polarization is kept in the vertical with no inversion. However, the H polarization is inverted while still remaining in the horizontal plane. This reflection has no effect on the H and V polarization measurement as V is unvaried and the 180° phase shift does not affect the H measurement. However, because the D and A polarizations are linear combination of the H and V states as defined in Table 1.2, the H inversion causes the D and A polarizations to switch positions. The polarization reflection experienced by the incoming beam is depicted in Figure 3.3a.

Due to these expected phase shifts, the uncompensated QBER for the single mirror case is calculated using Equation 3.1 below instead of Equation 1.11.

$$QBER = \frac{\langle V| M |H\rangle \langle H| M |V\rangle}{4} + \frac{\langle D| M |D\rangle \langle D| M |D\rangle}{4} + \frac{\langle H| M |V\rangle \langle V| M |H\rangle}{4} + \frac{\langle A| M |A\rangle \langle A| M |A\rangle}{4} \tag{3.1}$$

3.2.2 Double Mirror

The double mirror (3.2b) configuration is able to maintain the 90° reflection at various incoming angles by having the second mirror account for variations in the first. This is done by having the first mirror oriented with its normal 22.5° from the incoming beam, thus reflecting the beam by 45°. The second mirror is set at an angle of 45° such that under ideal conditions the reflected beam strikes the second mirror at 22.5° from the normal. This in turn reflects the beam by another 45° such that it exits the double mirror system 90° from the incoming beam.

Variations in the incoming beam angle with respect to the first mirror also change the angle of reflection off the second mirror. If the incoming beam pan angle relative to the first mirror is increased, the pan angle of reflection for the second mirror is decreased and vise versa. For example, if the first mirror reflects the beam by 50°, the second mirror will reflect the beam by 40°, and the beam will experience the desired 90° reflection.

Like in the single mirror case, the H polarization experiences a 180° phase shift and the V polarization is unvaried when the incoming beam is reflected of the first mirror. When the reflected beam strikes the second mirror, the H polarization is flipped again, resulting in a total phase shift of 360°. The incoming and exiting beam polarizations are expected to match due to the compensation effects of the second mirror. As a result of this, the double mirror system is expected to no induce polarization distortions at the ideal incoming angle. The polarization changes that the incoming beam experiences as it transverses the double mirror system is depicted in Figure 3.3b.

3.2.3 Pentaprism

The pentaprism acts in the same way as the double mirror configuration. The key difference is that there exists an additional medium between the two mirrors. In theory, this medium helps maintain the fixed angle between the two mirrors. It also compensates slightly for changes of incoming angle due to Snell's law as refraction reduces the incoming beam angle, mentioned in Section 1.2.3.

The difference between the pentaprisms used in the manual and the automated characterization is that the prior has partially reflective surfaces and therefore also acts as a beam splitter. It allows a portion of the incoming beam to transmit through the pentaprism, while the reflecting some of the beam off both surfaces.

The polarization reflections experienced by the incoming beam as it transverses the

pentaprism is identical to that cause by the double mirror system as described in Section 3.2.2

3.2.4 Periscope Assembly

The periscope assembly reflects the beam 90° horizontally, using a two mirror system. When the incoming beam strikes the first mirror, it is reflected upwards by 90°. The vertically traveling beam strikes the second mirror and is redirected horizontally by 90°. These two reflections orient the outgoing beam such that it exits the periscope assembly, making a 90° angle with the incoming beam from the top down view. Like the single mirror configuration, the periscope assembly does not maintain a 90° angle of redirection if the incoming angle is varied.

The periscope assembly naturally performs an effective rotation of the incoming linear polarizations by 90°. This causes H to become V and vice versa. In addition, D becomes A and vice versa. These rotations result in maximal polarization distortion. However, since this is a known effect, this polarization effect can be accounted for and should have no residual bias after compensation. This polarization rotation is visualized in Figure 3.3c.

The incoming beam starts traveling along the Z axis, parallel to the optics bench with the horizontal polarization also parallel to the bench (X axis) and the vertical polarization parallel to the bench's normal (Y axis). Reflection of the beam off the first mirror flips the vertical polarization to the Z axis as the ray continues along the Y axis. The second mirror flips the horizontal polarization to the Y axis while reflecting the ray to propagate along the X axis. This results in the vertical polarization being flipped into the horizontal plane and the initial horizontal polarization flipped into the vertical. Therefore, it is expected to have the polarizations in each basis flipped as a result of passing through the periscope assembly. Figure 3.3c depicts the polarization of the incident beam as it transverses the periscope assembly.

Due to these expected phase shifts, the uncompensated QBER for the periscope assembly case is calculated using Equation 3.2 below instead of Equation 1.11.

$$QBER = \frac{\langle H| M |H\rangle \langle H| M |H\rangle}{4} + \frac{\langle D| M |D\rangle \langle D| M |D\rangle}{4} + \frac{\langle V| M |V\rangle \langle V| M |V\rangle}{4} + \frac{\langle A| M |A\rangle \langle A| M |A\rangle}{4} \tag{3.2}$$

3.2.5 Ideal Ray Path

The polarization reflections for each optic described above are based on an ideal incoming ray. The light is taken to be traveling towards the optic along a perfectly horizontal path towards the optic. Any of the mirrored surfaces are to reflect the ray by exactly 90° (45° for the case of the double mirror and pentaprism cases), such that the beam is steered correctly. Deviations of incoming ray angle will change the path it takes through the optics and as a result, the resulting polarization of the ray may no longer be ideal. Because of this, the centre ray is expected to experience the least amount of distortion compared to the other rays that have deviations in their incoming angle.

3.3 Characterization Quantification

There are several different methods used for quantifying the amount of polarization distortion the optics induce. The methods of choice are: modeled channel unitaries; residual matrices and their trace; Bloch Sphere Projections; and QBER. Each of these methods are described in the subsections below.

3.3.1 Modeled Unitaries

A Jones matrix that models the system can be determined based on the polarization input and measurement results. In this case, each incoming angle is treated as an individual system as they are liable to act on incoming polarizations differently. The effect of the test optics on the incoming polarization states are approximated as unitary polarization rotations about a fixed axis on the Poincaré sphere. As such, the Jones matrices for each angle are modeled as unitaries.

The unitary calculation was performed using a program developed by Higgins et. al. [70]. This program, referred to as Poln, was designed to determine the required compensation to correct for channel distortion caused by an unknown unitary. It is based on a physical model where a quarter-wave plate followed by a half-wave plate and another quarter-wave plate are used to implement the channel compensation. The model takes in the relative measurement intensities and optimizes over wave plate angles, finding a combination that can compensate for the channel's unknown unitary. By doing so, it inherently calculates a compensation unitary, which when inverted is an estimate of the channel's unitary. Based on the measurement data, this program was used to calculate the

compensation unitaries given in the results Sections 3.4.2 and 3.5.2 to follow. For conciseness, when a reference to an optic's unitary is made, it is with regard to the compensation unitary unless specified otherwise.

Each beam steering optic has an ideal theoretical polarization effect as discussed in Section 3.2 based on how it reflects the incoming beam. This expected polarization effect can be described by a unitary transformation for each optic as given in Table 3.2. Any deviation from the ideal angle is indicative of beam polarization distortion. By comparing the ideal matrix with the unitary constructed from the polarization measurements, a further understanding of the distortion can be obtained.

Table 3.2: Ideal unitaries of the tested optics

Setup	Ideal Unitary
Straight Through Path	$\begin{pmatrix} 1 & 0 \\ 0 & 1 \end{pmatrix}$
Pentaprism	$\begin{pmatrix} 1 & 0 \\ 0 & 1 \end{pmatrix}$
Periscope Assembly	$\begin{pmatrix} 0 & 1 \\ -1 & 0 \end{pmatrix}$
Single Mirror	$\begin{pmatrix} 1 & 0 \\ 0 & -1 \end{pmatrix}$
Double Mirror	$\begin{pmatrix} 1 & 0 \\ 0 & 1 \end{pmatrix}$

The measured unitaries are expected to differ slightly from their ideal for four main reasons. The first is simply the material's birefringence and imperfections. These induced distortions in the measured polarizations are what is intended to be characterized, while the rest are a result of experimental inaccuracies. The other optics and detectors used to characterize the optic in question may have imperfections that also show up as non-idealities in the measurements. The calculation accuracy of the unitary determination implementation can also cause imperfections. Lastly, there can be a global phase difference between the average measured and ideal unitary. This can appear as a discrepancy, but

the global phase has little to no practical effect on the QKD implementation. The photon measurement process is independent of and destroys the phase information due to the Heisenberg uncertainty principle [3].

3.3.2 Residual Matrices and Traces

Another method for characterizing the polarization distortion and angular dependencies of a test optic is determining the trace of the residual matrices. These matrices describe the differences between the compensation unitaries, and therefore system unitaries, of different incoming angles. The residual matrices are determined by taking the unitary for one incoming angle and multiplying it by the conjugate of the unitary for another incoming angle. In the ideal case, the unitaries for each angle would be the exact same and the residual matrices would all come out to be the identity matrix multiplied by a global phase. As a result, the absolute value of their trace should be 2. The absolute value of the trace is taken because a global phase difference is not important as mentioned earlier, so only the magnitude of the trace is important. If the unitaries are different, the result would be less than 2, indicating that there is a discrepancy between the two unitaries and therefore an angular dependence. Equation 3.3 is given as an example of this with reference to the manually characterized pentaprism. The unitaries such as $\boldsymbol{U_{7pan,pp}}$ and $\boldsymbol{U_{-7pan,pp}}$ were calculated using the Poln program, based on the measurement data.

$$\left|Tr[U^{\dagger}_{7pan,pp}U_{-7pan,pp}]\right| = \left|Tr\left[\begin{pmatrix} 0.9957+0.0859i & 0.0136+0.0313i \\ -0.0136+0.0313i & 0.9957-0.0859i \end{pmatrix}\right]\right| = 1.9914 \quad (3.3)$$

This characterization method is commonly referred to throughout this chapter as the residual matrix trace (RMT). When the RMT is plotted, it is often displayed as two minus the RMT. In this representation format, RMTs corresponding to highly similar unitaries correspond to low values. This makes it simpler to identify which RMTs correspond to dissimilarities between the residual unitaries. Figure 3.8 is an example of where this representation is used.

The RMT characterization method can also be used to characterize the optic as a whole instead of the individual angels. In this way, the absolute value of the trace is taken of the optic's average unitary multiplied by its ideal unitary. This trace is used to quantify the difference between an optic and its theoretical ideal.

3.3.3 Bloch Sphere Projections

The polarization distortion caused by the optics can be expressed as a rotation of the state on the Bloch sphere. Because the optics are non-ideal, each polarization state may not experience the same rotation. Therefore the resulting states are not guaranteed to be orthogonal to each other. One way to visualize this is via a projection of the states onto a 2D plane of the Bloch sphere. Because the H, V, D, A states are sent and expected to be measured, the projections are given onto the H, V, D, A linear plane. Any out of plane rotation towards R or L are indistinguishable from each other as each would appear as a reduction in the vector's length, which is a deficit of this representation method.

Deviations of the H, V, D, A state projections from the 90°, 270°, 0°, 180° ideal projection angles respectively correspond to higher state distortions. State deviation from these positions is correctable by an applied unitary as discussed earlier so long as the relative angles between the state projections remains consistent. Bunching or separation of the input states reduces the compensation effectiveness of a uniform rotation correction by an applied unitary. Displaying the states on a Bloch sphere projection makes it easier to visualize this effect. Additionally, if the state projections vary strongly for different input angles, a single correction unitary will be less effective at compensating for all possible states and angles.

3.3.4 QBER

Based on the measurement data, the Poln program is also able to estimate the resulting density matrices of the H, V, D, and A states ($\boldsymbol{\Psi_H}$, $\boldsymbol{\Psi_V}$, $\boldsymbol{\Psi_D}$, $\boldsymbol{\Psi_A}$) after they are transmitted through the channel optics. From these density matrices, the QBER for each state and therefore, the channel can be calculated. For a given polarization state density matrix $\boldsymbol{\Psi_n}$, the QBER is given by Equation 3.4 where $\boldsymbol{\rho_o}$ is the polarization's ideal density matrix of the orthogonal state as given in Table 1.2.

$$\mathrm{QBER}_n = Tr\left[\rho_o \cdot \Psi_n \cdot \rho_o'\right] \tag{3.4}$$

This equation is an alternate form of Equation 1.10 given earlier based on density matrices instead of state vectors. Equation 3.5 is then used to calculate the QBER for the channel over all states assuming an equal probability of transmission for each state.

$$\mathrm{QBER}_{channel} = \frac{\mathrm{QBER}_H + \mathrm{QBER}_V + \mathrm{QBER}_D + \mathrm{QBER}_A}{4} \tag{3.5}$$

Applying the appropriate compensation unitary, as discussed earlier, to the system changes Equation 3.4 to Equation 3.6 where $\boldsymbol{U}$ is the compensation unitary.

$$\text{QBER}_{n,comp} = Tr\left[\rho_o \cdot U \cdot \Psi_n \cdot U' \cdot \rho_o'\right] \tag{3.6}$$

Physical implementation of the compensation unitary requires one matrix to compensate over all of the incoming angles as discussed in Section 2.3.3.2. This unitary is calculated with the polarization measurement data averaged over all incoming angle. By doing so, this average compensation unitary is constructed to compensate over all incoming paths to obtain a low average QBER. Because of this, each specific angle might not be optimally compensated for, and potentially made worse.

There is an alternate, simpler method for calculating the QBER for a transmitted polarization state. It is to take the measured power in the opposite state of the same basis and divide it by the total power measured in that basis. This measurement of power effectively measures the probability of a single photon measurement in the incorrect state. This QBER is therefore akin to the one defined earlier in Equation 1.9.

Because the Poln program was used for calculating the unitary, it was also used to calculate the QBER unless otherwise specified.

3.4 Manual Characterization Method

By transmitting several different orthogonal polarization states and measuring the received optical power over a set of orthogonal polarizations, a fundamental understanding of how an optic acts on polarization states can be gained. This characterization test was performed for the various test beam steering optics over several incoming beam angles. Two different experiments were conducted for this, the first being the manual characterization experiment. The second is the automated characterization experiment discussed later in Section 3.4.

Two different optics, the pentaprism and periscope assembly, were tested with the manual characterization method. Figure 3.4 depicts the experimental setup used to test the periscope assembly as an example of the manual characterization experiment. The setup used to characterize the pentaprism is functionally similar, but with a slightly different optical layout. Its layout is given in Appendix 4 for reference.

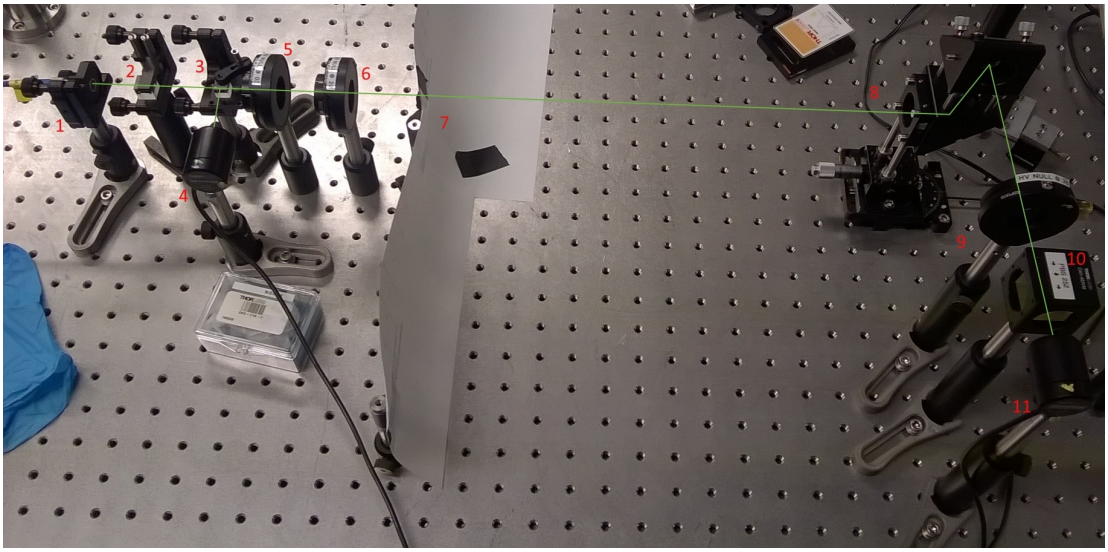

Figure 3.4: *Manual characterization setup shown with the periscope assembly under test*

3.4.1 Experimental Setup

3.4.1.1 Setting the Polarization of the Incident Beam

A 532 nm laser is coupled into a single mode fibre connected to collimator (1) as seen in Figure 3.4. The output beam passes through a polarizing beamsplitter (PBS) (2) setting the transmitted light's polarization to horizontal. Next, a 50:50 non-polarizing beamsplitter (BS) (3) reflects a portion of the beam towards the reference measurement detector (4). The optical beam power can vary as a result of the laser, optical fibre, and temperature. Because of this, the reference measurement is required to appropriately scale the measured power relative to the reference.

The measurement beam continues through a half wave plate (HWP) (5) followed by a quarter wave plate (QWP) (6). The combination of the HWP and QWP can rotate the incoming horizontal polarization into any arbitrary polarization. The particular output polarizations of interest are horizontal (H), vertical (V), diagonal (D), anti-diagonal (A), right circular (R), and left-circular (L). These 6 polarizations are chosen as they can form the 3 common orthogonal polarization bases: rectilinear basis, diagonal basis, and circular basis. The polarization measurements of the 6 different incoming polarizations can be used to determine how the system would affect any arbitrary incoming polarization. Table 3.3 indicates which set angles of the HWP and QWP are required to set the desired polarization.

The incoming light is set to H by the PBS, so the HWP and QWP are set to 0° such

that they do not affect the polarization to transmit the H state. To transmit V, the HWP is set to 45°, rotating H to V and the QWP is oriented at 0° as not to change the state. The HWP is set to 22.5° to rotate the initial H polarization to D and the QWP is rotated to 45° such that it is oriented appropriately not to affect the output D state. Similarly, to transmit A polarization, the HWP is set to −22.5° and the QWP is set to 45°. For the R polarization, the HWP is set to affect the incoming H polarization such that the QWP can rotate the H to R by setting it to 45°. To produce L, the HWP is set to 45° to rotate the incoming H polarization to V such that the QWP set at 45° rotates the V state to the L state.

Table 3.3: Waveplate orientations for preparation of the incident light polarization

		HWP (5) angle	QWP (6) angle
Polarization	H	0°	0°
	V	45°	0°
	D	22.5°	45°
	A	−22.5°	45°
	R	0°	45°
	L	45°	45°

3.4.1.2 Setting the Angle of Incidence

The optic under test (8) is affixed to a tilt stage on a rotation mount. In this configuration, the optic can pan and tilt, allowing for measurements to occur at various incoming horizontal and vertical angles. A piece of paper (7) was placed between the QWP and the optic. It was used to assist on alignment as some of the light can back scatter off the optic back towards the paper producing a spot on the paper plane. If it was accurately aligned, the back reflection should not be visible as it would align perfectly with the incoming beam. The paper also had angular markings on it to indicate the pan angle based on the back reflection spot location when used with the pentaprism.

3.4.1.3 Measurement

To measure the resulting polarization of the beam after it had passed though the optic under test, a HWP (9), PBS (10), and detector (11) were used. Attached to the detector was a 532nm ±10nm band pass filter to filter out most of the background room light. Because the PBS only transmits H, the HWP plate is used to rotate the incoming polarization about the Poincaré Sphere, translating the desired linear polarization into H

polarization. For example, setting the HWP to 45° rotates incoming V into H, allowing for the measurement of V by the detector. This allows for the measurement of H, V, D, and A polarization as they are all linear. Table 3.4 indicates the required HWP angle to measure each polarization.

Table 3.4: Half-wave plate orientation for polarization measurement of the reflected light

	HWP (9)			
Angle	0°	45°	22.5°	−22.5°
Polarization	H	V	D	A

Adjusting the incoming angle by panning and tilting the optic caused the outgoing beam to wander. As a result, the beam may drift off the measurement HWP, PBS, and detector. To prevent this, their locations are adjusted and re-aligned to optimize the beam such that the portion of the beam that would reach the detector was maximized.

For each set of measured incoming pan and tilt angles, the incoming polarization was scanned over the 6 aforementioned polarizations. The outgoing polarizations were measured in the 4 different measurement polarization states and the reference power was recorded for each. In total, 24 different polarization measurements were taken for each incoming angle to gather enough data to gain an accurate understanding of the channel distortion.

3.4.2 Results

3.4.2.1 Relative Intensities

The relative intensities and their polarization contrasts are given in the tables below. The relative intensities are the measured powers given as a scaled proportional fraction of their corresponding reference intensities.

The reference measurement used for the pentaprism pan measurements had a polarization bias. Because of this, the reference polarization bias was measured and the data was corrected based on this reference measurement. The pentaprism pan measurement data presented in this chapter are based on the corrected data. The correction process is discussed further in Appendix 4.

Table 3.5: Measured relative intensities scaled proportional to reference measurement for the pentaprism at different pan angles

			Input					
			H	V	D	A	R	L
Measured	0°	H	75.90	1.127	31.24	42.27	33.64	43.64
		V	0.955	85.08	49.54	41.13	38.72	48.56
		D	43.04	38.86	79.51	1.535	27.52	52.80
		A	30.74	52.53	1.804	82.84	43.73	40.99
	7°	H	67.03	1.244	28.60	37.99	31.55	37.46
		V	0.997	72.28	46.67	38.36	36.61	45.25
		D	39.42	34.02	72.01	1.633	23.95	49.42
		A	26.67	50.57	0.774	76.25	43.28	35.38
	−7°	H	85.98	1.532	32.82	44.43	35.33	53.59
		V	0.565	97.53	49.21	45.35	46.74	52.81
		D	47.20	43.08	83.24	0.935	37.47	55.85
		A	35.64	56.14	1.297	94.65	43.06	53.01

Table 3.6: Measured relative intensities scaled proportional to reference measurement for the pentaprism at different tilt angles

			Input					
			H	V	D	A	R	L
Measured	0°	H	8.81	0.09	3.91	4.92	5.09	4.22
		V	0.16	9.88	5.65	4.76	5.93	4.62
		D	4.81	4.45	9.45	0.05	4.47	5.32
		A	4.09	5.27	0.27	9.51	5.03	3.62
	4°	H	4.40	0.17	1.52	2.96	2.60	1.88
		V	0.17	5.05	3.51	1.83	2.49	2.57
		D	3.14	1.68	4.65	0.12	2.03	2.63
		A	1.60	3.46	0.29	4.72	3.03	1.94
	−4°	H	7.24	0.09	3.94	3.32	3.53	3.82
		V	0.06	8.35	3.66	4.93	4.07	4.33
		D	3.35	4.49	7.66	0.23	2.95	4.88
		A	4.13	3.82	0.08	7.85	4.48	3.44

Table 3.7: Measured relative intensities scaled proportional to reference measurement for the periscope assembly at different pan angles

			Input					
			H	V	D	A	R	L
Measured	0°	H	0.43	30.76	18.56	14.37	15.13	16.63
		V	29.14	0.35	13.37	17.49	16.24	14.34
		D	11.80	17.96	0.37	32.07	17.70	13.50
		A	17.86	12.64	31.0	0.35	13.27	18.18
	2°	H	0.31	27.99	17.39	12.78	15.04	14.25
		V	27.97	0.48	11.17	16.77	14.09	13.89
		D	11.30	17.13	0.51	27.00	16.48	11.95
		A	15.75	12.85	28.02	0.30	12.09	16.24
	−2°	H	0.27	27.33	15.92	12.82	13.78	14.13
		V	27.74	0.14	12.76	14.86	15.10	12.41
		D	12.06	15.46	0.38	27.62	17.08	10.67
		A	14.09	13.28	27.35	0.23	11.51	16.14

Table 3.8: Measured relative intensities scaled proportional to reference measurement for the periscope assembly at different tilt angles

			Input					
			H	V	D	A	R	L
Measured	0°	H	0.26	30.48	18.27	14.94	15.17	18.38
		V	27.00	0.40	14.40	19.32	17.00	17.03
		D	11.01	17.20	0.35	33.87	18.55	15.82
		A	16.16	12.21	33.19	0.44	13.02	20.50
	4°	H	0.94	27.83	19.26	10.77	14.17	16.09
		V	28.13	0.94	10.10	18.02	16.44	13.74
		D	9.86	19.16	0.80	28.17	18.55	11.63
		A	19.34	9.22	28.06	0.68	11.85	18.44
	−4°	H	0.15	32.63	17.08	16.34	16.13	15.75
		V	32.70	0.11	16.78	15.63	17.31	14.43
		D	15.21	17.69	0.19	32.52	18.64	13.45
		A	15.99	16.67	32.62	0.17	13.94	17.60

3.4.2.2 Modeled Unitaries

Theoretically, the unitaries representing 0° pan and 0° tilt should be exactly the same, as the incoming beam angle was set to be the same. Any difference between the two would be due to experimental errors such as alignment inaccuracies and background noise.

Table 3.9: Pentaprism compensation unitaries

Angle	Compensation Unitary
0° Pan	$\begin{pmatrix} 9.975019 \times 10^{-1} - 1.087043 \times 10^{-3}i & -7.043064 \times 10^{-2} - 5.321710 \times 10^{-3}i \\ 7.043064 \times 10^{-2} - 5.321710 \times 10^{-3}i & 9.975019 \times 10^{-1} + 1.087043 \times 10^{-3}i \end{pmatrix}$
7° Pan	$\begin{pmatrix} 9.920369 \times 10^{-1} - 1.014857 \times 10^{-1}i & -7.458871 \times 10^{-2} - 1.843878 \times 10^{-4}i \\ 7.458871 \times 10^{-2} - 1.843878 \times 10^{-4}i & 9.920369 \times 10^{-1} + 1.014857 \times 10^{-1}i \end{pmatrix}$
−7° Pan	$\begin{pmatrix} 9.975317 \times 10^{-1} - 1.813359 \times 10^{-2}i & -5.758495 \times 10^{-2} + 3.585627 \times 10^{-2}i \\ 5.758495 \times 10^{-2} + 3.585627 \times 10^{-2}i & 9.975317 \times 10^{-1} + 1.813359 \times 10^{-2}i \end{pmatrix}$
0° Tilt	$\begin{pmatrix} 9.968151 \times 10^{-1} - 6.362403 \times 10^{-2}i & -4.670039 \times 10^{-2} + 1.143045 \times 10^{-2}i \\ 4.670039 \times 10^{-2} + 1.143045 \times 10^{-2}i & 9.968151 \times 10^{-1} + 6.362403 \times 10^{-2}i \end{pmatrix}$
4° Tilt	$\begin{pmatrix} 9.808053 \times 10^{-1} - 9.450036 \times 10^{-2}i & -1.680017 \times 10^{-1} - 2.942793 \times 10^{-2}i \\ 1.680017 \times 10^{-1} - 2.942793 \times 10^{-2}i & 9.808053 \times 10^{-1} + 9.450036 \times 10^{-2}i \end{pmatrix}$
−4° Tilt	$\begin{pmatrix} 9.939201 \times 10^{-1} - 9.624476 \times 10^{-2}i & 5.329667 \times 10^{-2} - 4.390063 \times 10^{-3}i \\ -5.329667 \times 10^{-2} - 4.390063 \times 10^{-3}i & 9.939201 \times 10^{-1} + 9.624476 \times 10^{-2}i \end{pmatrix}$

Table 3.10: Periscope assembly compensation unitaries

Angle	Compensation Unitary
0° Pan	$\begin{pmatrix} -7.803656 \times 10^{-2} + 2.370657 \times 10^{-2}i & -9.941095 \times 10^{-1} - 7.137710 \times 10^{-2}i \\ 9.941095 \times 10^{-1} - 7.137710 \times 10^{-2}i & -7.803656 \times 10^{-2} - 2.370657 \times 10^{-2}i \end{pmatrix}$
2° Pan	$\begin{pmatrix} 8.387343 \times 10^{-2} + 1.230910 \times 10^{-2}i & 9.934662 \times 10^{-1} + 7.641068 \times 10^{-2}i \\ -9.934662 \times 10^{-1} + 7.641068 \times 10^{-2}i & 8.387343 \times 10^{-2} - 1.230910 \times 10^{-2}i \end{pmatrix}$
−2° Pan	$\begin{pmatrix} -4.155864 \times 10^{-2} + 2.239486 \times 10^{-2}i & -9.940866 \times 10^{-1} - 9.779177 \times 10^{-2}i \\ 9.940866 \times 10^{-1} - 9.779177 \times 10^{-2}i & -4.155864 \times 10^{-2} - 2.239486 \times 10^{-2}i \end{pmatrix}$
0° Tilt	$\begin{pmatrix} -7.334595 \times 10^{-2} + 2.005534 \times 10^{-2}i & -9.944064 \times 10^{-1} - 7.330761 \times 10^{-2}i \\ 9.944064 \times 10^{-1} - 7.330761 \times 10^{-2}i & -7.334595 \times 10^{-2} - 2.005534 \times 10^{-2}i \end{pmatrix}$
4° Tilt	$\begin{pmatrix} -1.505032 \times 10^{-1} + 2.375270 \times 10^{-2}i & -9.825903 \times 10^{-1} - 1.063053 \times 10^{-1}i \\ 9.825903 \times 10^{-1} - 1.063053 \times 10^{-1}i & -1.505032 \times 10^{-1} - 2.375270 \times 10^{-2}i \end{pmatrix}$
−4° Tilt	$\begin{pmatrix} 4.401511 \times 10^{-3} - 2.038586 \times 10^{-2}i & 9.975089 \times 10^{-1} + 6.738748 \times 10^{-2}i \\ -9.975089 \times 10^{-1} + 6.738748 \times 10^{-2}i & 4.401511 \times 10^{-3} + 2.038586 \times 10^{-2}i \end{pmatrix}$

The average compensation unitaries for the Pentaprism and Periscope assembly are given in Table 3.11.

Table 3.11: Average compensation unitaries

Optic	Average Compensation Unitary
Pentaprism	$\begin{pmatrix} -9.9564 \times 10^{-1} + 7.5123 \times 10^{-2}i & 5.4707 \times 10^{-2} - 7.6006 \times 10^{-3}i \\ -5.4707 \times 10^{-2} - 7.6006 \times 10^{-3}i & -9.9564 \times 10^{-1} - 7.5123 \times 10^{-2}i \end{pmatrix}$
Periscope Assembly	$\begin{pmatrix} 7.2408 \times 10^{-2} - 1.7136 \times 10^{-2}i & 9.9364 \times 10^{-1} + 8.4468 \times 10^{-2}i \\ -9.9364 \times 10^{-1} + 8.4468 \times 10^{-2}i & 7.2408 \times 10^{-2} + 1.7136 \times 10^{-2}i \end{pmatrix}$

3.4.2.3 Residual Matrices and Traces

Table 3.12: Pentaprism absolute RMTs

			Conjugate Unitary					
			Pan			Tilt		
			−7°	7°	0°	0°	4°	−4°
Unitary	Pan	−7°	2.0000	1.9914	1.9978	1.9972	1.9774	1.9800
		7°	1.9914	2.0000	1.9898	1.9976	1.9902	1.9836
		0°	1.9978	1.9898	2.0000	1.9952	1.9809	1.9756
	Tilt	0°	1.9972	1.9976	1.9952	2.0000	1.9824	1.9887
		4°	1.9774	1.9902	1.9809	1.9824	2.0000	1.9502
		−4°	1.9800	1.9836	1.9756	1.9887	1.9502	2.0000

Table 3.13: Periscope assembly absolute RMTs

			Conjugate Unitary					
			Pan			Tilt		
			−2°	2°	0°	0°	4°	−4°
Unitary	Pan	−2°	2.0000	1.9965	1.9980	1.9984	1.9879	1.9977
		2°	1.9965	2.0000	1.9986	1.9988	1.9932	1.9925
		0°	1.9980	1.9986	2.0000	2.0000	1.9934	1.9945
	Tilt	0°	1.9984	1.9988	2.0000	2.0000	1.9928	1.9952
		4°	1.9879	1.9932	1.9934	1.9928	2.0000	1.9769
		−4°	1.9977	1.9925	1.9945	1.9952	1.9769	2.0000

From Table 3.13, it can be seen that the residual matrix for periscope assembly 0° pan and tilt has an RMT of 2, rounding to 4 decimal places. This indicates that their unitaries have a high degree if similarity as they should. The pentaprism 0° pan and tilt RMT has a value of 1.9952, which is substantially different than expected. During testing, the pentaprism was removed from the pan stage and mounted on a new stage to accommodate the tilt measurements, and the periscope assembly was not remounted between pan and tilt tests. Remounting the pentaprism likely caused an erroneous shift relative to the defined frame of reference, inducing experimental errors. Over the RMTs for each optic are relatively similar and near ideal. From the data, it is difficult to discern any overall trends.

3.4.2.4 Bloch Sphere Projection

Figure 3.5 and 3.6 show the measured uncompensated and post compensation states projected onto the rectilinear and diagonal cross section of the Bloch sphere. In the ideal case each arrow would correspond directly with one of the four linear polarization states at 0°, 90°, 180°, 270° representing D, H, A, V respectively. In this format, the unitary compensation rotation can be seen to rotate all states about the Bloch sphere. These rotations are not purely about the 2D plane's central axis. Some of projected vectors appear to shift relative to each other due to the applied rotation's out of plane components.

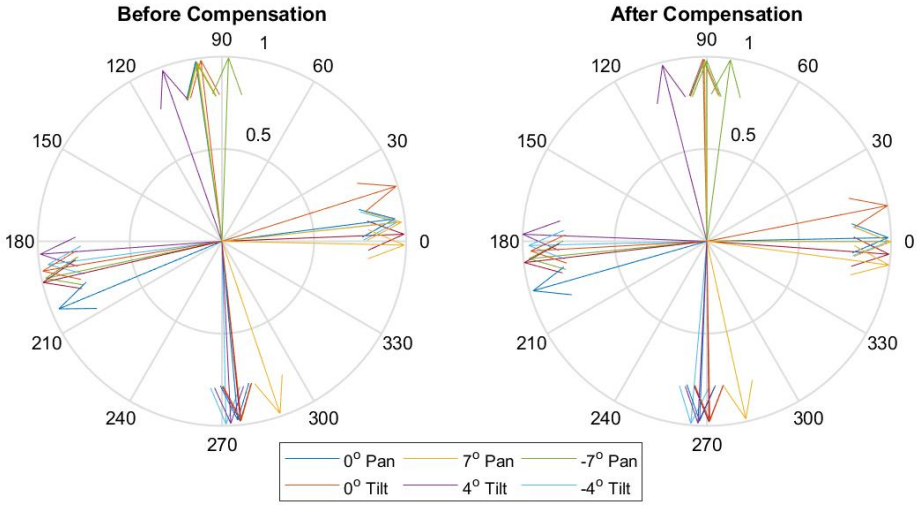

Figure 3.5: *Pentaprism Bloch sphere projections for incoming pan and tilt angles*

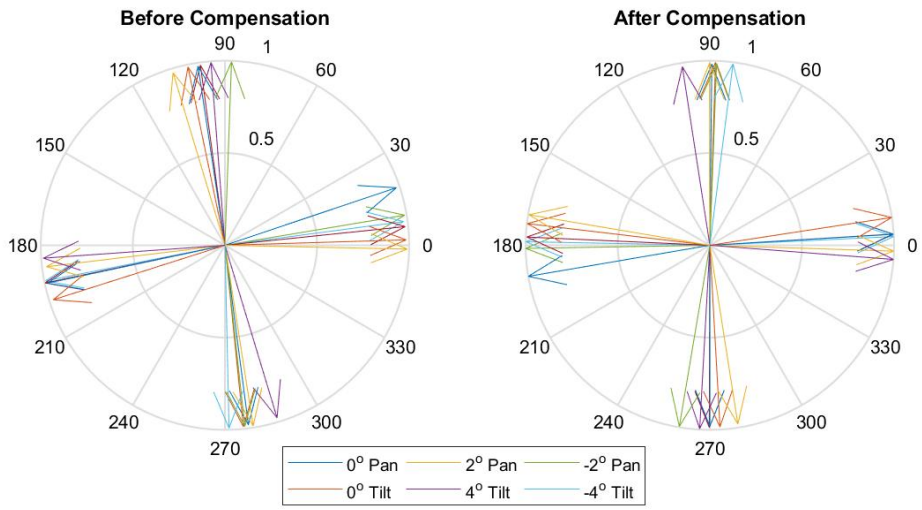

Figure 3.6: *Periscope assembly Bloch sphere projections for incoming pan and tilt angles*

3.4.2.5 QBER

The uncompensated and compensated QBER results are given for both characterized optics in the tables below.

Table 3.14: Pentaprism pan uncompensated and compensated QBER

		QBER		
		Measured	Poln Calculated	Compensated
Pan Angle	0°	1.64996%	1.7979%	1.023%
	7°	1.60166%	1.8963%	0.91603%
	−7°	1.19797%	1.2274%	1.0158%

Table 3.15: Pentaprism tilt uncompensated and compensated QBER

		QBER		
		Measured	Poln Calculated	Compensated
Tilt Angle	0°	1.46105%	1.461%	1.0581%
	4°	3.84690%	3.8737%	2.0007%
	−4°	1.46419%	1.4642%	1.8868%

Table 3.16: Periscope assembly pan uncompensated and compensated QBER

		QBER		
		Measured	Poln Calculated	Compensated
Pan Angle	0°	1.19880%	1.2786%	0.40885%
	2°	1.42494%	1.4249%	0.48920%
	−2°	0.91472%	0.9651%	0.39053%

Table 3.17: Periscope assembly tilt uncompensated and compensated QBER

		QBER		
		Measured	Poln Calculated	Compensated
Tilt Angle	0°	1.16614%	0.9651%	0.45002%
	4°	2.91631%	3.3459%	1.1515%
	−4°	0.47140%	0.4995%	0.72238%

As can be seen from Tables 3.14 - 3.17, the measured QBER and the Poln calculated QBER tend to be similar. The two exceptions to this are pentaprism 7° pan angle and periscope assembly 4° tilt which differ by roughly 0.3% and 0.4% respectively. This is likely due to factors considered in the algorithm, such as the L and R polarizations, not considered by the simple measured QBER calculation.

The measured and Poln calculated uncompensated QBER, show no discernible underlying trend for either the pentaprism or periscope assembly. These uncompensated QBER values from the table above do not indicate any underlying angular dependence. Furthermore, the centre value (0° pan, 0° tilt) often does not correspond to the least erroneous angle, which should theoretically be the case as mentioned in Section 3.2.5. Because this manual characterization study did not result in data of significant meaning, the characterization process was redone with a semiautomated system.

A QBER tilt angular dependence was discovered as part of the automated characterization tests and beam steering simulation. This trend is described further in Section 3.5 and 3.6. In summary, their results indicate that changes in the incoming tilt angle increase the QBER significantly more than changes in the pan angle do. This was seen consistently through each of the characterized optics.

By further inspection of the compensated QBER data collected during this manual characterization experiment, the tilt dependence trend can also be seen. Changes of pan

angle for both the pentaprism and periscope assembly only have slight changes on the compensated QBER. Tilt angle variations cause significant changes in the compensated QBER, and in some cases doubling it. These results were noticed in hindsight after performing the automated characterization tests and beam steering simulation.

3.5 Automated Characterization Method

There was a selection of error sources in the manual characterization process that may have interfered with the experiment's accuracy. The previous version of the experiment was done in room light with an optical band pass filter to reduce the background light. Because the filter will still let some light through, it was beneficial to perform the experiment again in a dark room with background light subtraction. 532 nm laser light was used in the manual characterization configuration where as the OGR system is designed for 785 nm light. Because of this, it was desirable to perform the experiment again with a wavelength closer that used by OGR in case the results have a wavelength dependence. Additionally, there are errors associated with the setting of half and quarter waveplate angles between measurements reducing the experimental accuracy. By automating the measurement process, these errors can be reduced as well as several measurements can be taken at a particular angle and averaged to increase measurement accuracy. These changes were implemented and the experiments were redone using automated motorized optic rotation mounts.

3.5.1 Experimental Setup

A 780 nm laser was used to characterize the polarization distortion induced by the test optics. The laser light was coupled in to an optic fibre (1) attached to a collimator and a linear polarizer (3) attached to a motorized rotation stage (2). The polarized light was then passed through the optic under test then towards the detector assembly. In 3.7 no test optic is displayed as it shows the basic straight through path. In the detector assembly, the beam first passes through an aperture (4) followed by a QWP (5) and a linear polarizer (6), each on motorized rotation stages. After passing through the measurement selection optics, the beam then reaches the power meter (7).

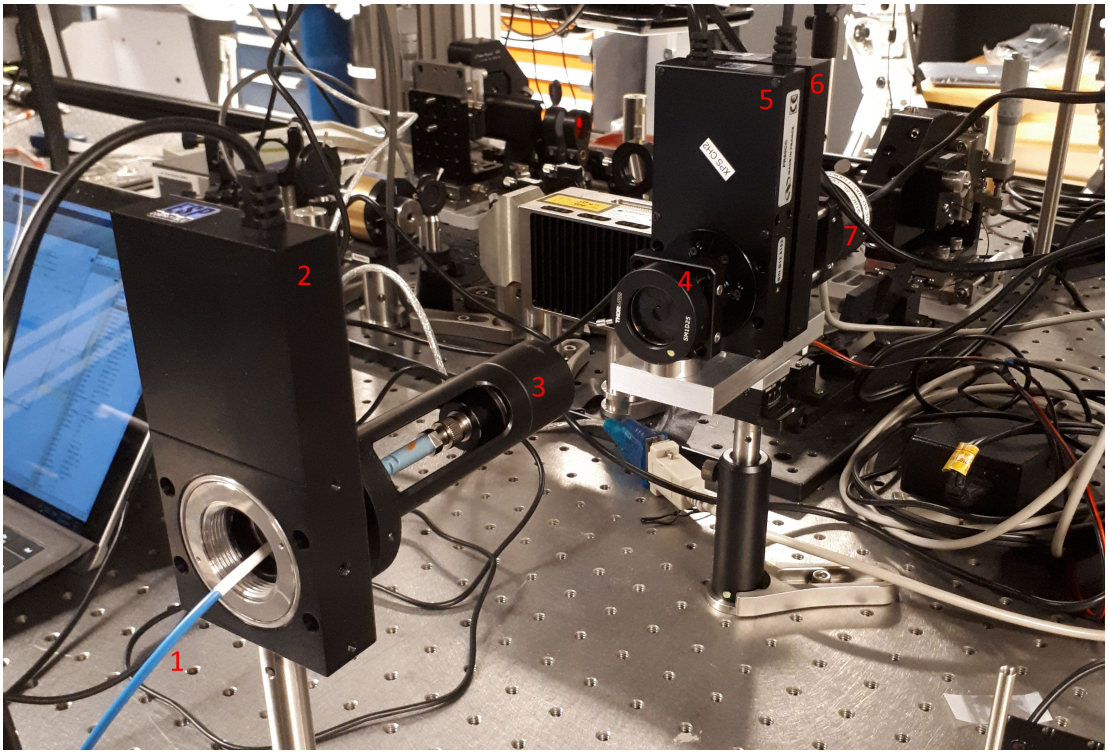

Figure 3.7: *The straight through path characterization setup is given as an example of the automated characterization system*

The automated characterization setup varies from that of the manual configuration in several ways. The automated setup was configured to transmit H, V, D, and A polarizations whilst being able to measure H, V, D, A, R, and L polarizations. This configuration was chosen as it only requires one automated rotation stage for polarization state preparation, simplifying the transmission optics. The laser transmission fibre, collimator, and polarizer can then be affixed to the just one rotation stage. Having the optical fibre rotate with the polarizer, reduces any polarization bias effects the optical fibre may have, reducing the incoming optical power variations. Instead of having a QWP and HWP along with a fixed PBS for the six state selection, the automated setup utilized a QWP and linear polarizer to reduce the amount of optics required. The laser power for the automated setup was given to be more stable than the laser power used during manual characterization. Because of this and the measurement averaging, a reference power measurement was not required.

For the rectilinear basis measurements, the QWP is set to 0° causing it to have no effect, allowing the polarizer to act directly on the H and V polarizations. The QWP is set to 45° for measurements in the diagonal basis. In this configuration, the diagonal basis acts as if it were the rectilinear basis interacting with a QWP at 0° due to the global 45° rotation experienced by both the basis and QWP. The polarizer is then set to −45° and

45° to measure the D and A polarizations respectively. For the circular basis, the QWP is set to 45°. This rotates the circular polarizations into linear polarizations, transforming R and L to H and V respectively. These rotation configurations are summarized in Table 3.18.

Table 3.18: QWP and polarizer orientations for polarization measurement

		QWP (5) angle	Polarizer (6) angle
Polarization	H	0°	0°
	V	0°	90°
	D	45°	−45°
	A	45°	45°
	R	45°	0°
	L	45°	90°

The test optic was placed between the transmission system and polarization measurement assembly on a manual tilt stage and rotation mount. The incoming beam pan and tilt angles were set by manually rotating and tilting the optic on its stage. The polarization measurement assembly was positioned such that the outgoing beam passed through it and the measured power intensity was maximized. Adjusting the optic's orientation caused the outgoing beam to wander, thus the measurement assembly needed to be mobile so it could properly capture the outgoing beam. Because of this, the measurement assembly was mounted to a tilt stage on a movable post so it could swivel, tilt, and translate.

One set of reference measurements were taken for the straight through path without any beam steering optics. Four different beam steering optics were characterized; a pentaprism, periscope assembly, single mirror, and set of double mirrors in a pentaprism like configuration as described in Section 3.2.

Each optic under test was characterized over 9 different incoming angles. For most optics, these measurements were taken at +4°, 0°, and −4° pan angles and at each pan angle the tilt angles of +4°, 0°, and −4° were measured. The specifics for each optic are given in Table 3.1. For each angle 24 different polarization measurements were taken such that each of the 4 transmission polarizations were measured over the 6 different measurement polarizations. The average of 5 power meter readings were used for one polarization measurement.

All the measurements were performed in a dark room to minimize the amount of ambient light. Furthermore, a set of background measurements were taken before data acquisition, and background subtraction was utilized to reduce measurement noise.

Due to slight differences between the input beam direction of propagation and its motorized rotation stage, the incoming beam happened to wander slightly on the detector during the characterization process. This might have induced artificial input polarization dependent power loss. Because of this, the measured powers were normalized based on average measured power for each input polarization at a given angle.

3.5.2 Results

3.5.2.1 Relative Intensities

The relative intensity tables are not presented here for the automated characterization section as they are too numerous and would to lose value if presented in bulk form.

3.5.2.2 Modeled Unitaries

The average compensation unitary for each characterization setup is given below in Table 3.19. These unitaries were calculated via the method described in Section 3.3.1 developed by Higgins et. al. [70]. In general, there is a high correlation between the average unitary and its ideal with an applied global phase shift. This is made more apparent in Section 3.5.2.3.

Table 3.19: Average compensation unitaries

Setup	Average Compensation Unitary	Ideal
Straight Through Path	$\begin{pmatrix} -1.0000 + 0.0013i & 0.0026 + 0.0068i \\ -0.0026 + 0.0068i & -1.0000 - 0.0013i \end{pmatrix}$	$\begin{pmatrix} 1 & 0 \\ 0 & 1 \end{pmatrix}$
Pentaprism	$\begin{pmatrix} -0.9995 - 0.0250i & 0.0162 - 0.0135i \\ -0.0162 - 0.0135i & -0.9995 + 0.0250i \end{pmatrix}$	$\begin{pmatrix} 1 & 0 \\ 0 & 1 \end{pmatrix}$
Periscope Assembly	$\begin{pmatrix} 0.0361 - 0.0286i & 0.9955 + 0.0826i \\ -0.9955 + 0.0826i & 0.0361 + 0.0286i \end{pmatrix}$	$\begin{pmatrix} 0 & 1 \\ -1 & 0 \end{pmatrix}$
Single Mirror	$\begin{pmatrix} -0.1980 + 0.9772i & 0.0037 + 0.0766i \\ -0.0037 + 0.0766i & -0.1980 - 0.9772i \end{pmatrix}$	$\begin{pmatrix} 1 & 0 \\ 0 & -1 \end{pmatrix}$
Double Mirror	$\begin{pmatrix} -0.9955 - 0.0901i & 0.0300 - 0.0069i \\ -0.0300 - 0.0069i & -0.9955 + 0.0901i \end{pmatrix}$	$\begin{pmatrix} 1 & 0 \\ 0 & 1 \end{pmatrix}$

3.5.2.3 Residual Matrices and Traces

To help show and characterize the relation between the average unitary and its ideal, the complex conjugate of the average unitary is multiplied by its ideal unitary. The absolute value of the resulting matrix trace is taken, as shown in Equation 3.7. This process is similar to that used to calculate RMT. These results, along with the average of the residual absolute traces are listed for each characterization setup in Table 3.20.

$$\left| Tr\left[U'_{avg} \cdot U_{ideal} \right] \right| \tag{3.7}$$

Table 3.20: Average of the RMTs and traces with ideal unitaries

Optic	Average Residual Unitary Trace	Unitary With Ideal Trace
Straight Path	1.9999	1.9999
Pentaprism	1.9937	1.9989
Periscope Assembly	1.9942	1.9910
Single Mirror	1.9914	1.9544
Double Mirror	1.9940	1.9909

The RMTs for each optic and incoming angle were taken to characterize the effect of incoming angle variation. This calculation creates a 9 by 9 matrix consisting of the RMTs. The diagonal terms all have a trace of 2 as they are calculated using a unitary and its inverse. Each off-diagonal component will have a diagonally symmetric counterpart that is calculated using the same unitaries, but in opposite order. The RMT value is the same independent of the order of the unitaries as shown by Equations 3.8 - 3.12.

$$U_1^\dagger \cdot U_2 = \left(U_2^\dagger \cdot U_1\right)^\dagger \tag{3.8}$$

$$Tr\left[U_1^\dagger \cdot U_2\right] = Tr\left[\left(U_2^\dagger \cdot U_1\right)^\dagger\right] \tag{3.9}$$

$$Tr\left[U_1^\dagger \cdot U_2\right] = Tr\left[U_2^\dagger \cdot U_1\right]^\dagger \tag{3.10}$$

$$\left|Tr\left[U_1^\dagger \cdot U_2\right]\right| = \left|Tr\left[U_2^\dagger \cdot U_1\right]^\dagger\right| \tag{3.11}$$

$$\left|Tr\left[U_1^\dagger \cdot U_2\right]\right| = \left|Tr\left[U_2^\dagger \cdot U_1\right]\right| \tag{3.12}$$

Because of the off-diagonal symmetry, only one half of the RMT values are shown in Figures 3.8 - 3.11. The calculated averages for the residuals given in Table 3.20, are taken from only the off-diagonal components as the diagonal components are all trace 2 and therefore would skew the average. In the figures below, the values are plotted as 2 minus the RMT, as to better display the differences in values.

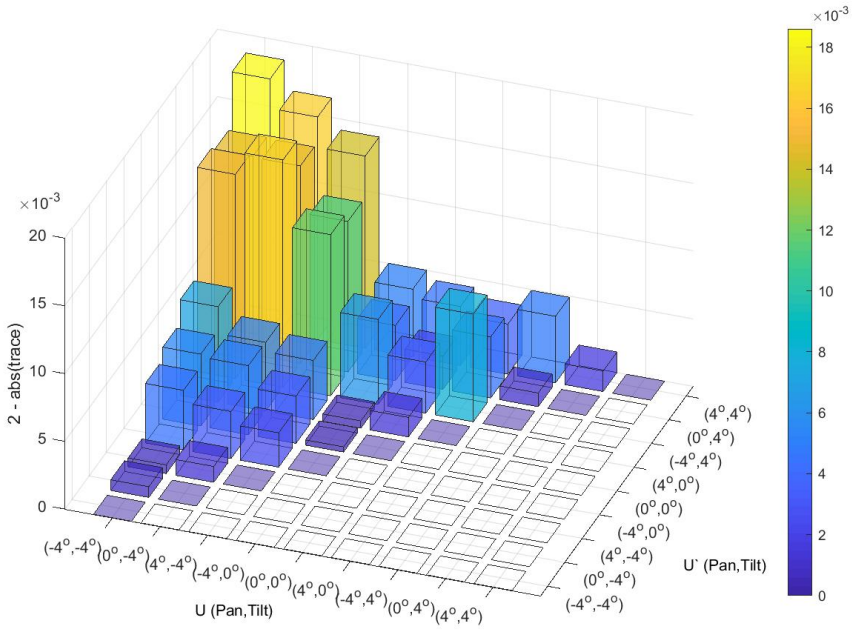

Figure 3.8: *Pentaprism absolute value of the RMT, presented as 2 - RMT for better visualization*

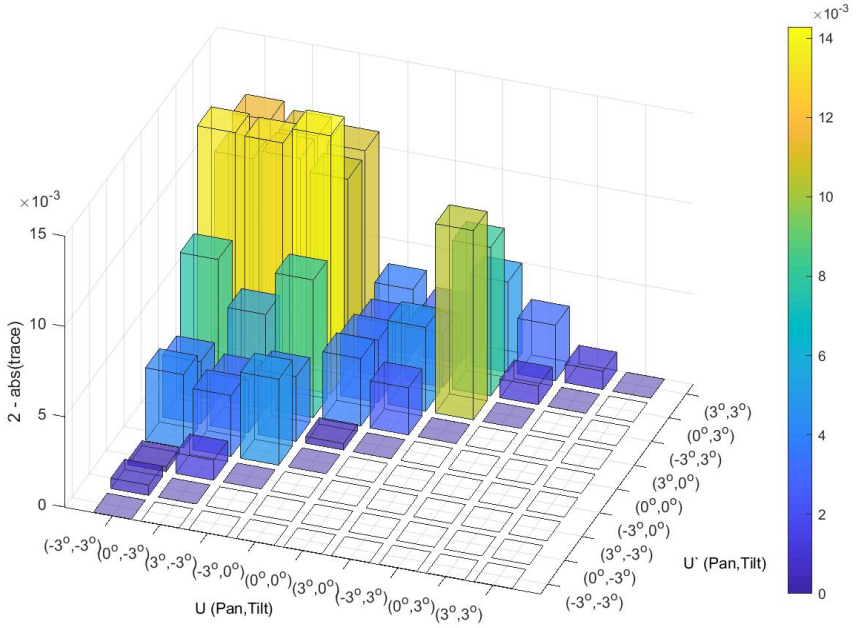

Figure 3.9: *Periscope assembly absolute value of the RMT, presented as 2 - RMT for better visualization*

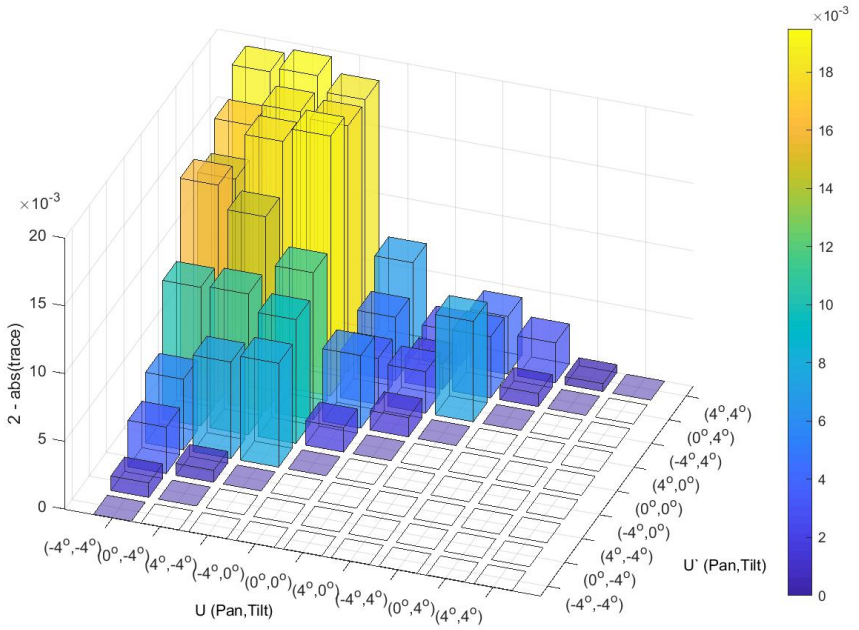

Figure 3.10: *Single mirror absolute value of the RMT, presented as 2 - RMT for better visualization*

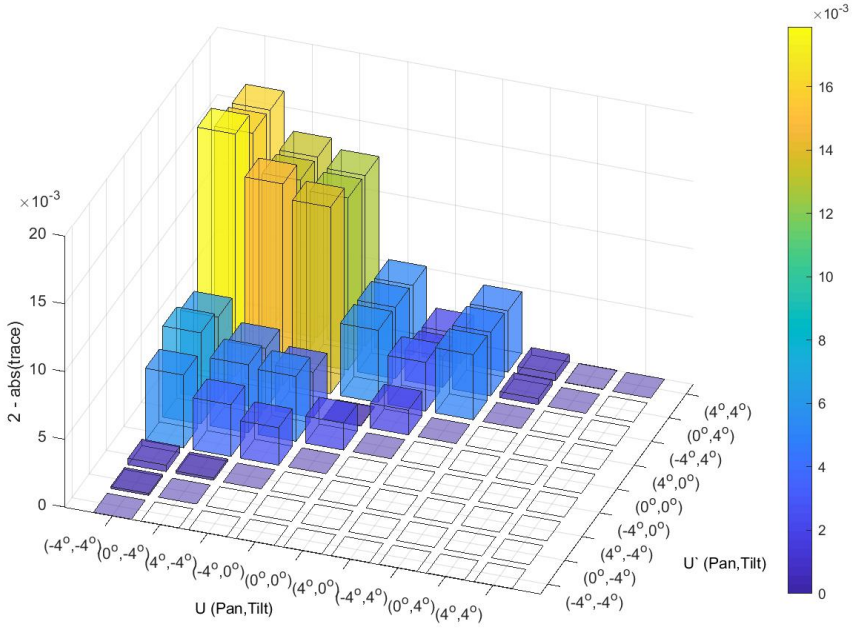

Figure 3.11: *Double mirror absolute value of the RMT, presented as 2 - RMT for better visualization*

The RMTs for all the optics given in Figures 3.8 - 3.11 show very similar distributions. They all show a strong angular tilt dependence. The reduction in RMT appears to scale strongly with the difference between the tilt angles for the unitaries used. The RMTs for the unitaries of opposite tilt angles are consistently the lowest with minimal pan dependence. This is presented in Figures 3.8 - 3.11 by the 3 by 3 section of tall bars, shown at the rear left corner in the figures as these plots depict 2 minus the RMT. The data was presented in this format to depict the RMT deviation from ideal.

RMTs corresponding to the intersection of no tilt with top and bottom tilts are the next most significant. These regions are shown in the middle left and middle back of the figures. In contrast, there are only slight trends with increasing pan angles which are inconsistent between different optics.

The tested optics are positioned such that they steer the beam in the horizontal plane, which is the same plane associated with pan angle adjustments. Therefore, tilt adjustments cause the beam to experience reflections that are not in the ideal plane of reflection, whereas pan adjustments do not. It is theorized that the tilt dependence trend is due to this difference between the pan and tilt incoming angles.

There are a selection of periscope assembly RMTs in Figure 3.9 that deviate from the general trend. These values correspond to the row and column that are based on the $(3°, 0°)$ incoming angle, indicating that it is the plausible source of error. Because the errors are all associated with the one incoming angle, they are likely due to an experimental error such as beam clipping or accidental reflections for that set of polarization measurements.

3.5.2.4 Bloch Sphere Projections

Figures 3.12 - 3.15 below show the Bloch sphere state projections as previously discussed in Section 3.4.2.4. The 9 different projections for each angle rotate about the sphere equally due to the shared unitary compensation.

It is fairly common to see the projection arrows oriented together in three groups organized by incoming tilt angles. The middle of these groupings regularly corresponds to 0° tilt, while the outer collections correspond separately to positive or negative tilts. A strong example of this is the uncompensated periscope assembly projections near 0° in Figure 3.13. This reinforces the tilt dependence which is discussed in further detail later in Section 3.5.2.5.

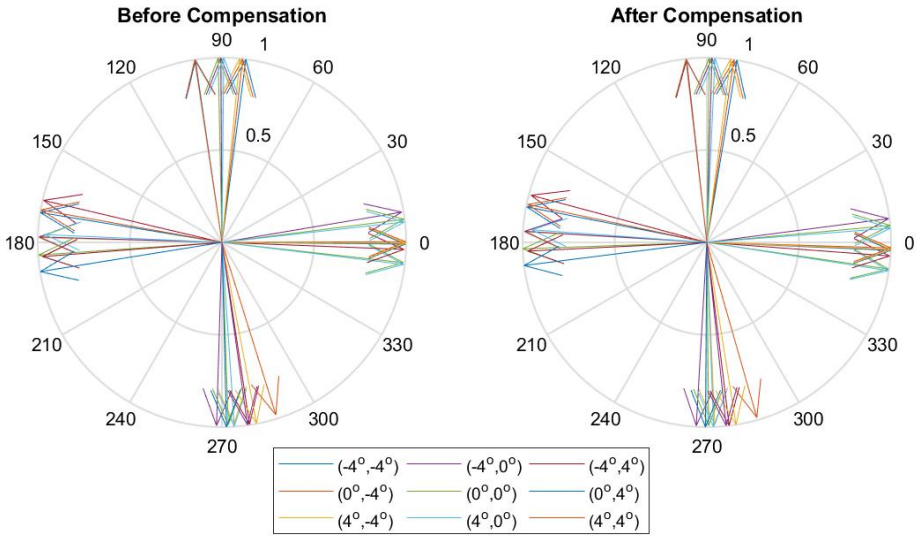

Figure 3.12: *Pentaprism Bloch sphere projections for incoming pan and tilt angles*

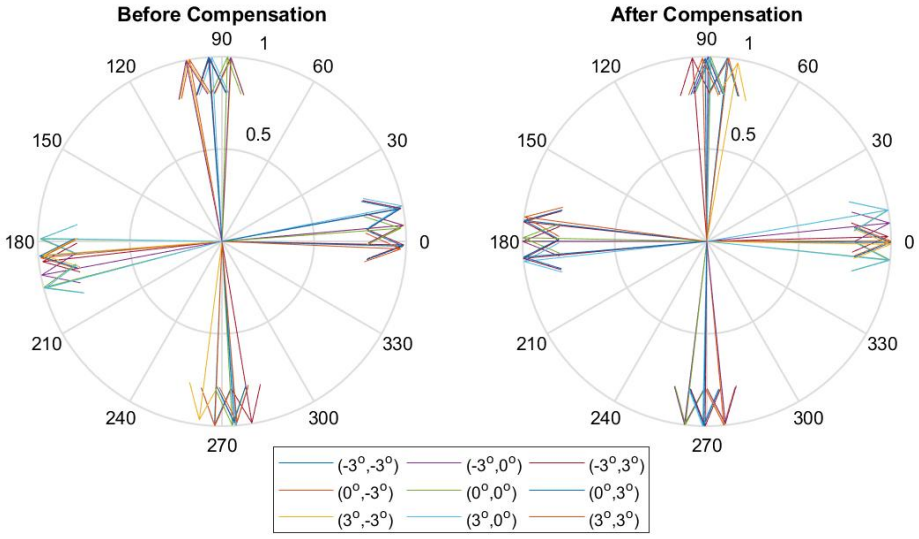

Figure 3.13: *Periscope assembly Bloch sphere projections for incoming pan and tilt angles*

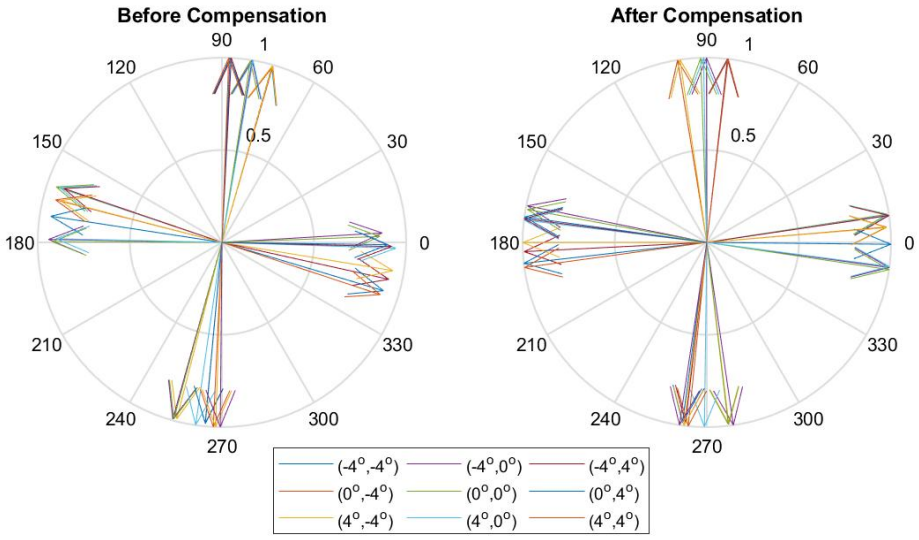

Figure 3.14: *Single mirror Bloch sphere projections for incoming pan and tilt angles*

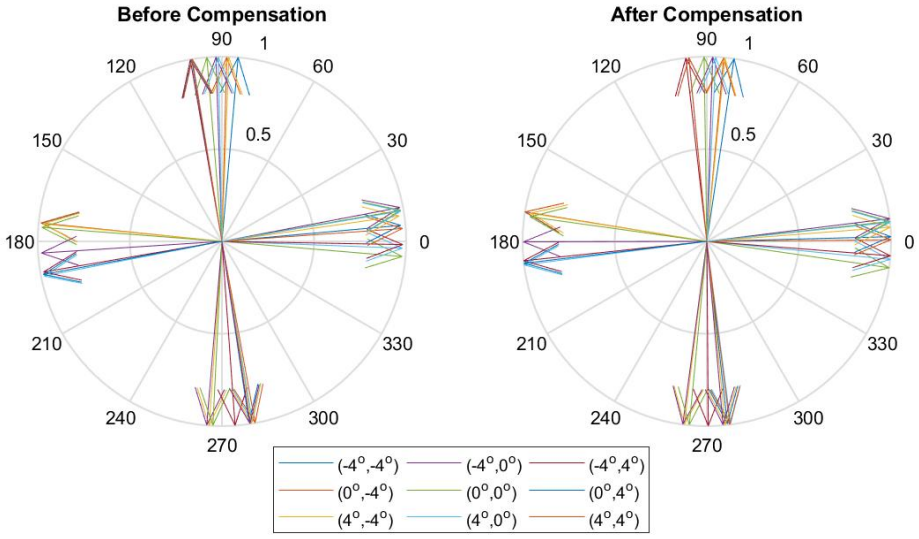

Figure 3.15: *Double mirror Bloch sphere projections for incoming pan and tilt angles*

3.5.2.5 QBER

The QBER for each incoming angle was also calculated, the averages for each optic are given in Table 3.21.

Table 3.21: Average and compensated QBER

Optic	Average QBER	Compensated QBER
Straight Path	0.0084 %	0.0054 %
Pentaprism	0.5095 %	0.4647 %
Periscope Assembly	0.7460 %	0.2246 %
Single Mirror	2.9420 %	0.3805 %
Double Mirror	0.7883 %	0.3177 %

Since the straight through path does not measure any optic, it effectively measures any inherent bias in the characterization setup. Because of this, it is important to have both the QBER and RMT values near their ideals of 0 and 2, respectively for this measurement. Their values are reasonably close to their ideals listed in Tables 3.20 and 3.21, indicating that the straight through path has minimal polarization distortion. Its measured QBER is roughly two orders of magnitude below that of the next lowest QBER indicating that the errors due to optical alignment and measurement accuracy are minimal.

Because the straight through path is purely linear and it has no angular dependence, not all 9 angular combinations were tested for the straight through path. Instead, 4 different polarization measurement sets were run. The optical alignment was broken and reset between each of these test runs. This was done to include any manual alignment induced errors, as each optical alignment is different. If there was a strong alignment dependence, then there would be large QBER differences between each test. As shown in Figure 3.16, the variation in QBER between tests is apparent, but overall fairly low indicating that the alignment biases are minimal.

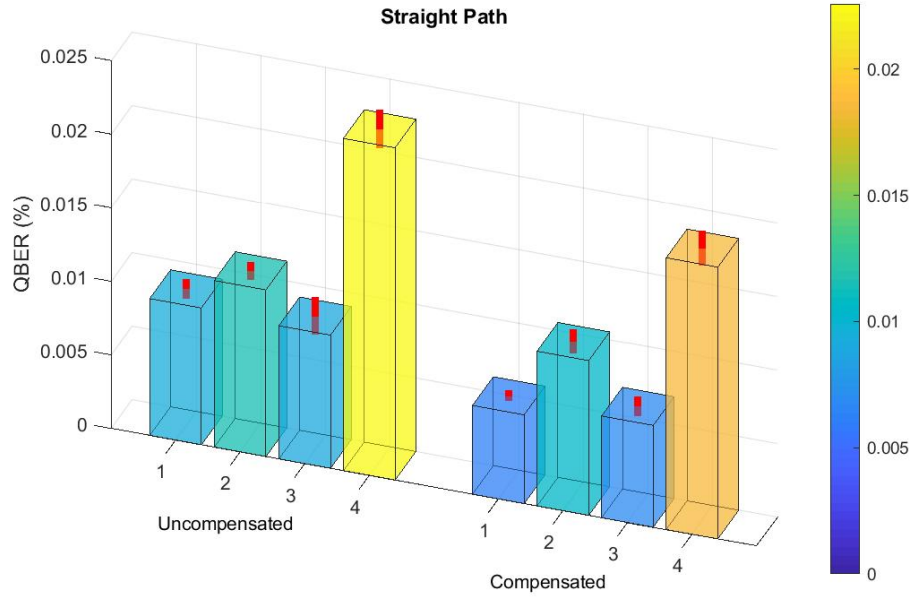

Figure 3.16: *Straight through path uncompensated and compensated QBER. Each bar is labeled with its associated test number, as there is no angular dependence for the straight though case. The red lines show the 95% confidence interval for the QBER measurement and determination. The numbers on the horizontal axis indicate the test number as there is not angular dependence for the straight through path.*

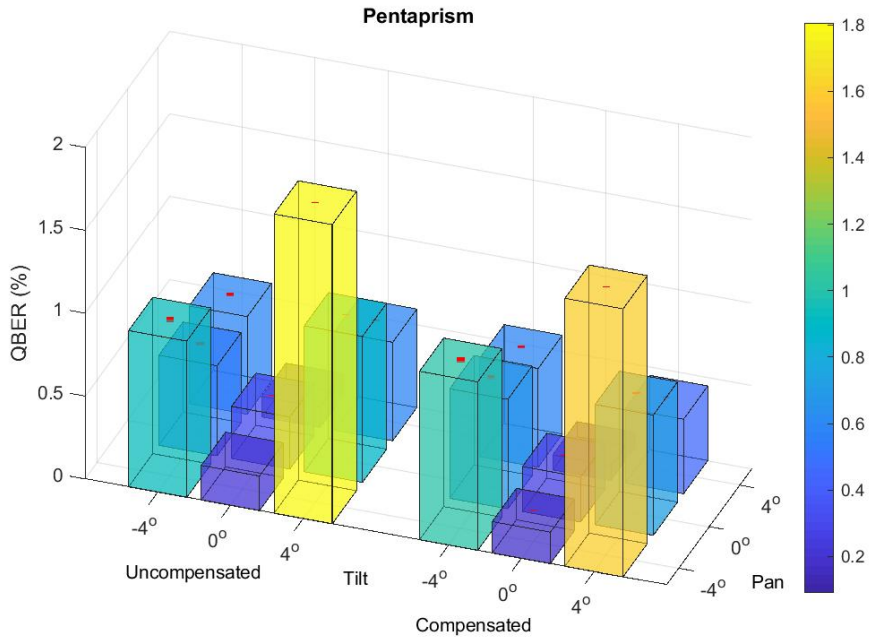

Figure 3.17: *Pentaprism uncompensated and compensated QBER. The red lines show the 95% confidence interval for the QBER measurement and determination.*

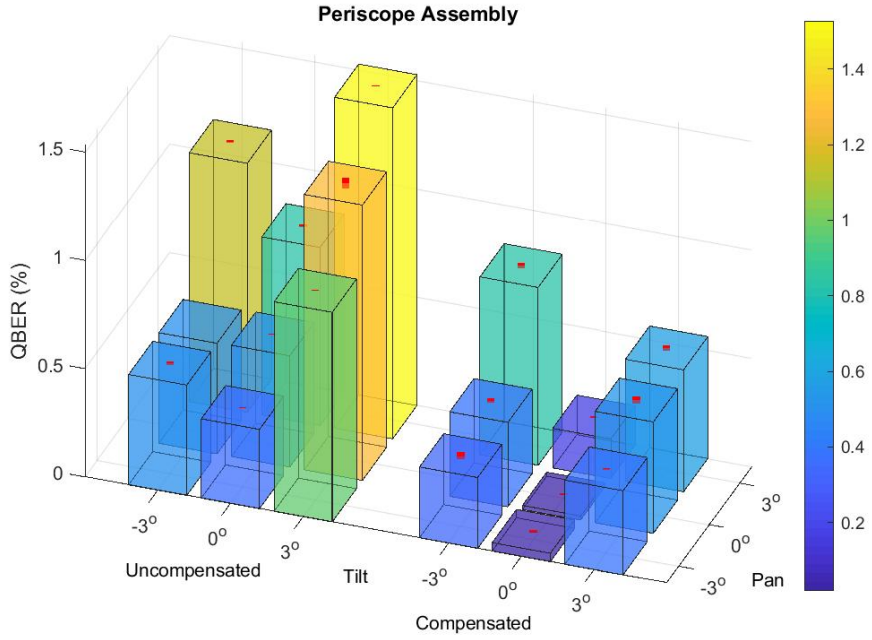

Figure 3.18: *Periscope assembly uncompensated and compensated QBER. The red lines show the 95% confidence interval for the QBER measurement and determination.*

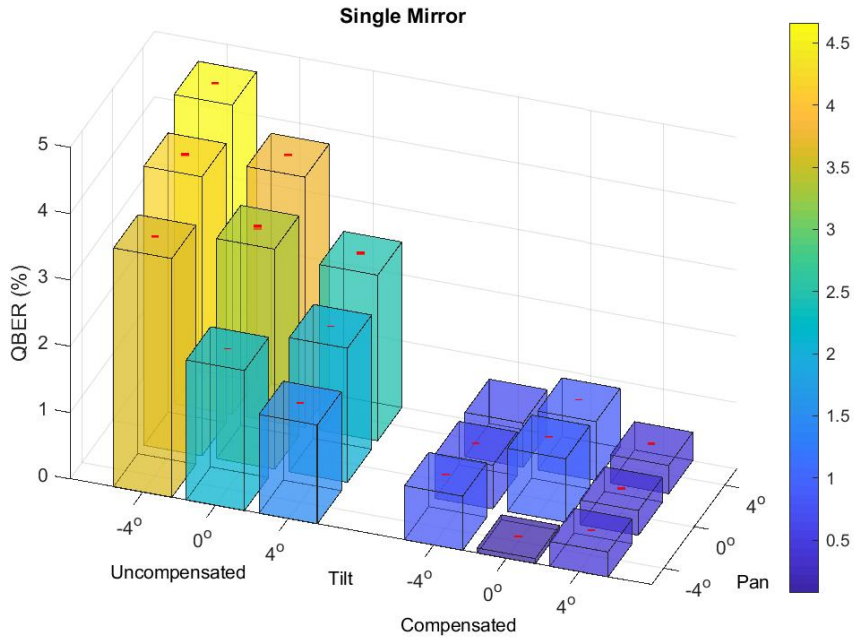

Figure 3.19: *Single mirror uncompensated and compensated QBER. The red lines show the 95% confidence interval for the QBER measurement and determination.*

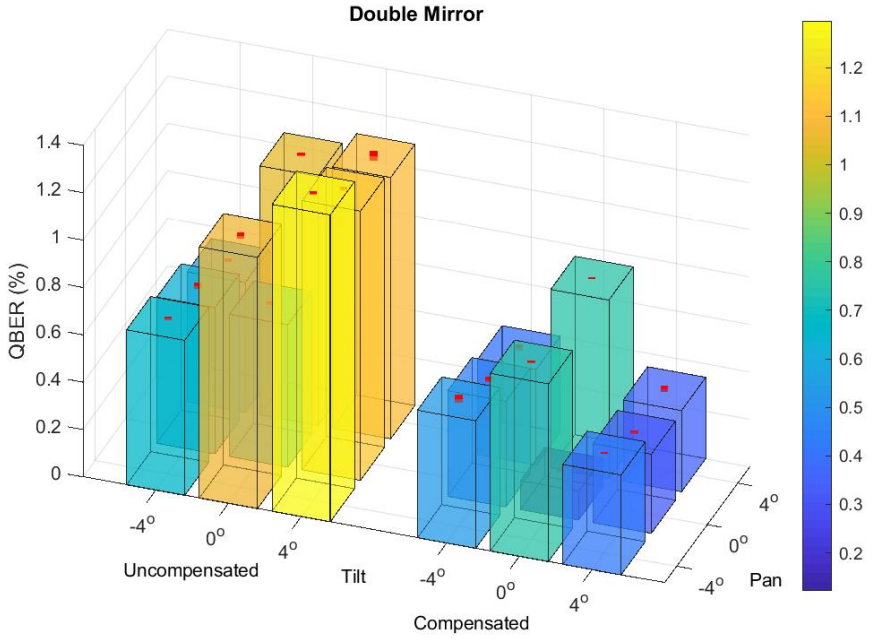

Figure 3.20: *Double mirror uncompensated and compensated QBER. The red lines show the 95% confidence interval for the QBER measurement and determination.*

The strong tilt dependence of the compensation unitary as discussed earlier is also visible in QBER distributions seen throughout Figures 3.17 - 3.20. This effect is made more apparent in the compensated QBER bar plots. For a single tilt angle, the various different pan angles have a similar compensated QBER for a particular optic in general. This does not hold for the inverse case. For a fixed pan angle, the QBER differs greatly between various tilt angles. This gives credence to there being a strong birefringence variation associated with the tilt angle.

If an optic's birefringence has a high degree of tilt dependence, there would be a significant difference between the unitaries used to describe the optic's effect at various angles. This would also correspond to variations in the compensation unitaries, which is seen in the RMT tilt trends demonstrated previously. Furthermore, if there were a tilt dependent birefringence, then correcting over multiple tilt angles with a single unitary will have a reduced accuracy. As a result, there would be substantial differences in compensated QBER over various different tilt angles. This is seen throughout all the optics characterized, indicating their strong tilt dependent birefringence variation.

Figures 3.21 - 3.24 depict the difference between the measured QBER and the Poln calculated QBER. Both methods produce QBER values that tend to be very similar to each other. However, there are some data points that are significantly different than their counterpart. Because there are only two methods compared, it is difficult to identify which more properly describes the system.

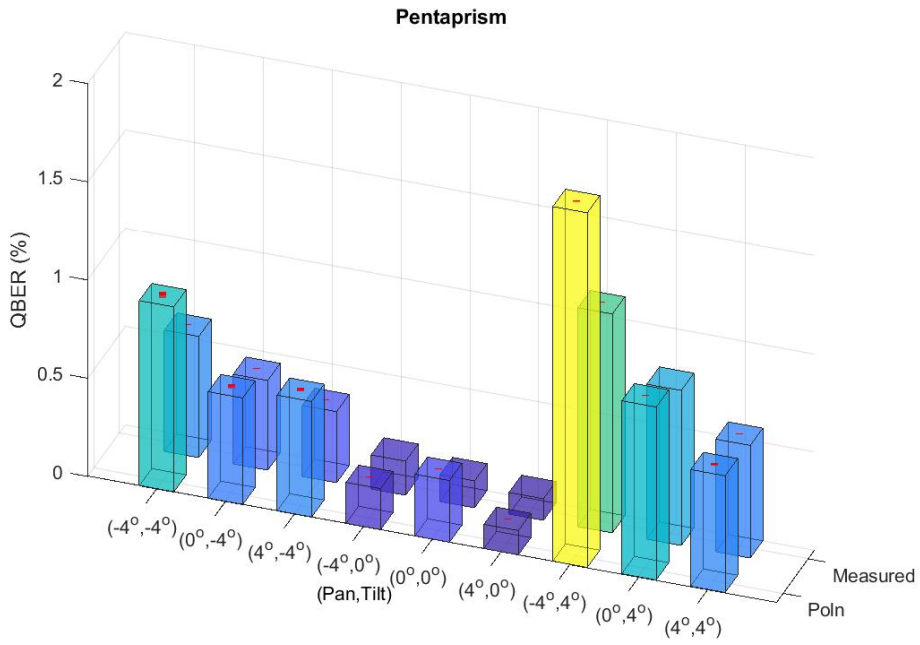

Figure 3.21: *Pentaprism QBER determination method comparison. The red lines show the 95% confidence interval for the QBER measurement and determination.*

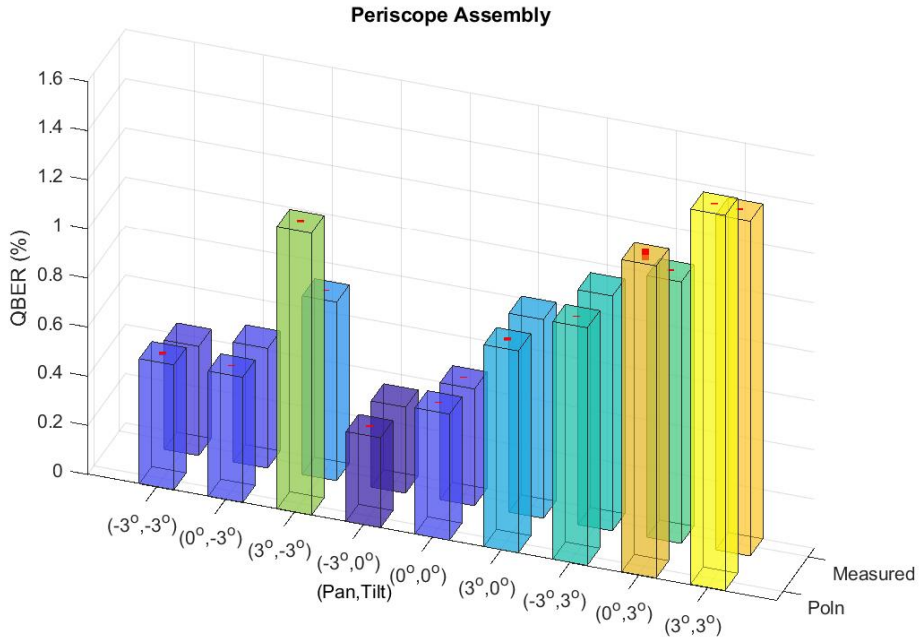

Figure 3.22: *Periscope assembly QBER determination method comparison. The red lines show the 95% confidence interval for the QBER measurement and determination.*

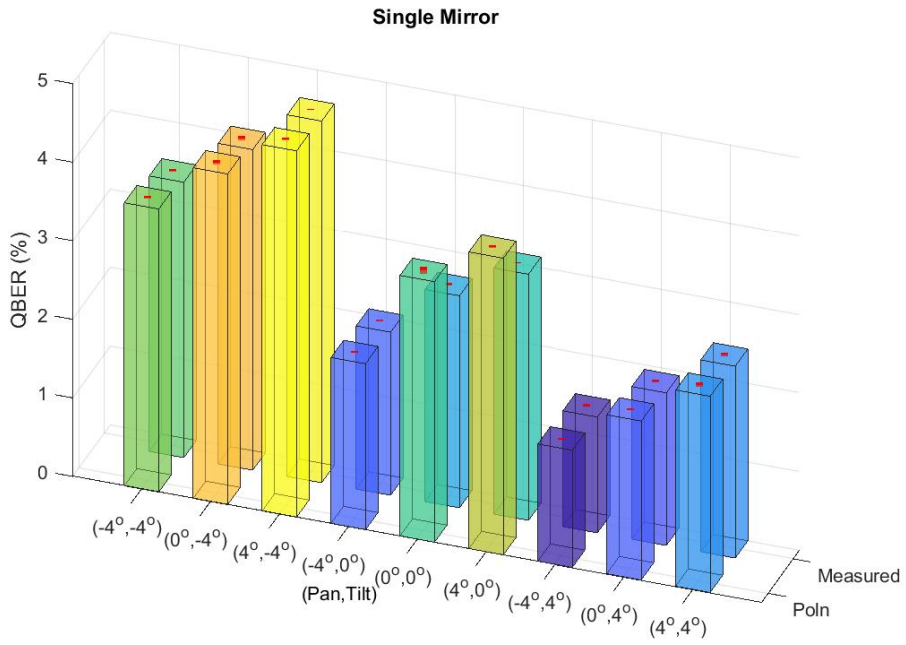

Figure 3.23: *Single mirror QBER determination method comparison. The red lines show the 95% confidence interval for the QBER measurement and determination.*

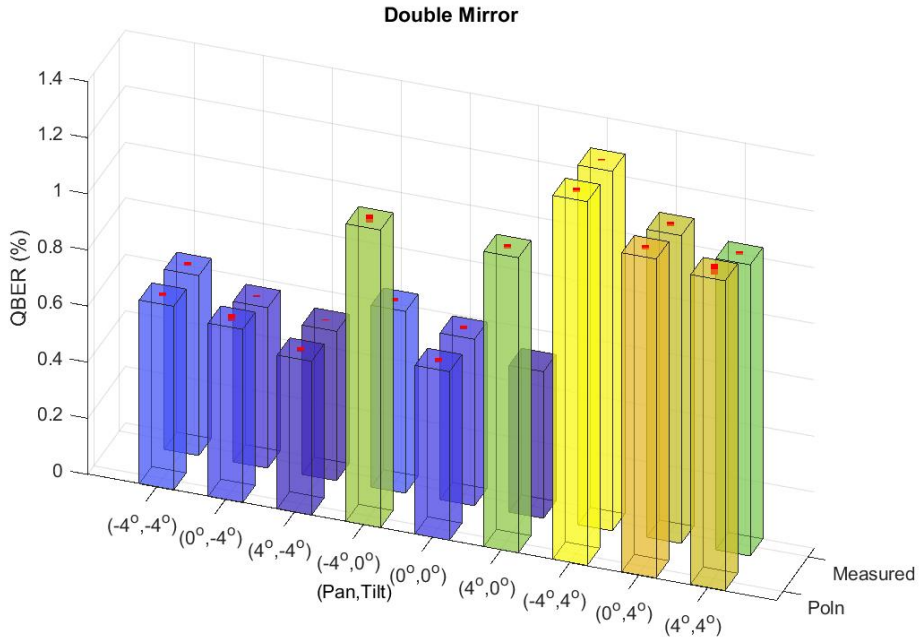

Figure 3.24: *Double mirror QBER determination method comparison. The red lines show the 95% confidence interval for the QBER measurement and determination.*

The main reason for the discrepancy between the two methods is that the measured QBER only takes into account 8 different measurements whereas the Poln calculated QBER is based on all 24 measurements. Two examples of the discrepancies are the $-4°$ pan $0°$ tilt and the $4°$ pan $0°$ tilt cases for the double mirror system presented in Figure 3.23. The discrepancy can be explained more by investigating the power measurement data for these incoming angles. Other cases such as the $0°$ pan $0°$ tilt and the $-4°$ pan $4°$ tilt have minimal QBER discrepancies between the two methods. The measured power for these incoming angles are given in Figure 3.26 as method independent QBER references.

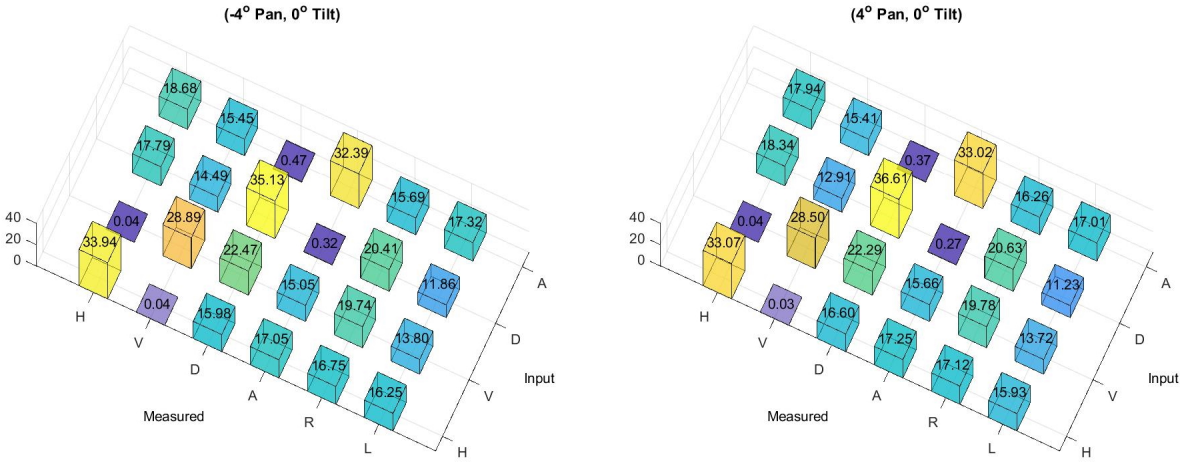

(a) $-4°$ *Pan,* $0°$ *Tilt* **(b)** $4°$ *Pan,* $0°$ *Tilt*

Figure 3.25: *The measured power at various polarizations for a selection of double mirror incoming angles. These figures are given as an example of measurements that correspond to method dependent QBER values. The values are given in arbitrary units*

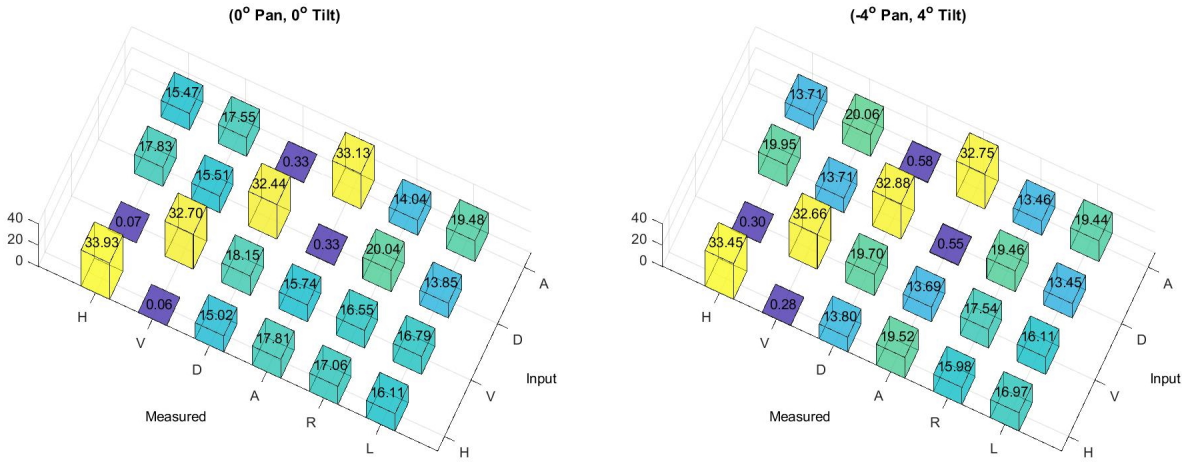

(a) $0°$ *Pan,* $0°$ *Tilt* **(b)** $-4°$ *Pan,* $4°$ *Tilt*

Figure 3.26: *The measured power at various polarizations for a selection of double mirror incoming angles. These figures are given as an example of measurements that correspond to method independent QBER values. The values are given in arbitrary units*

By looking at the input states measured in the incorrect basis, differences between the angles that have QBER discrepancies and those that do not can be explained. In the ideal case, an input state measured in an orthogonal bases should produce even power in both states of the measured basis. The experimental results however, have a natural imbalance of power when measured in the off-basis states and therefore do not produce balanced measurements. Taking the $0°$ pan, $0°$ tilt case as an example, the input A state measured in V is greater than when A is measured in H. The opposite is true for the D input state as shown in Figure 3.26 and Table 3.22. The H and V measurements are given here as an example, but similar effects can also be seen for the R and L measurements.

Since the ideal A and D input states oppose each other on the Bloch sphere, they should ideally rotate about the Bloch sphere such that they are always opposite of each other. Because of this, a rotation that shifts the A state towards V, should also rotate the D state towards H. This type of relation should also hold true for the H and V input states, as well as the R and L input states, but only the D and A cases are given as an example.

If D and A are in opposition, the orthogonal basis power ratio of $\frac{\langle H|M|A\rangle}{\langle V|M|A\rangle}$ should be the same as $\frac{\langle V|M|D\rangle}{\langle H|M|D\rangle}$. The $0°$ pan, $0°$ tilt and $-4°$ pan, $4°$ tilt double mirror angles show this relation nicely and are given as an ideal example in Table 3.22. The Poln calculated QBER agrees strongly with that of the measured QBER for these angle measurements as seen in Figure 3.24.

Table 3.22: Orthogonal basis power ratios for the double mirror examples of QBER calculation method independent angles

0° Pan, 0° Tilt	−4° Pan, 4° Tilt
$\frac{\langle H\|M\|A\rangle}{\langle V\|M\|A\rangle} = \frac{15.47}{17.55} = 0.8815$	$\frac{\langle H\|M\|A\rangle}{\langle V\|M\|A\rangle} = \frac{13.71}{20.06} = 0.6849$
$\frac{\langle V\|M\|D\rangle}{\langle H\|M\|D\rangle} = \frac{15.51}{17.83} = 0.8699$	$\frac{\langle V\|M\|D\rangle}{\langle H\|M\|D\rangle} = \frac{13.71}{19.95} = 0.6872$

For the QBER calculation method dependent angles, D and A are not kept in opposition on the Bloch sphere after their rotation. Because of this, the orthogonal basis power ratios are not similar as displayed in Table 3.23 and Figure 3.25. These results indicate that D and A have both rotated closer towards H on the Bloch sphere after they pass through the optic which is undesirable and can induce biases in the QKD process. This also comes out in H and V in basis measurements where $\langle V| M |V\rangle$ is noticeably less than $\langle H| M |H\rangle$ for the QBER method dependent angles.

Table 3.23: Orthogonal basis power ratios for double mirror examples of QBER calculation method dependent angles

−4° Pan, 0° Tilt	4° Pan, 0° Tilt
$\frac{\langle H\|M\|A\rangle}{\langle V\|M\|A\rangle} = \frac{18.68}{15.45} = 1.2091$	$\frac{\langle H\|M\|A\rangle}{\langle V\|M\|A\rangle} = \frac{17.94}{15.41} = 1.1642$
$\frac{\langle V\|M\|D\rangle}{\langle H\|M\|D\rangle} = \frac{14.49}{17.79} = 0.8145$	$\frac{\langle V\|M\|D\rangle}{\langle H\|M\|D\rangle} = \frac{12.91}{18.34} = 0.7039$

The measured QBER method does not consider the orthogonal basis measurement results, and therefore tends to exhibit lower QBER than the Poln calculated QBER. The Poln QBER calculation is based on the state's fidelity, $\boldsymbol{F_n}$, which can be calculated via Equation 3.13 where $\boldsymbol{\sigma_n}$ is the state's ideal density matrix, and $\boldsymbol{\psi_n}$ is the state's calculated density matrix.

$$F_n = Tr\left[\sigma_n \psi_n \sigma_n\right] \tag{3.13}$$

Equation 3.13 is a simplified version of fidelity presented by Richard Jozsa, shown in Equation 3.14 [71]. The simplification as shown below in Equations 3.14 - 3.18 is based on

$\boldsymbol{\sigma_n}$ being a pure state.

$$F_n = \left(Tr \left[\sqrt{\sqrt{\sigma_n} \psi_n \sqrt{\sigma_n}} \right] \right)^2 \tag{3.14}$$

$$F_n = \left(Tr \left[\sqrt{\sigma_n \psi_n \sigma_n} \right] \right)^2 \tag{3.15}$$

$$F_n = \left(Tr \left[\sqrt{|\sigma_n\rangle \langle\sigma_n| \psi_n |\sigma_n\rangle \langle\sigma_n|} \right] \right)^2 \tag{3.16}$$

The term, $\langle\sigma_n| \psi_n |\sigma_n\rangle$, simplifies to a constant and therefore be taken out of the trace.

$$F_n = \langle\sigma_n| \psi_n |\sigma_n\rangle \left(Tr \left[\sqrt{|\sigma_n\rangle \langle\sigma_n|} \right] \right)^2 \tag{3.17}$$

Because $\boldsymbol{\sigma_n}$ is a pure state, it has trace 1, simplifying Equation 3.14 to Equation 3.18.

$$F_n = \langle\sigma_n| \psi_n |\sigma_n\rangle \tag{3.18}$$

Similarly, Equation 3.13 can also be reduced to Equation 3.18, showing it is identical to 3.14 if $\boldsymbol{\sigma_n}$ is a pure state.

The channel QBER can then be calculated from the fidelity via Equation 3.19 [70].

$$\text{QBER}_{\text{Poln}} = 1 - \sum_{n}^{H,V,D,A} \frac{F_n}{4} \tag{3.19}$$

$\boldsymbol{\psi_n}$ is calculated by the Poln algorithm taking into account all the power measurement data. Because of this, the Poln QBER takes into account various different characteristics of the optic that the measured QBER does not. Therefore, the Poln QBER gives a better overall representation of the quantum channel's deformation. However, it is not necessarily the most accurate description of the induced QBER. As defined earlier in Equation 1.9, QBER is the probability of measuring an erroneous qubit over the probability of measuring a correct or erroneous qubit [22]. This definition coincides directly with how the QBER is calculated from the measurement data.

Based on the premise that the measured QBER is more accurate than the Poln QBER, the previous uncompensated and compensated QBER plots can be reviewed in a new light. The angles that have a significant mismatch between QBER methods also tend to have

particularly higher than expected compensated QBER. This is apparent in all of the four characterized optics.

The single mirror results demonstrate this property well. Its measured QBER is shown to increase as a function of increasing pan angle, which is highly consistent between different tilt angles as shown in Figure 3.23. This makes it apparent that the (0°,0°) and (4°,0°) angles are outliers. Focusing on the compensated QBER in Figure 3.19 we can see that these two measured angles are also significant outliers because of the following two principles. Each measured QBER should have roughly the same corrected QBER for a particular tilt angle as dictated by the tilt dependence as established previously. Furthermore, the 0° tilt angles should have the lowest compensated QBER because the compensation unitary corrects based on the average unitary which should be most similar to the 0° cases. This trend is evident in the compensated QBER for each optic as shown in Figures 3.17 - 3.20. Based on these two principles and the QBER method comparison, the angles given in Table 3.24 have been identified as significant outliers.

Table 3.24: Outlier angles corresponding to high degrees of method dependent QBER

Pentaprism	Periscope Assembly	Single Mirror	Double Mirror
(−4°,−4°), (−4°,4°)	(3°,−3°), (0°,3°), (3°,3°)	(0°,0°), (4°,0°)	(−4°,0°), (4°,0°)

3.6 Simulations

Using a polarization ray tracing tool developed by the Jennewein group, the theoretical QBER and compensation unitaries at various incoming angles were simulated. The matrix formalism used in the script is described in Section 1.2.5 and is based on the three-dimensional ray tracing papers by Chipman et. al. [50, 69].

The rays are simulated with a wavelength of 785 nm and propagate through air before striking the optics. The reflective surfaces are modeled using silver mirrors and the glass used for the pentaprism is N-BK7 float glass based on the materials used in the Automated experiment [63]. The ray tracing diagrams for each simulated configuration are presented in Figure 3.27.

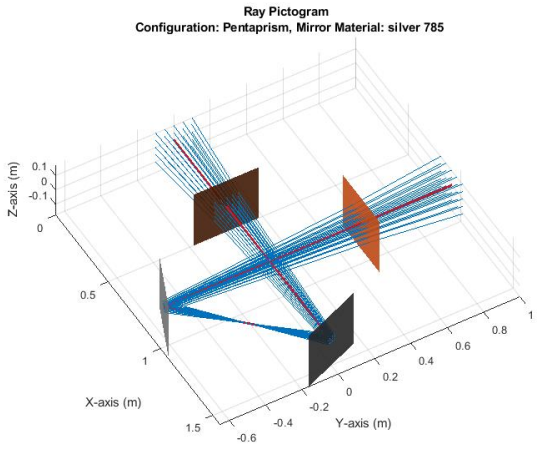

(a) *Pentaprism*

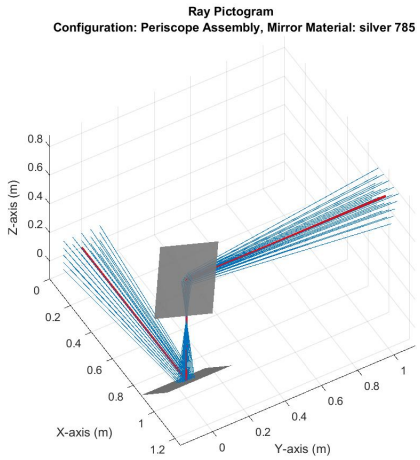

(b) *Periscope Assembly*

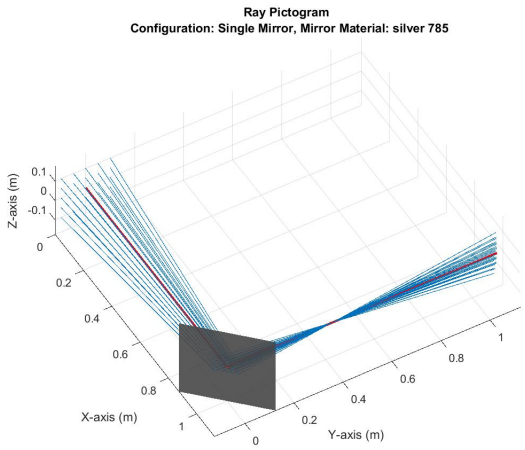

(c) *Single Mirror*

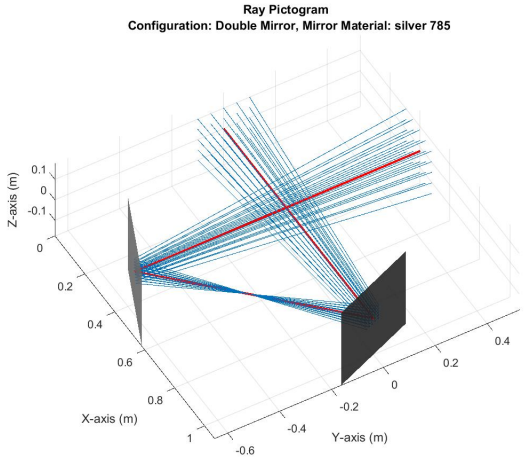

(d) *Double Mirror*

Figure 3.27: *Simulated ray tracing paths for beam steering optics with the central incoming ray starting at the origin*

Incoming light propagates primarily along the positive X direction with the horizontal and vertical polarization components chiefly along the Y axis and Z axis respectively. The primary incoming ray with an pan and tilt angle of 0° and 90° respectively is shown in red in Figure 3.27. It represents the ideal ray path with minimal expected distortion as described in Section 3.2. The other rays, shown in blue, represent the various angular deviations presented in Figures **??**, 3.32, and 3.33. The orange surfaces shown in Figure 3.27a represent where the rays enter and exit the N-BK7 medium of the pentaprism. In Figure 3.27, the gray surfaces depict the silver mirrors.

The plots given in Figure **??**, show the simulated measured power as a fraction of the input power for varying receiver polarizer angles. A simulated anti-diagonal polarized input state is used to construct these sub-figures as an example. The maximum output power for an Anti-diagonally polarized ray should be at 135° if the state is undistorted. Figure **??** shows the simulated output polarization results correlate with the theorized outputs from Section 3.2. Other input states would show analogous results, with an applied phase shift to the sinusoidal pattern.

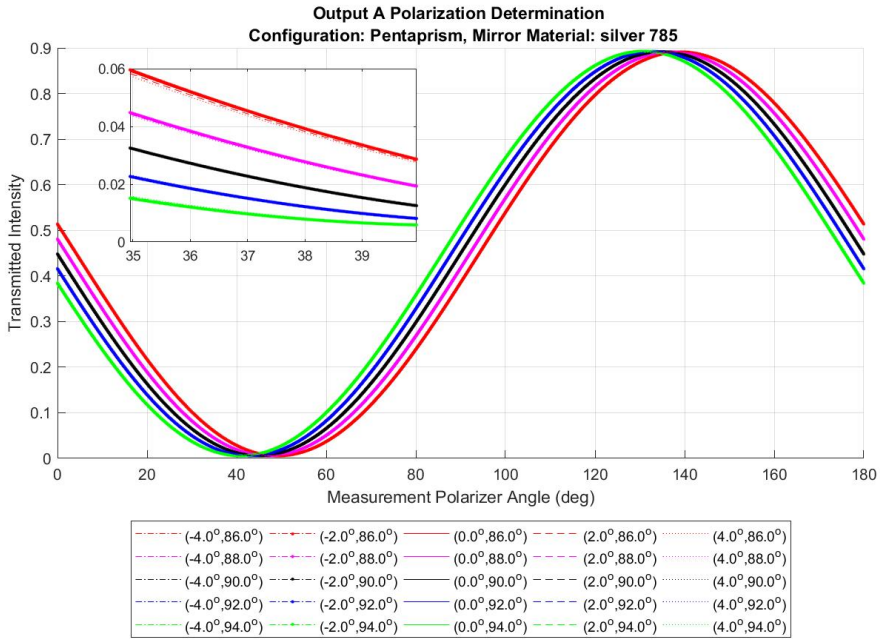

Figure 3.28: *Pentaprism output angular polarization intensities for an input anti-diagonal polarization as an example of angle dependent intensity dispersion*

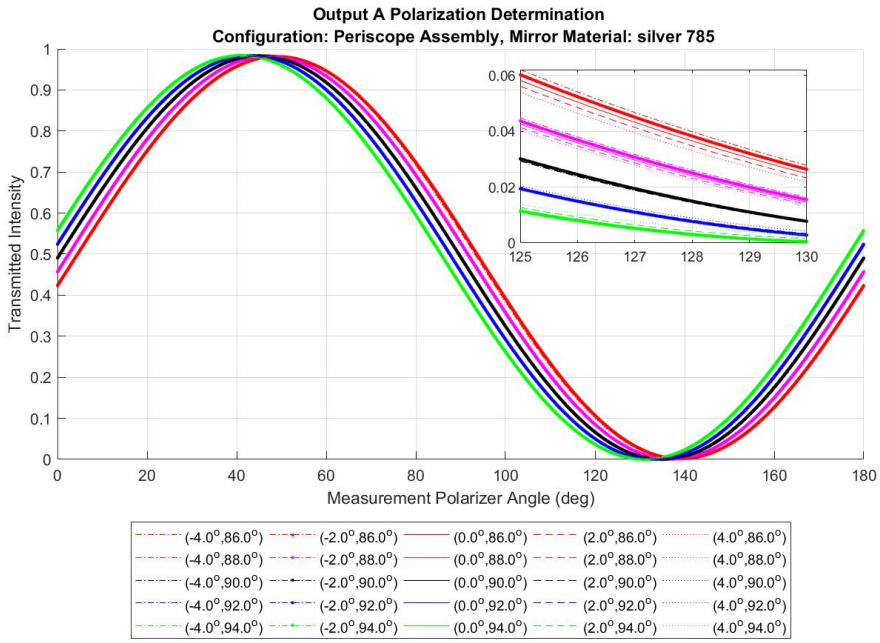

Figure 3.29: *Periscope Assembly output angular polarization intensities for an input anti-diagonal polarization as an example of angle dependent intensity dispersion*

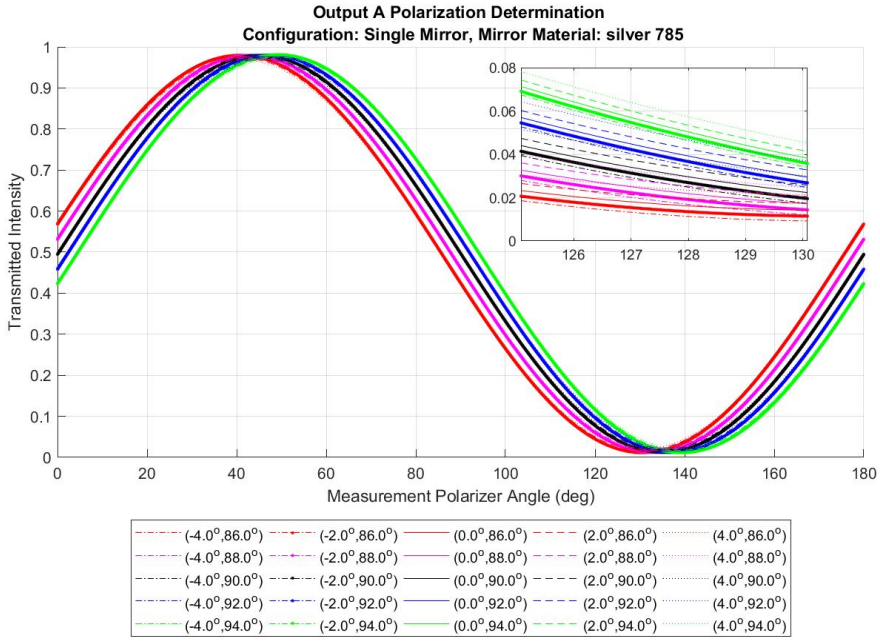

Figure 3.30: *Single Mirror output angular polarization intensities for an input anti-diagonal polarization as an example of angle dependent intensity dispersion*

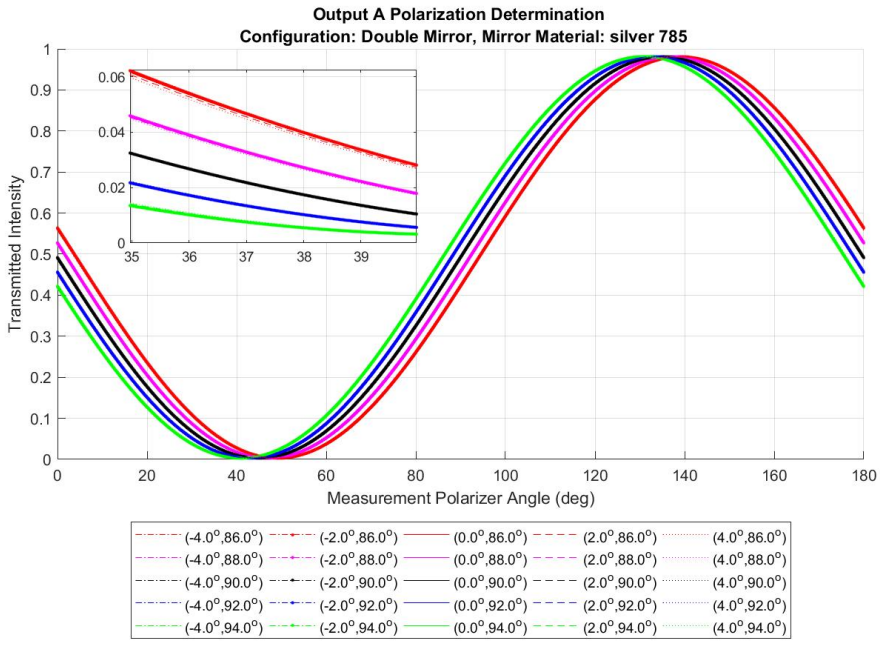

Figure 3.31: *Double Mirror output angular polarization intensities for an input anti-diagonal polarization as an example of angle dependent intensity dispersion*

Figures 3.28 to 3.31 account for 25 various incoming beam angles; however, due to the similarity between each, there is significant overlap in the data. This is as to be expected, and even ideal. The insets for each of the figures are expanded regions of each plot to show overlap or lack there of. Higher degrees in overlap, as seen in the double mirror case in Figure 3.31, indicate that overlapping angles are very similar to each other.

The single mirror plot shows significantly less overlap than the double mirror near the peaks and troughs. Additionally, for the single mirror, the minimum received power does not reach zero any incoming angle, as it does with the other optics. This indicates a reduced purity of the state.

For each optic, there are five sets of overlapping lines. Each line in a set all share the same tilt angle, indicating a strong tilt dependence for all optics simulated. This agrees with what the experimental data from Section 3.5.2 shows.

The resulting QBER for the various incoming beam angles was simulated for each optic configuration, and the results are presented in Figure 3.32

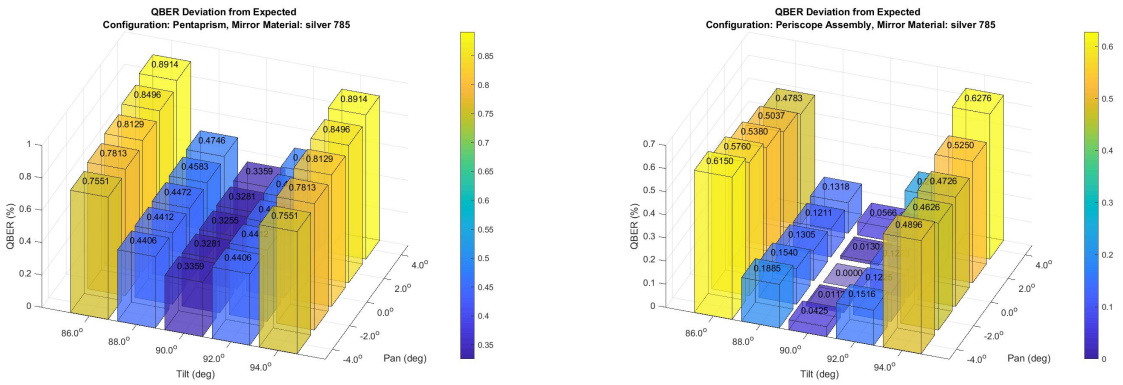

(a) *Pentaprism* **(b)** *Periscope Assembly*

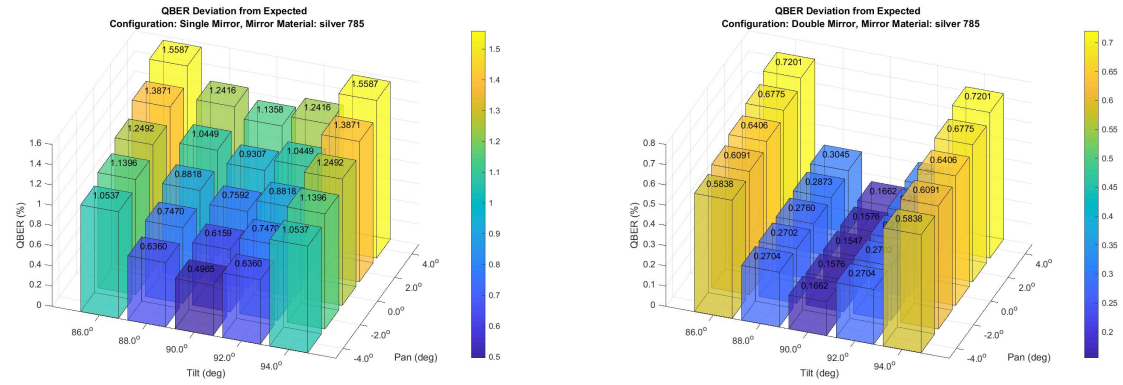

(c) *Single Mirror* **(d)** *Double Mirror*

Figure 3.32: *Simulated QBER*

The simulated single mirror shows some pan and tilt dependence, which matches the experimental results in Figure 3.19. There is a slight deviation in QBER distributions for the simulated and experimental single mirror QBER. This is likely due to an experimental pan and tilt misalignment. The other three simulated optics each show a strong uncompensated tilt dependence which agrees with the results and discussion in Section 3.5.2.

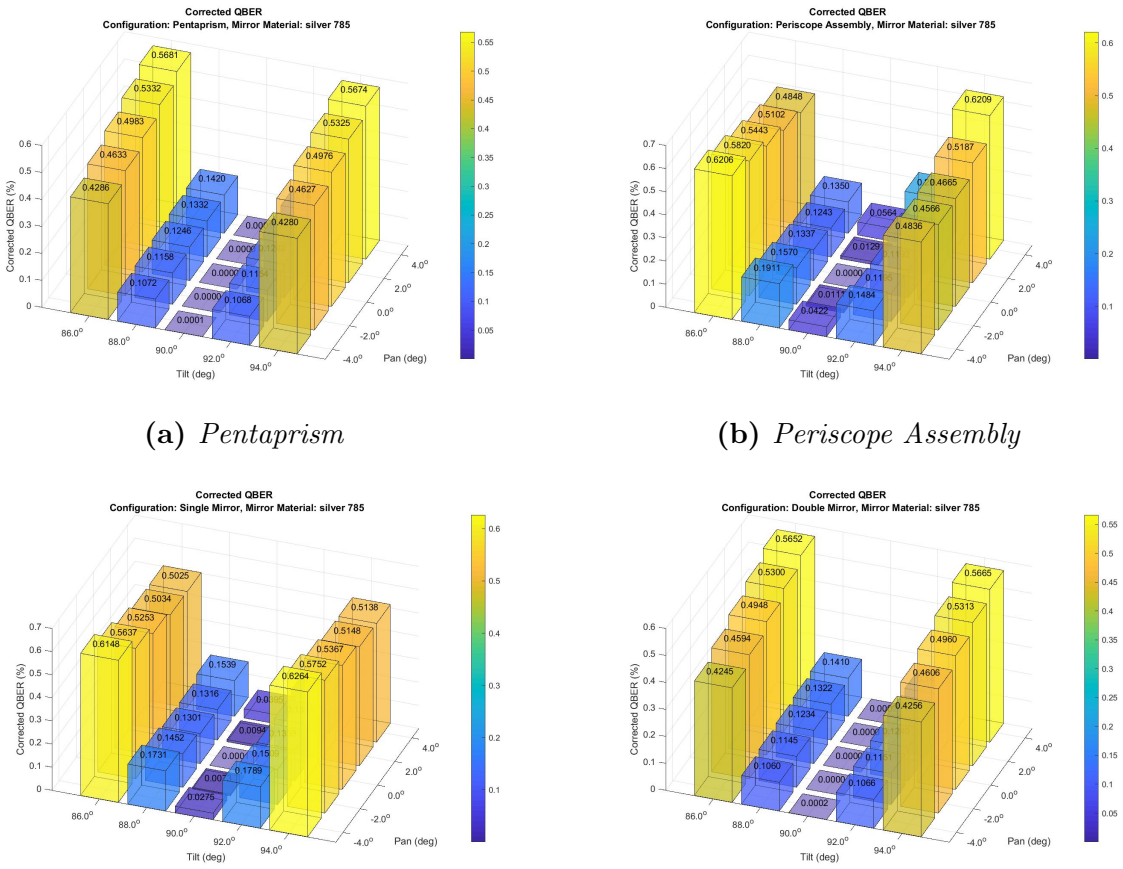

(a) *Pentaprism* **(b)** *Periscope Assembly*

(c) *Single Mirror* **(d)** *Double Mirror*

Figure 3.33: *Simulated QBER compensated with average unitary*

Upon comparing Figure 3.32 and Figure 3.33, we see that the pan trend of the single mirror case is reduced after compensation, and the optic shows a prevalent tilt dependence like the other optics. All of the optics, except the periscope assembly, experience a significant reduction in QBER due to compensation. This is likely because unitary compensation tends to reduce the QBER of the centre ray and the uncompensated QBER of the periscope assembly's 0° pan, 0° tilt ray is extremely close to its minimum. After unitary compensation, the centre angle QBER is almost zero for each optic.

Each of the calculated values in Table 3.25 are based on the average of 9 different incoming angles such that the results are directly comparable to the angles used in Section 3.5.1, given in Table 3.1. The angle range for each optic is stated near the top of the table. Only values corresponding to the same angular range can be compared accurately. This is because values taken over a smaller angular range will be more similar to each other and their will be closer to their ideal. As a result, the periscope assembly was simulated over

two different angular ranges.

Table 3.25: Simulated and experimental average QBER comparison

		Pentaprism	Periscope Assembly	Single Mirror	Double Mirror	Periscope Assembly
Pan and Tilt Angles		$-4°$,$0°$,$4°$	$-3°$,$0°$,$3°$	$-4°$,$0°$,$4°$	$-4°$,$0°$,$4°$	$-4°$,$0°$,$4°$
QBER	Simulated Average	0.6563%	0.2075%	1.1238%	0.4852%	0.3680%
	Experimental Average	0.5095 ± 0.1011%	0.7460 ± 0.0807%	2.9420 ± 0.2166%	0.7883 ± 0.0570%	-
	Simulated Compensated	0.3309%	0.2075%	0.3763%	0.3293%	0.3679%
	Experimental Compensated	0.4647 ± 0.0937%	0.2263 ± 0.0513%	0.3805 ± 0.0574%	0.3177 ± 0.0401%	-

The experimental and simulated values presented in Table 3.25 are seen to be closely correlated to each other. This relation is stronger for the compensated QBER values as the compensation filters out some of the experimental defects and errors. These results indicate that the modeling software is fairly accurate in predicting the amounted of QBER induced on a quantum signal as it passes through various beam steering optics.

It is interesting to note that experimental average QBER is lower than the simulated QBER for the pentaprism. Similarly, the compensated average QBER is less in the experimental case than in the simulated case for the double mirror optics. It is unexpected to have the experimental data set to show a better performance than the simulated data due to natural defects and impurities in the experimental optics. This discrepancy is small and theorized to be a result of experimental state preparation and measurement device inaccuracies and variance.

3.7 Conclusion

The single mirror system is the only sample optic to have its uncompensated QBER above the the 1% QBER threshold, indicating that its performance is sub-par. Post compensation, each of the optics studied are seen to induce similar amounts of distortion, based on the experimental and simulated data. Furthermore, the experimental compensated QBER

for each optic is below half a percent, which is beneath the 1% QBER threshold. Because of these factors, each of the optics are viable in a quantum optic receiver where beam steering is required.

3.7.1 Metric Comparison

From the comparison in Figure 3.34, it can be seen that the single mirror consistently performs poorly over all metrics. As stated previously in Section 3.6, the simulated and experimental compensated QBER agree well with each other for each optic. This indicates that the automated characterization method is fairly accurate after correcting for various experimental errors such as alignment with the unitary compensation.

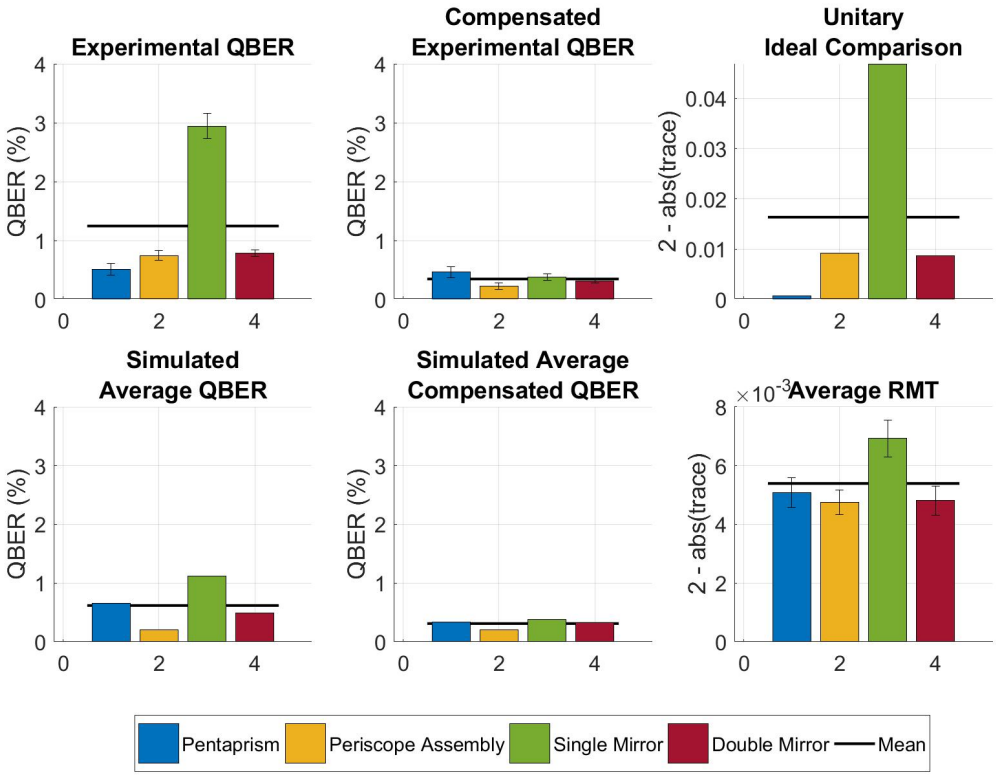

Figure 3.34: *Polarization distortion metric comparison for automated experimental measurements and simulated data*

The compensated QBER and RMT show trends similar to each other with some variance. The RMT effectively measures the differences between the compensation unitaries for each tested incoming angle. If the differences are high, then a single unitary will have

limited effect correcting over all incoming angles. The compensated QBER will therefore be increased as a result.

Figure 3.34 is presented to compare various trends between characterization metrics and not the performance of each optic. In the data it presents, the periscope assembly appears to have a better performance than the other optics. This is because its data was taken over smaller input angle variance as given in Table 3.25 and discussed in Section 3.5.2.5. Based on the data in Table 3.25, the double mirror system gives the best performance based on the compensated QBER over the same set of incoming angles.

3.7.2 Tilt Dependence

The simulated and experimental results indicate a strong relation between the compensated QBER and the incoming tilt angle. Variations of the incoming beam's tilt angle increase the resulting compensated QBER significantly more than pan angle changes do. This trend is evident in Figures 3.17 - 3.20 and 3.33 as well as Tables 3.15 - 3.17.

Chapter 4

Conclusion

Various photon polarization distortion studies have been conducted in this thesis to aid in the design of QKD implementations. In Chapter 2, I presented a simulation model that calculates birefringence due to mechanical stress experienced by an optical window. The model uses the FEM to calculate birefringence in the window due to a pressure differential on either side. It was determined that increases in the incoming beam radius and angle from normal are directly related to increases in birefringence and QBER. Additionally, the effects of the birefringence were seen to cause a polarization bias, effecting the exiting beam's QBER. The induced polarization distortion and bias can be reduced by over an order of magnitude with applied translation and unitary compensation. Furthermore, it was found that the pressurized window has a self compensation effect on the induced polarization distortion. Overall, my studies have shown that it is viable to transmit polarized quantum signals through the WORF window, as it has minimal effect on the QBER post compensation. The compensation mechanism used needs to be angular dependent and can be preformed either at the ground station or receiver. With such compensation, the resulting QBER was simulated to be 0.03% well below the threshold of 1%.

Chapter 3 presented a characterization study of various optical beam steering methods. Two different experiments were completed and a pentaprism, periscope assembly, single mirror reflector, as well as a double mirror reflector were characterized. A polarized ray tracing simulation was utilized as a reference for the experimental data. The improved automated experiment produced results akin to that of the simulation. The data showed similar performances for the various optics, with the double mirror reflector showing a slight advantage over the others. Because all of the sample optics show QBER values below 1% post compensation, they are all viable beam steering options for use in a quantum receiver. The compensation optics can be positioned before or after the beam folding

optics. If compensation is not used, the single mirror system QBER rises above the 1% threshold, and therefore should not be implemented without compensation. Furthermore, an incoming beam tilt angle dependence was noticed throughout all the optics tested in the experiments and in the simulation results.

There are several different avenues of investigation to further the development of these projects. The birefringence simulation could be improved by incorporating various aspects of the beam steering simulation such as polarization dependent refraction. Furthermore, reducing the approximations made, would bring the simulation closer to reality. The simulation assumes the window does not bow due to the pressure which effects the beams relative incoming angle and the stress distribution. Additionally, the incoming beam power distribution is approximated as uniform. Implementing various other beam shapes such as Gaussian, should improve the model's accuracy. To gauge the accuracy of the birefringence model, an experimental test could be developed, similar to the beam steering characterization experiment. The experiment could use a vacuum chamber or pressure chamber to induce stress on an optical window. Furthermore, the simulation could be extended by characterizing the birefringence as a function of wavelength.

To further the beam steering characterization, the angular measurements could be redone for each of the optics over the same incoming angular range. This would be done to more accurately compare the experimental results of each beam steering optic. Additionally, these tests could be redone with automated incoming angle control to increase the accuracy of the set angles. Beam steering optics based on refraction could also be simulated and characterized to study the effects of non-reflection based beam steering optics on polarization. Furthermore, the beam steering optics could be experimentally characterized and simulated at different wavelengths to test for any wavelength dependence.

Letters of copyright permission

Copyright Clearance Center Marketplace™

John Wiley & Sons - Books - License Terms and Conditions

This is a License Agreement between Sebastian Slaman ("You") and John Wiley & Sons - Books ("Publisher") provided by Copyright Clearance Center ("CCC"). The license consists of your order details, the terms and conditions provided by John Wiley & Sons - Books, and the CCC terms and conditions.

All payments must be made in full to CCC.

Order Date	11-May-2020	**Type of Use**	Republish in other published product
Order license ID	1033987-1		
ISBN-13	9780471740377	**Publisher**	Wiley-Interscience
		Portion	Image/photo/illustration

LICENSED CONTENT

Publication Title	Wiley encyclopedia of biomedical engineering	**Country**	United States of America
		Rightsholder	John Wiley & Sons - Books
Author/Editor	Akay, Metin.	**Publication Type**	Book
Date	01/01/2006		
Language	English		

REQUEST DETAILS

Portion Type	Image/photo/illustration	**Distribution**	Canada
Number of images / photos / illustrations	1	**Translation**	Original language of publication
Format (select all that apply)	Print, Electronic	**Copies for the disabled?**	No
		Minor editing privileges?	Yes
Who will republish the content?	Academic institution	**Incidental promotional use?**	No
Duration of Use	Life of current edition	**Currency**	CAD
Lifetime Unit Quantity	Up to 499		
Rights Requested	Main product		

NEW WORK DETAILS

Title	Understanding Polarization Distortions for Real-world Quantum Key Distribution	**Produced by**	University of Waterloo
		Expected publication date	2020-05-15
Author	Sebastian Slaman		

ADDITIONAL DETAILS

Order reference number	N/A	**The requesting person / organization to appear on the license**	Sebastian Slaman

Copyright Clearance Center Marketplace™

American Inst of Aeronautics & Astronautics (AIAA) - License Terms and Conditions

This is a License Agreement between Sebastian Slaman ("You") and American Inst of Aeronautics & Astronautics (AIAA) ("Publisher") provided by Copyright Clearance Center ("CCC"). The license consists of your order details, the terms and conditions provided by American Inst of Aeronautics & Astronautics (AIAA), and the CCC terms and conditions.

All payments must be made in full to CCC.

Order Date	08-May-2020	**Publisher**	AIAA
Order license ID	1033479-1	**Portion**	Image/photo/illustration
Type of Use	Republish in other published product		

LICENSED CONTENT

Publication Title	36th AIAA Aerospace Sciences Meeting and Exhibit	**Country**	United States of America
		Rightsholder	American Inst of Aeronautics & Astronautics (AIAA)
Date	01/01/1998		
Language	English	**Publication Type**	Book

REQUEST DETAILS

Portion Type	Image/photo/illustration	**Distribution**	Canada
Number of images / photos / illustrations	1	**Translation**	Original language of publication
Format (select all that apply)	Electronic	**Copies for the disabled?**	No
		Minor editing privileges?	No
Who will republish the content?	Academic institution	**Incidental promotional use?**	No
Duration of Use	Life of current edition	**Currency**	CAD
Lifetime Unit Quantity	Up to 499		
Rights Requested	Main product		

NEW WORK DETAILS

Title	Understanding Polarization Distortions for Real-world Quantum Key Distribution	**Produced by**	University of Waterloo
		Expected publication date	2020-05-15
Author	Sebastian Slaman		

ADDITIONAL DETAILS

Order reference number	N/A	**The requesting person / organization to appear on the license**	Sebastian Slaman

American Physical Society
Reuse and Permissions License

11-May-2020

This license agreement between the American Physical Society ("APS") and Sebastian Slaman ("You") consists of your license details and the terms and conditions provided by the American Physical Society and SciPris.

Licensed Content Information

License Number:	**RNP/20/MAY/025709**
License date:	11-May-2020
DOI:	10.1103/PhysRevA.92.052339
Title:	Experimental quantum key distribution with simulated ground-to-satellite photon losses and processing limitations
Author:	Jean-Philippe Bourgoin et al.
Publication:	Physical Review A
Publisher:	American Physical Society
Cost:	USD $ 0.00

Request Details

Does your reuse require significant modifications: No

Specify intended distribution locations:	Canada
Reuse Category:	Reuse in a thesis/dissertation
Requestor Type:	Student
Items for Reuse:	Figures/Tables
Number of Figure/Tables:	1
Figure/Tables Details:	High-loss QKD receiver
Format for Reuse:	Electronic

Information about New Publication:

University/Publisher:	University of Waterloo
Title of dissertation/thesis:	Understanding Polarization Distortions for Real-world Quantum Key Distribution
Author(s):	Sebastian Slaman
Expected completion date:	May. 2020

License Requestor Information

Name:	Sebastian Slaman
Affiliation:	Individual
Email Id:	sebslaman@gmail.com
Country:	Canada

References

[1] Albert Einstein, Boris Podolsky, and Nathan Rosen. Can quantum-mechanical description of physical reality be considered complete? *Physical review*, 47(10):777, 1935.

[2] John S Bell. On the einstein podolsky rosen paradox. *Physics Physique Fizika*, 1(3):195, 1964.

[3] Werner Heisenberg. Über den anschaulichen inhalt der quantentheoretischen kinematik und mechanik. In *Original Scientific Papers Wissenschaftliche Originalarbeiten*, pages 478–504. Springer, 1985.

[4] Charles H Bennett, Gilles Brassard, Claude Crépeau, Richard Jozsa, Asher Peres, and William K Wootters. Teleporting an unknown quantum state via dual classical and einstein-podolsky-rosen channels. *Physical review letters*, 70(13):1895, 1993.

[5] Stefano Pirandola, Jens Eisert, Christian Weedbrook, Akira Furusawa, and Samuel L Braunstein. Advances in quantum teleportation. *Nature photonics*, 9(10):641, 2015.

[6] Michael A Nielsen and Isaac Chuang. Quantum computation and quantum information, 2002.

[7] C. H. Bennett and G. Brassard. Quantum cryptography: Public key distribution and coin tossing. In *Proceedings of the IEEE International Conference on Computers, Systems, and Signal Processing*, pages 175–179, Bangalore, India, December 1984.

[8] Valerio Scarani, Helle Bechmann-Pasquinucci, Nicolas J Cerf, Miloslav Dušek, Norbert Lütkenhaus, and Momtchil Peev. The security of practical quantum key distribution. *Reviews of modern physics*, 81(3):1301, 2009.

[9] Ramy Tannous. Polarization entangled photon sources for free-space quantum key distribution. Master's thesis, University of Waterloo, 2018.

[10] Artur K Ekert. Quantum cryptography based on bells theorem. *Physical review letters*, 67(6):661, 1991.

[11] C. H. Bennett, G. Brassard, and N. D. Mermin. Quantum cryptography without bell's theorem. *Phys. Rev. Lett.*, 68:557, 1992.

[12] James L Park. The concept of transition in quantum mechanics. *Foundations of Physics*, 1(1):23–33, 1970.

[13] William K Wootters and Wojciech H Zurek. A single quantum cannot be cloned. *Nature*, 299(5886):802, 1982.

[14] Felix Bloch. Nuclear induction. *Physical review*, 70(7-8):460, 1946.

[15] Kyo Inoue and Yuuki Iwai. Differential-quadrature-phase-shift quantum key distribution. *Physical Review A*, 79(2):022319, 2009.

[16] Matthieu Bloch, Steven W McLaughlin, Jean-Marc Merolla, and Frédéric Patois. Frequency-coded quantum key distribution. *Optics letters*, 32(3):301–303, 2007.

[17] Robert Thomas Thew, Sébastien Tanzilli, Wolfgang Tittel, Hugo Zbinden, and Nicolas Gisin. Experimental investigation of the robustness of partially entangled qubits over 11 km. *Physical Review A*, 66(6):062304, 2002.

[18] Jürgen Brendel, Nicolas Gisin, Wolfgang Tittel, and Hugo Zbinden. Pulsed energy-time entangled twin-photon source for quantum communication. *Physical Review Letters*, 82(12):2594, 1999.

[19] Gilbert S Vernam. Cipher printing telegraph systems: For secret wire and radio telegraphic communications. *Journal of the AIEE*, 45(2):109–115, 1926.

[20] Claude E Shannon. Communication theory of secrecy systems. *Bell system technical journal*, 28(4):656–715, 1949.

[21] G. Gilbert and M. Hamrick. Practical quantum cryptography: A comprehensive analysis (part one). Technical Report MTR00W0000052, The MITRE Corporation, 2000. arXiv:quant-ph/0009027.

[22] Nicolas Gisin, Grégoire Ribordy, Wolfgang Tittel, and Hugo Zbinden. Quantum cryptography. *Reviews of modern physics*, 74(1):145, 2002.

[23] Norbert Lütkenhaus. Estimates for practical quantum cryptography. *Physical Review A*, 59(5):3301, 1999.

[24] Jean-Philippe Bourgoin, Nikolay Gigov, Brendon L Higgins, Zhizhong Yan, Evan Meyer-Scott, Amir K Khandani, Norbert Lütkenhaus, and Thomas Jennewein. Experimental quantum key distribution with simulated ground-to-satellite photon losses and processing limitations. *Physical Review A*, 92(5):052339, 2015.

[25] Charles H Bennett and Gilles Brassard. Experimental quantum cryptography: the dawn of a new era for quantum cryptography: the experimental prototype is working. *ACM Sigact News*, 20(4):78–80, 1989.

[26] Charles H Bennett, François Bessette, Gilles Brassard, Louis Salvail, and John Smolin. Experimental quantum cryptography. *Journal of cryptology*, 5(1):3–28, 1992.

[27] R. Ursin, F. Tiefenbacher, T. Schmitt-Manderbacha, H. Weier, T. Scheidl, M. Lindenthal, B. Blauensteiner, T. Jennewein, J. Perdigues, P. Trojek, B. Oemer, M. Fuerst, M. Meyenburg, J. Rarity, Z. Sodnik, C. Barbieri, H. Weinfurter, and A. Zeilinger. Free-space distribution of entanglement and single photons over 144 km. *Nature Physics*, 3:481–486, 2007.

[28] LC Comandar, B Fröhlich, M Lucamarini, KA Patel, AW Sharpe, JF Dynes, ZL Yuan, RV Penty, and AJ Shields. Room temperature single-photon detectors for high bit rate quantum key distribution. *Applied Physics Letters*, 104(2):021101, 2014.

[29] Hua-Lei Yin, Teng-Yun Chen, Zong-Wen Yu, Hui Liu, Li-Xing You, Yi-Heng Zhou, Si-Jing Chen, Yingqiu Mao, Ming-Qi Huang, Wei-Jun Zhang, et al. Measurement-device-independent quantum key distribution over a 404 km optical fiber. *Physical review letters*, 117(19):190501, 2016.

[30] Yichen Zhang, Zhengyu Li, Ziyang Chen, Christian Weedbrook, Yijia Zhao, Xiangyu Wang, Yundi Huang, Chunchao Xu, Xiaoxiong Zhang, Zhenya Wang, et al. Continuous-variable qkd over 50 km commercial fiber. *Quantum Science and Technology*, 4(3):035006, 2019.

[31] Gilles Brassard, Norbert Lütkenhaus, Tal Mor, and Barry C Sanders. Limitations on practical quantum cryptography. *Physical Review Letters*, 85(6):1330, 2000.

[32] L-M Duan, MD Lukin, J Ignacio Cirac, and Peter Zoller. Long-distance quantum communication with atomic ensembles and linear optics. *Nature*, 414(6862):413, 2001.

[33] Nicolas Sangouard, Christoph Simon, Hugues De Riedmatten, and Nicolas Gisin. Quantum repeaters based on atomic ensembles and linear optics. *Reviews of Modern Physics*, 83(1):33, 2011.

[34] T Jennewein, JP Bourgoin, B Higgins, C Holloway, E Meyer-Scott, C Erven, B Heim, Z Yan, H Hübel, G Weihs, et al. Qeyssat: a mission proposal for a quantum receiver in space. In *Advances in Photonics of Quantum Computing, Memory, and Communication VII*, volume 8997, page 89970A. International Society for Optics and Photonics, 2014.

[35] Paolo Villoresi, Thomas Jennewein, Fabrizio Tamburini, Markus Aspelmeyer, Cristian Bonato, Rupert Ursin, Claudio Pernechele, Vincenza Luceri, Giuseppe Bianco, Anton Zeilinger, et al. Experimental verification of the feasibility of a quantum channel between space and earth. *New Journal of Physics*, 10(3):033038, 2008.

[36] T Jennewein, C Grant, E Choi, C Pugh, C Holloway, JP Bourgoin, H Hakima, B Higgins, and R Zee. The nanoqey mission ground to space quantum key and entanglement distribution using a nanosatellite. In *Emerging technologies in security and defence II; and quantum-physics-based information security III*, volume 9254, page 925402. International Society for Optics and Photonics, 2014.

[37] Sheng-Kai Liao, Wen-Qi Cai, Wei-Yue Liu, Liang Zhang, Yang Li, Ji-Gang Ren, Juan Yin, Qi Shen, Yuan Cao, Zheng-Ping Li, et al. Satellite-to-ground quantum key distribution. *Nature*, 549(7670):43, 2017.

[38] Sheng-Kai Liao, Wen-Qi Cai, Johannes Handsteiner, Bo Liu, Juan Yin, Liang Zhang, Dominik Rauch, Matthias Fink, Ji-Gang Ren, Wei-Yue Liu, et al. Satellite-relayed intercontinental quantum network. *Physical review letters*, 120(3):030501, 2018.

[39] JP Bourgoin, E Meyer-Scott, Brendon L Higgins, B Helou, Chris Erven, Hannes Huebel, B Kumar, D Hudson, Ian D'Souza, Ralph Girard, et al. A comprehensive design and performance analysis of low earth orbit satellite quantum communication. *New Journal of Physics*, 15(2):023006, 2013.

[40] Christopher Pugh. Free space quantum key distribution to moving platforms. 2017.

[41] Michael A Krainak, W Yu Anthony, Guangning Yang, Steven X Li, and Xiaoli Sun. Photon-counting detectors for space-based laser receivers. In *Quantum Sensing and Nanophotonic Devices VII*, volume 7608, page 760827. International Society for Optics and Photonics, 2010.

[42] Brendon Higgins, Jean-Philippe Bourgoin, Nikolay Gigov, Evan Meyer-Scott, Zhizhong Yan, and Thomas Jennewein. Detailed performance analysis of the proposed qeyssat quantum receiver satellite. In *2012 Conference on Lasers and Electro-Optics (CLEO)*, pages 1–2. IEEE, 2012.

[43] Christopher J Pugh, Sarah Kaiser, Jean-Philippe Bourgoin, Jeongwan Jin, Nigar Sultana, Sascha Agne, Elena Anisimova, Vadim Makarov, Eric Choi, Brendon L Higgins, et al. Airborne demonstration of a quantum key distribution receiver payload. *Quantum Science and Technology*, 2(2):024009, 2017.

[44] Jean-Philippe Bourgoin, Brendon L Higgins, Nikolay Gigov, Catherine Holloway, Christopher J Pugh, Sarah Kaiser, Miles Cranmer, and Thomas Jennewein. Free-space quantum key distribution to a moving receiver. *Optics express*, 23(26):33437–33447, 2015.

[45] B. E. A. Saleh and M. C. Teich. *Fundamentals of Photonics*. Wiley-Interscience, second edition, 2007.

[46] Russell A Chipman. Polarization analysis of optical systems. *Optical engineering*, 28(2):280290, 1989.

[47] Eugene Hecht. *Optics*. Addison-Wesley, fourth edition, 2002.

[48] R Clark Jones. A new calculus for the treatment of optical systemsi. description and discussion of the calculus. *Josa*, 31(7):488–493, 1941.

[49] José J Gil and Eusebio Bernabeu. Obtainment of the polarizing and retardation parameters of a non-depolarizing optical system from the polar decomposition of its mueller matrix. *Optik*, 76(2):67–71, 1987.

[50] Garam Yun, Karlton Crabtree, and Russell A Chipman. Three-dimensional polarization ray-tracing calculus i: definition and diattenuation. *Applied optics*, 50(18):2855–2865, 2011.

[51] Haiyang Zhang, Yi Li, Changxiang Yan, and Junqiang Zhang. Three-dimensional polarization ray tracing calculus for partially polarized light. *Optics express*, 25(22):26973–26986, 2017.

[52] Garam Yun, Stephen C McClain, and Russell A Chipman. Three-dimensional polarization ray-tracing calculus ii: retardance. *Applied optics*, 50(18):2866–2874, 2011.

[53] Serdar Artan. *Bulk Modulus*. Wiley Online Library, 04 2006.

[54] Keith B Doyle, Victor L Genberg, and Gregory J Michels. Numerical methods to compute optical errors due to stress birefringence. In *Optical Design and Analysis Software II*, volume 4769, pages 34–42. International Society for Optics and Photonics, 2002.

[55] Karen Scott, Dave Warren, Dean Eppler, Dave Amsbury, and Mark Pestana. Development of the international space station high optical quality window. In *36th AIAA Aerospace Sciences Meeting and Exhibit*, page 391, 1998.

[56] Sebastian Slaman and Thomas Jennewein. Modelling polarisation distortion of optical quantum signals through a pressurized window. *Physics in Canada*, 74(3):129–130, 2018.

[57] Rupert Ursin, Thomas Jennewein, Johannes Kofler, Josep M Perdigues, Luigi Cacciapuoti, Clovis J de Matos, Markus Aspelmeyer, Alejandra Valencia, Thomas Scheidl, Antonio Acin, et al. Space-quest, experiments with quantum entanglement in space. *Europhysics News*, 40(3):26–29, 2009.

[58] David Edward Bruschi, Timothy C Ralph, Ivette Fuentes, Thomas Jennewein, and Mohsen Razavi. Spacetime effects on satellite-based quantum communications. *Physical Review D*, 90(4):045041, 2014.

[59] Siddarth Koduru Joshi, Jacques Pienaar, Timothy C Ralph, Luigi Cacciapuoti, Will McCutcheon, John Rarity, Dirk Giggenbach, Jin Gyu Lim, Vadim Makarov, Ivette Fuentes, et al. Space quest mission proposal: experimentally testing decoherence due to gravity. *New journal of physics*, 20(6):063016, 2018.

[60] Rupert Ursin, Thomas Jennewein, Felix Tiefenbacher, and Anton Zeilinger. Applications of quantum entanglement on a iss-spaceplatform. In *International Conference on Space OpticsICSO 2006*, volume 10567, page 1056727. International Society for Optics and Photonics, 2017.

[61] Sang B. Gubbini E Neuzner, A. Worf window optical performance: Assessment and proposed way forward. Technical Report MTR00W0000052, OHB, 2017.

[62] William S Rodney and Robert J Spindler. Index of refraction of fused quartz glass for ultraviolet, visible, and infrared wavelengths. *JOSA*, 44(9):677–679, 1954.

[63] Mikhail N. Polyanskiy. Refractive index database. https://refractiveindex.info. Accessed on 2019-09-26.

[64] Keith Doyle, Jeffrey Hoffman, Victor Genberg, and Gregory Michels. Stress birefringence modeling for lens design and photonics. In *International Optical Design Conference*, page IWC1. Optical Society of America, 2002.

[65] Olivier Lubin and Olivier Heuzé. Modelling of stress-induced birefringence in vacuum barrier lenses. *Pure and Applied Optics: Journal of the European Optical Society Part A*, 7(4):699, 1998.

[66] John H Burnett. Stress-optical coefficients of 157 nm materials. Technical report, 2001.

[67] IH Malitson. Interspecimen comparison of the refractive index of fused silica. *Josa*, 55(10):1205–1209, 1965.

[68] M Sparks and M Cottis. Pressure-induced optical distortion in laser windows. *Journal of Applied Physics*, 44(2):787–794, 1973.

[69] Wai Sze Tiffany Lam and Russell Chipman. Balancing polarization aberrations in crossed fold mirrors. *Applied optics*, 54(11):3236–3245, 2015.

[70] Brendon L Higgins, Jean-Philippe Bourgoin, and Thomas Jennewein. Practical polarization-frame alignment for quantum key distribution with single-photon-level resources. *arXiv preprint arXiv:1810.04112*, 2018.

[71] Richard Jozsa. Fidelity for mixed quantum states. *Journal of modern optics*, 41(12):2315–2323, 1994.

Beam Steering Data

.1 Pentaprism Reference Correction

During the manual optics characterization tests, a polarization discrepancy was noticed between the pentaprism's transmission and reflection. For the pentaprism pan measurements, the transmission path was used as a reference as shown in Figure 1. Therefore, the polarization bias between the reflected and transmitted paths caused a bias in the measurement data. This polarization bias is not inherent to the pentaprism design, but is a flaw in the physical construction of the pentaprism used.

As a result of the bias, the data needed to be corrected or retaken. This discrepancy was corrected for by measuring the pentaprism's transmitted and reflected power along with a reference for the 6 input states to measure the bias. With the bias known, the previously biased references were adjusted accordingly. The corrected pentaprism pan data is presented in Section 3.4.

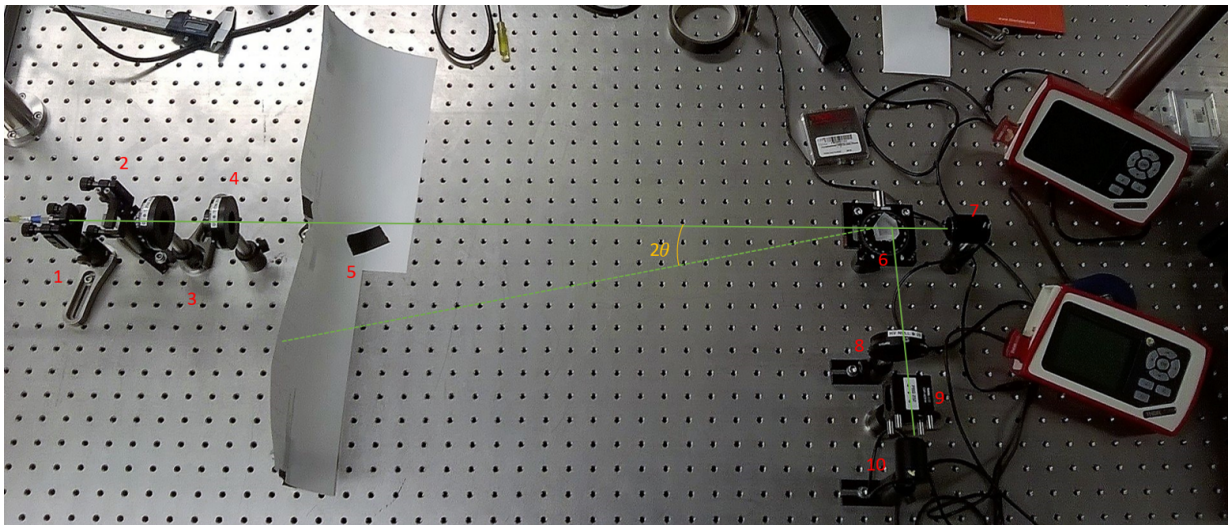

Figure 1: *Pentaprism pan characterization optical setup with reference measuring transmission path*

For the pentaprism pan configuration, the collimated laser light (1) passed through a PBS (2). The horizontally polarized light then passed through a HWP (3) followed by a QWP (4) for polarization rotation and state selection. The beam was then partly transmitted and partly reflected by the pentaprism (6). The transmitted portion was measured by a power meter (7) for reference and the reflected beam continued toward the polarization measurement HWP (8). It then passed through a PBS (9) before reaching the power meter (10).

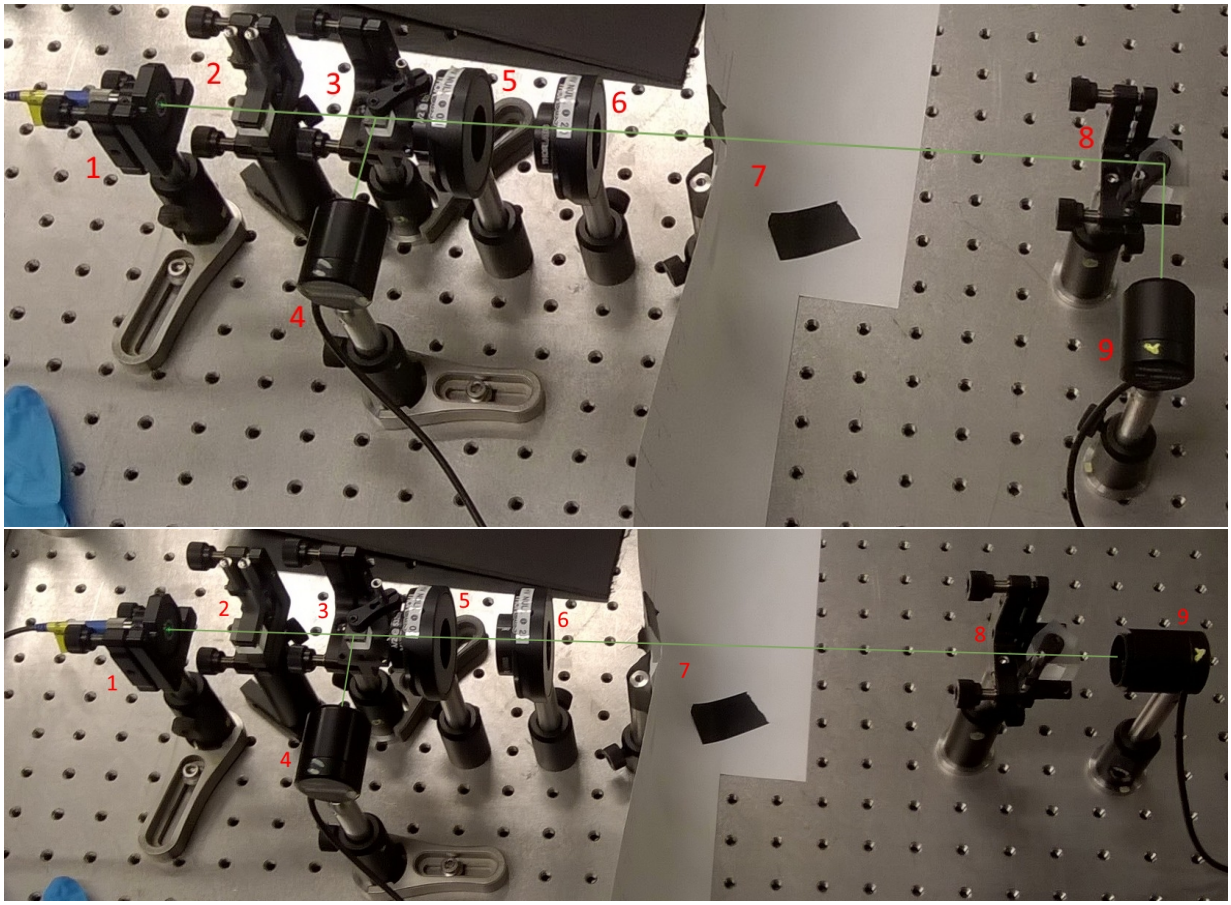

Figure 2: *Pentaprism reference polarization bias characterization setup*

The pentaprism transmission bias characterization was done by taking reflection and transmission measurements for each of the 6 input polarizations. Proper reference measurements we taken after the PBS along side the characterization data. The set up used was very similar to the one described in Section 3.4 without the polarization selection measurement optics. Power measurements were taken directly after the pentaprism for the transmitted and reflected paths. The measured data is given below in Table 1. The relative intensities of the measurement data scaled proportionally to the reference are provided in

Table 2.

Table 1: Pentaprism reference correction measured powers (μW)

		Input					
		H	V	D	A	R	L
Transmit	Power	24.3	21.8	23.9	25.03	23.2	25.5
	Reference	54.77	54.04	56.13	59.07	54.22	60.73
Reflect	Power	16.2	19.8	16.8	17.1	19.1	18.3
	Reference	55.79	59.96	53.98	54.14	60.64	59.48

From the relative intensities, it was made apparent that there is a polarization bias in the rectilinear basis. The pentaprism tends to transmit more H than V, whist reflecting more V than H. The diagonal and circular basis do not show strong affinities to particular polarization states.

Table 2: Pentaprism reference correction relative intensities. Power is given as a percentage of the reference

	Input					
	H	V	D	A	R	L
Transmit	44.37	40.34	42.58	42.37	42.79	41.99
Reflect	29.04	33.02	31.12	31.58	31.50	30.77

The original pan measurements were scaled by dividing the reflected power by the transmitted power. To counter this improper reference correction, the scaled measurements were multiplied by the characterized transmitted power over the reference measurement. This results in the transmitted portions canceling each other out as demonstrated by Equation 1. The correction is performed for the pentaprism pan dataset using the correction factors appropriate to each input polarization.

$$\text{Intensity}_{\text{corrected}} = \frac{\text{Reflected}}{\text{transmitted}} \cdot \frac{\text{Transmitted}_{\text{correction}}}{\text{Reference}_{\text{correction}}} \tag{1}$$

.2 Beam Steering Manual Method Data

The manual method beam steering data is presented in the tables below for reference.

Table 3: Pentaprism pan measured powers (μW)

				Input					
				H	V	D	A	R	L
Measured	0°	H	Reflected	17.4	0.23	5.93	8.57	6.29	8.15
			Transmitted	101.7	82.3	80.8	85.9	80	78.4
		V	Reflected	0.223	19.3	9.53	8.67	7.15	10.26
			Transmitted	103.6	91.5	81.9	89.3	79	88.7
		D	Reflected	8.77	8.95	15.2	0.317	5.75	11.28
			Transmitted	90.4	92.9	81.4	87.5	89.4	89.7
		A	Reflected	6.5	10.9	0.337	17.4	8.3	8.67
			Transmitted	93.8	83.7	79.5	89	81.2	88.8
	7°	H	Reflected	13.19	0.24	5.59	6.94	5.87	6.95
			Transmitted	87.3	77.8	83.2	77.4	79.6	77.9
		V	Reflected	0.208	16.7	9.35	6.99	7.53	8.86
			Transmitted	92.5	93.2	85.3	77.2	88	82.2
		D	Reflected	7.9	6.46	13.31	0.338	4.53	9.5
			Transmitted	88.9	76.6	78.7	87.7	80.9	80.7
		A	Reflected	5.91	9.83	0.142	14	7.89	6.59
			Transmitted	98.3	78.4	78.1	77.8	78	78.2
	−7°	H	Reflected	19.4	0.353	7.81	10.98	8.01	13.67
			Transmitted	100.1	92.9	101.3	104.7	97	107.1
		V	Reflected	0.145	23.5	11.79	12.16	10.52	12.05
			Transmitted	114.5	97.2	102	113.6	96.3	95.8
		D	Reflected	10.98	10.05	22.6	0.238	8.74	13.01
			Transmitted	103.2	94.1	115.6	107.8	99.8	97.8
		A	Reflected	8.71	14.6	0.32	21.4	10.96	13.32
			Transmitted	108.4	104.9	105	95.8	108.9	105.5

Table 4: Pentaprism tilt measured powers (μW)

				Input					
				H	V	D	A	R	L
Measured	0°	H	Power	11.51	0.11	5.19	6.12	6.72	5.57
			Reference	130.6	128.4	132.9	124.5	132.1	132.1
		V	Power	0.2	11.77	7.17	6.36	7.54	6.09
			Reference	127.3	119.1	126.9	133.6	127.2	131.9
		D	Power	6.22	5.64	11.57	0.07	5.32	6.73
			Reference	129.3	126.6	122.4	129.4	119	126.6
		A	Power	5.18	6.45	0.32	12.04	6.69	4.46
			Reference	126.8	122.4	119.1	126.6	133.1	123.3
	−4°	H	Power	9.58	0.12	4.78	4.22	4.63	4.56
			Reference	132.3	131.8	121.3	127	131	119.4
		V	Power	0.08	10.19	4.61	6.3	5.23	5.42
			Reference	128.9	122.1	126	127.8	128.6	125.2
		D	Power	4.21	5.63	10.09	0.29	3.9	6.29
			Reference	125.7	125.5	131.7	125.4	132	128.8
		A	Power	4.95	4.65	0.09	10.06	5.68	4.2
			Reference	119.9	121.7	119.9	128.1	126.8	122.1
	4°	H	Power	5.73	0.21	1.96	3.53	3.17	2.28
			Reference	130.3	122.9	129.3	119.4	121.8	121
		V	Power	0.23	6.3	4.36	2.24	3.3	3.11
			Reference	132.3	124.8	124.3	122.7	132.7	121
		D	Power	4.1	2.17	6.19	0.15	2.71	3.5
			Reference	130.6	129.5	133.1	121.5	133.5	133.1
		A	Power	1.97	4.14	0.38	5.98	3.76	2.45
			Reference	122.8	119.7	132.3	126.6	123.9	126.6

Table 5: Periscope assembly pan measured powers (μW)

				Input					
				H	V	D	A	R	L
Measured	0°	H	Power	0.23	17.8	10.38	7.78	8.43	9.17
			Reference	54.01	57.86	55.92	54.14	55.72	55.14
		V	Power	15.7	0.21	7.95	10.61	9.54	8.68
			Reference	53.88	60.53	59.47	60.68	58.73	60.52
		D	Power	7.06	9.94	0.21	19	10.71	8.15
			Reference	59.84	55.36	56.56	59.25	60.52	60.39
		A	Power	10.05	7.49	18.8	0.21	7.17	10.88
			Reference	56.27	59.25	60.65	60.43	54.02	59.86
	2°	H	Power	0.175	17.7	10.88	7.65	8.59	8.29
			Reference	56.87	63.24	62.55	59.86	57.1	58.17
		V	Power	16.1	0.3	7.04	9.48	8.58	8.2
			Reference	57.56	61.93	63.05	56.53	60.88	59.03
		D	Power	7.08	10.71	0.32	17	9.22	7.26
			Reference	62.68	62.53	63.3	62.97	55.95	60.76
		A	Power	8.85	8.13	16	0.17	7.63	9.27
			Reference	56.2	63.26	57.11	56.01	63.09	57.09
	−2°	H	Power	0.35	35.2	20.5	15.2	16	16.5
			Reference	129.3	128.8	128.8	118.6	116.1	116.8
		V	Power	32.6	0.18	15.5	18.2	17.5	14.5
			Reference	117.5	127.8	121.5	122.5	115.9	116.8
		D	Power	14.8	18	0.487	32.9	19.8	12.65
			Reference	122.7	116.4	129.2	119.1	115.9	118.6
		A	Power	18.2	15.5	32	0.27	14.4	19.5
			Reference	129.2	116.7	117	118.4	125.1	120.8

Table 6: Periscope assembly tilt measured powers (μW)

				Input					
				H	V	D	A	R	L
Measured	0°	H	Power	0.293	36.3	21.9	19.6	19.8	22.2
			Reference	112	119.1	119.9	131.2	130.5	120.8
		V	Power	35.8	0.506	18.4	23.9	20.4	22.7
			Reference	132.6	125	127.8	123.7	120	133.3
		D	Power	14.4	22.7	0.421	44.2	24	19.1
			Reference	130.8	132	118.8	130.5	129.4	120.7
		A	Power	20.7	14.6	39.5	0.574	15.7	25.2
			Reference	128.1	119.6	119	131.2	120.6	122.9
	−4°	H	Power	0.2	38.7	21.2	21.7	21.1	20.5
			Reference	131.7	118.6	124.1	132.8	130.8	130.2
		V	Power	41.5	0.13	21.7	20.8	20.7	17.4
			Reference	126.9	123.5	129.3	133.1	119.6	120.6
		D	Power	18.8	21.7	0.232	38.7	22.7	16.3
			Reference	123.6	122.7	122.4	119	121.8	121.2
		A	Power	19.4	20.2	42.8	0.22	17.3	21.6
			Reference	121.3	121.2	131.2	128.5	124.1	122.7
	4°	H	Power	1.25	35.6	23.5	12.9	17	19.9
			Reference	133.1	127.9	122	119.8	120	123.7
		V	Power	37.5	1.13	12.34	23.3	21.8	17.5
			Reference	133.3	119.8	122.2	129.3	132.6	127.4
		D	Power	11.78	23.8	0.971	34.7	23.2	14.9
			Reference	119.5	124.2	120.8	123.2	125.1	128.1
		A	Power	24.2	12.31	33.9	0.913	15.5	22.3
			Reference	125.1	133.5	120.8	133.3	130.8	120.9

.2.1 Polarization Contrasts

The polarization contrasts are given in the tables below for reference. They are calculated from the values given in Section 3.4.2.1. The polarization contrasts were calculated taking the relative intensity measured for one polarization and dividing it by the relative intensity measured in the orthogonal polarization. For example the polarization contrast in the measured H state for the input state L measured at 0° normal incidence is given by Equation

2.

$$\text{Contrast of H for input L} = \frac{\langle H|\, M\, |L\rangle}{\langle V|\, M\, |L\rangle} = \frac{43.64}{48.56} = 0.90 \tag{2}$$

Table 7: Polarization contrast for the pentaprism at different pan angles

			Input					
			H	V	D	A	R	L
Measured	0°	H	79.48	0.01	0.63	1.03	0.87	0.90
		V	0.01	75.48	1.59	0.97	1.15	1.11
		D	1.40	0.74	44.05	0.02	0.63	1.29
		A	0.71	1.35	0.02	53.96	1.59	0.78
	7°	H	67.19	0.02	0.61	0.99	0.86	0.83
		V	0.01	58.09	1.63	1.01	1.16	1.21
		D	1.48	0.67	93.02	0.02	0.55	1.40
		A	0.68	1.49	0.01	46.69	1.81	0.72
	−7°	H	151.99	0.02	0.67	0.98	0.76	1.01
		V	0.01	63.63	1.50	1.02	1.32	0.99
		D	1.32	0.77	64.15	0.01	0.87	1.05
		A	0.76	1.30	0.02	101.18	1.15	0.95

Table 8: Polarization contrast for the pentaprism at different tilt angles

			Input					
			H	V	D	A	R	L
Measured	0°	H	56.1	0.0	0.7	1.0	0.9	0.9
		V	0.0	115.4	1.4	1.0	1.2	1.1
		D	1.2	0.8	35.2	0.0	0.9	1.5
		A	0.8	1.2	0.0	175.8	1.1	0.7
	−4°	H	116.7	0.0	1.1	0.7	0.9	0.9
		V	0.0	91.7	0.9	1.5	1.2	1.1
		D	0.8	1.2	102.1	0.0	0.7	1.4
		A	1.2	0.9	0.0	34.0	1.5	0.7
	4°	H	25.3	0.0	0.4	1.6	1.0	0.7
		V	0.0	29.5	2.3	0.6	1.0	1.4
		D	2.0	0.5	16.2	0.0	0.7	1.4
		A	0.5	2.1	0.1	38.3	1.5	0.7

Table 9: Polarization contrast for the periscope assembly at different pan angles

			Input					
			H	V	D	A	R	L
Measured	0°	H	0.0	87.9	1.4	0.8	0.9	1.2
		V	67.8	0.0	0.7	1.2	1.1	0.9
		D	0.7	1.4	0.0	91.6	1.3	0.7
		A	1.5	0.7	83.8	0.0	0.7	1.3
	2°	H	0.0	58.3	1.6	0.8	1.1	1.0
		V	90.2	0.0	0.6	1.3	0.9	1.0
		D	0.7	1.3	0.0	90.0	1.4	0.7
		A	1.4	0.8	54.9	0.0	0.7	1.4
	−2°	H	0.0	195.2	1.2	0.9	0.9	1.1
		V	102.7	0.0	0.8	1.2	1.1	0.9
		D	0.9	1.2	0.0	120.1	1.5	0.7
		A	1.2	0.9	72.0	0.0	0.7	1.5

Table 10: Polarization contrast for the periscope assembly at different tilt angles

			Input					
			H	V	D	A	R	L
Measured	0°	H	0.0	75.3	1.3	0.8	0.9	1.1
		V	103.2	0.0	0.8	1.3	1.1	0.9
		D	0.7	1.4	0.0	77.4	1.4	0.8
		A	1.5	0.7	93.7	0.0	0.7	1.3
	−4°	H	0.0	310.0	1.0	1.0	0.9	1.1
		V	215.3	0.0	1.0	1.0	1.1	0.9
		D	1.0	1.1	0.0	190.0	1.3	0.8
		A	1.1	0.9	172.1	0.0	0.7	1.3
	4°	H	0.0	29.5	1.9	0.6	0.9	1.2
		V	30.0	0.0	0.5	1.7	1.2	0.9
		D	0.5	2.1	0.0	41.1	1.6	0.6
		A	2.0	0.5	34.9	0.0	0.6	1.6

.3 Automated Method Data

The measurement data for each incoming angle was deemed to be too large to be presented in the appendix, so only the unitaries for each angle are given.

Table 11: straight through path compensation unitaries

Angle	Average Compensation Unitary
run 0.0	$\begin{pmatrix} -0.99996 + 0.002071i & 0.000984 + 0.00821i \\ -0.000984 + 0.00821i & -0.99996 - 0.002071i \end{pmatrix}$
run 0.1	$\begin{pmatrix} -0.99998 - 0.002367i & 0.00519 + 0.002316i \\ -0.00519 + 0.002316i & -0.99998 + 0.002367i \end{pmatrix}$
run 1.0	$\begin{pmatrix} -0.99996 + 0.006671i & 0.002115 + 0.005053i \\ -0.002115 + 0.005053i & -0.99996 - 0.006671i \end{pmatrix}$
run 1.1	$\begin{pmatrix} -0.99996 - 0.000744i & 0.002855 + 0.008615i \\ -0.002855 + 0.008615i & -0.99996 + 0.000744i \end{pmatrix}$

Table 12: Pentaprism compensation unitaries

Angle	Average Compensation Unitary
0° Pan 0° Tilt	$\begin{pmatrix} -0.99965 - 0.008334i & 0.018095 - 0.017391i \\ -0.018095 - 0.017391i & -0.99965 + 0.008334i \end{pmatrix}$
0° Pan 356° Tilt	$\begin{pmatrix} -0.99844 - 0.010572i & -0.053147 - 0.013373i \\ 0.053147 - 0.013373i & -0.99844 + 0.010572i \end{pmatrix}$
0° Pan 4° Tilt	$\begin{pmatrix} -0.99751 - 0.011257i & 0.067521 - 0.016819i \\ -0.067521 - 0.016819i & -0.99751 + 0.011257i \end{pmatrix}$
356° Pan 0° Tilt	$\begin{pmatrix} -0.99974 - 0.020391i & 0.004785 - 0.009589i \\ -0.004785 - 0.009589i & -0.99974 + 0.020391i \end{pmatrix}$
356° Pan 356° Tilt	$\begin{pmatrix} -0.99792 - 0.000404i & -0.050858 - 0.039519i \\ 0.050858 - 0.039519i & -0.99792 + 0.000404i \end{pmatrix}$
356° Pan 4° Tilt	$\begin{pmatrix} -0.9964 + 0.002562i & 0.071723 - 0.04503i \\ -0.071723 - 0.04503i & -0.9964 - 0.002562i \end{pmatrix}$
4° Pan 0° Tilt	$\begin{pmatrix} -0.99921 - 0.038232i & 0.0099 + 0.004441i \\ -0.0099 + 0.004441i & -0.99921 + 0.038232i \end{pmatrix}$
4° Pan 356° Tilt	$\begin{pmatrix} -0.99836 - 0.020104i & -0.034845 - 0.040637i \\ 0.034845 - 0.040637i & -0.99836 + 0.020104i \end{pmatrix}$
4° Pan 4° Tilt	$\begin{pmatrix} -0.99688 - 0.034012i & 0.069696 + 0.014704i \\ -0.069696 + 0.014704i & -0.99688 + 0.034012i \end{pmatrix}$

Table 13: Periscope assembly compensation unitaries

Angle	Average Compensation Unitary
0° Pan 0° Tilt	$\begin{pmatrix} 0.037702 - 0.030954i & 0.99571 + 0.078662i \\ -0.99571 + 0.078662i & 0.037702 + 0.030954i \end{pmatrix}$
0° Pan 357° Tilt	$\begin{pmatrix} 0.016114 + 0.03195i & -0.99593 - 0.082683i \\ 0.99593 - 0.082683i & 0.016114 - 0.03195i \end{pmatrix}$
0° Pan 3° Tilt	$\begin{pmatrix} 0.08614 - 0.048035i & 0.99332 + 0.059923i \\ -0.99332 + 0.059923i & 0.08614 + 0.048035i \end{pmatrix}$
357° Pan 0° Tilt	$\begin{pmatrix} 0.037207 - 0.024054i & 0.99714 + 0.061159i \\ -0.99714 + 0.061159i & 0.037207 + 0.024054i \end{pmatrix}$
357° Pan 357° Tilt	$\begin{pmatrix} 0.015753 + 0.055209i & -0.99533 - 0.07761i \\ 0.99533 - 0.07761i & 0.015753 - 0.055209i \end{pmatrix}$
357° Pan 3° Tilt	$\begin{pmatrix} 0.088755 - 0.029828i & 0.99504 + 0.033696i \\ -0.99504 + 0.033696i & 0.088755 + 0.029828i \end{pmatrix}$
3° Pan 0° Tilt	$\begin{pmatrix} -0.037035 - 0.004871i & -0.99268 - 0.11488i \\ 0.99268 - 0.11488i & -0.037035 + 0.004871i \end{pmatrix}$
3° Pan 357° Tilt	$\begin{pmatrix} 0.010717 + 0.063969i & -0.99379 - 0.090443i \\ 0.99379 - 0.090443i & 0.010717 - 0.063969i \end{pmatrix}$
3° Pan 3° Tilt	$\begin{pmatrix} 0.089165 - 0.035045i & 0.99143 + 0.088788i \\ -0.99143 + 0.088788i & 0.089165 + 0.035045i \end{pmatrix}$

Table 14: Single mirror compensation unitaries

Angle	Average Compensation Unitary
0° Pan 0° Tilt	$\begin{pmatrix} -0.20745 + 0.97648i & -0.019244 + 0.055506i \\ 0.019244 + 0.055506i & -0.20745 - 0.97648i \end{pmatrix}$
0° Pan 356° Tilt	$\begin{pmatrix} -0.20275 + 0.96826i & 0.033219 + 0.14236i \\ -0.033219 + 0.14236i & -0.20275 - 0.96826i \end{pmatrix}$
0° Pan 4° Tilt	$\begin{pmatrix} -0.19968 + 0.97971i & -0.010312 + 0.01378i \\ 0.010312 + 0.01378i & -0.19968 - 0.97971i \end{pmatrix}$
356° Pan 0° Tilt	$\begin{pmatrix} -0.17303 + 0.98189i & -0.008391 + 0.076677i \\ 0.008391 + 0.076677i & -0.17303 - 0.98189i \end{pmatrix}$
356° Pan 356° Tilt	$\begin{pmatrix} -0.17312 + 0.97534i & 0.038111 + 0.13148i \\ -0.038111 + 0.13148i & -0.17312 - 0.97534i \end{pmatrix}$
356° Pan 4° Tilt	$\begin{pmatrix} -0.16993 + 0.98527i & -0.005022 + 0.018627i \\ 0.005022 + 0.018627i & -0.16993 - 0.98527i \end{pmatrix}$
4° Pan 0° Tilt	$\begin{pmatrix} -0.23084 + 0.97002i & -0.047932 + 0.058959i \\ 0.047932 + 0.058959i & -0.23084 - 0.97002i \end{pmatrix}$
4° Pan 356° Tilt	$\begin{pmatrix} -0.2224 + 0.9642i & 0.011334 + 0.14395i \\ -0.011334 + 0.14395i & -0.2224 - 0.9642i \end{pmatrix}$
4° Pan 4° Tilt	$\begin{pmatrix} -0.22248 + 0.97487i & -0.00589 + 0.010002i \\ 0.00589 + 0.010002i & -0.22248 - 0.97487i \end{pmatrix}$

Table 15: Double mirror compensation unitaries

Angle	Average Compensation Unitary
0° Pan 0° Tilt	$\begin{pmatrix} -0.99554 - 0.086352i & 0.036027 + 0.012189i \\ -0.036027 + 0.012189i & -0.99554 + 0.086352i \end{pmatrix}$
0° Pan 356° Tilt	$\begin{pmatrix} -0.99517 - 0.092618i & -0.030646 - 0.010785i \\ 0.030646 - 0.010785i & -0.99517 + 0.092618i \end{pmatrix}$
0° Pan 4° Tilt	$\begin{pmatrix} -0.99239 - 0.090329i & 0.083194 + 0.009282i \\ -0.083194 + 0.009282i & -0.99239 + 0.090329i \end{pmatrix}$
356° Pan 0° Tilt	$\begin{pmatrix} -0.99691 - 0.06959i & 0.02424 - 0.027348i \\ -0.02424 - 0.027348i & -0.99691 + 0.06959i \end{pmatrix}$
356° Pan 356° Tilt	$\begin{pmatrix} -0.9946 - 0.094157i & -0.042546 - 0.010061i \\ 0.042546 - 0.010061i & -0.9946 + 0.094157i \end{pmatrix}$
356° Pan 4° Tilt	$\begin{pmatrix} -0.99148 - 0.092485i & 0.091165 - 0.010163i \\ -0.091165 - 0.010163i & -0.99148 + 0.092485i \end{pmatrix}$
4° Pan 0° Tilt	$\begin{pmatrix} -0.99708 - 0.066115i & 0.029035 - 0.024761i \\ -0.029035 - 0.024761i & -0.99708 + 0.066115i \end{pmatrix}$
4° Pan 356° Tilt	$\begin{pmatrix} -0.99591 - 0.084498i & -0.025496 - 0.019533i \\ 0.025496 - 0.019533i & -0.99591 + 0.084498i \end{pmatrix}$
4° Pan 4° Tilt	$\begin{pmatrix} -0.9928 - 0.086081i & 0.082576 + 0.010577i \\ -0.082576 + 0.010577i & -0.9928 + 0.086081i \end{pmatrix}$

.4 Automated Measurement Variance

The measurement data used for the automated beam steering characterization was based on the average of 10 measurements. As a way to gage the statistical relevance of these measurements, the standard deviation for each was calculated. Each dot in Figure 3 corresponds to the standard deviation of the 10 different measurements taken for each incoming angle, input polarization, and measurement polarization set.

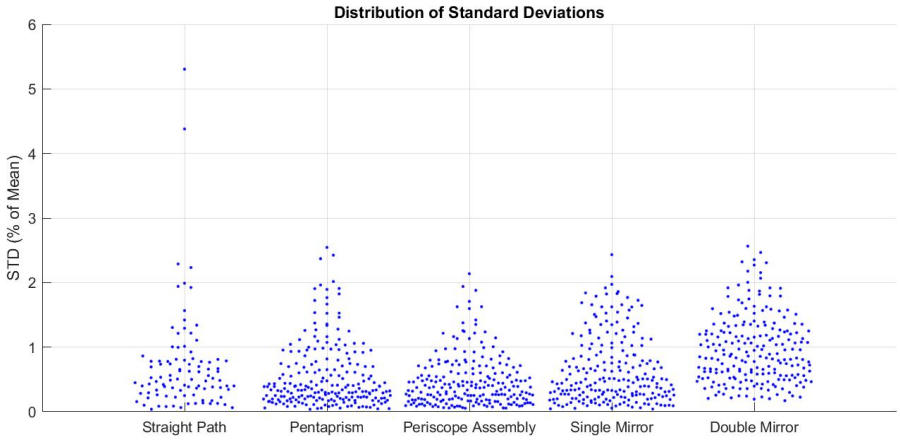

Figure 3: *Standard deviations of the automated measurement optical power data*

The values are given as a percentage of the measurement mean power as to show the values on the same relative scale. The horizontal data positions are not tied to any physical meaning. Horizontal position variance is only given to remove data point overlapping in the figure. The values corresponding to low measured powers skew the data slightly and give higher standard deviations in Figure 3. This is the case for the upper most two data points of the straight path measurements. Overall the standard deviations are relatively low, and the average of the measured powers holds as an accurate indication of the measured powers.

Stress Induced Birefringence Matlab Code

The following is the core script used to calculate the mechanical stress induced birefringence and QBER.

```
% Birefingance Calculater

%% Initiate Program

close all; clear all; clc; tic;    % clear all previous saved variables

addpath('supporting');

initiate;   % setup log files and colormaps
diary on

%% Parameters

saveFigs = true;    % set to true to save the figures
saveGif = false;

translationCompensation = false;

% The units in the file are Newton and Millimeter
%   the tensor elements are thus in units of MPa.
filename = 'supporting/WORF_FEM_CSV.csv';

% radius of calculation limmiter. only calculate points that exist
% withinin calcFract of the radius of the center of the object.
calcFract = 0.85; % # | cant be 1 because edge effect cause error / ...
    clipping

% scalle to stress by a constant value
stressScale = 1; % set to 1 for no effect

```

```
% cell sizes
cellsWide = 601  % # | coresponds to x,y directions should be odd so ...
    there is a center cell.
cellsHigh = 80   % # | coresponds to z direction

% To save preliminary generated matricies, and load them later, use the
% following parameters. The purpose of this would be to save time when
% using the same initial data and (large) cell sizes. loading may ...
    overwrite
% or conflict with somparameters, if paramerers disagrre with those ...
    in the
% loaded file.
artificialdata = 0; % do not use, currently broken

%% Variables

fs = 16;    % normally 12

l_v = 0.810; % um | the wavelength of the light in vacuum

material = 'mSiO2'; % currently limited material selection

vtilt = [0,1,5,10,15,20,25,30]; % deg | various angles of incomming ...
    beam tilt to loop over and calculate

%define input parameters for aperture telescope
aperture = 0.1  % m | 10,14,17,20 input beam / telescope diameter
pivot_l = 0.3   % m | location of pivot point of gimbal, behind window

% log parameters
fileID = fopen(statfile,'a');
if translationCompensation
    fprintf(fileID, ['Fixed centre aka translation compensation\n']);
else
    fprintf(fileID, ['Not fixed centre \n']);
end
fprintf(fileID, ['Wavelength: ',num2str(l_v*1000),'nm \n']);
fprintf(fileID, ['Aperture: ',num2str(aperture*100),'cm \n']);
fclose(fileID);

% estimat how long it will take on my computer
durration = 60+(638-60)*(cellsWide/100)^2*(cellsHigh/80)^2* ...
    length(vtilt)/8;      % seconds: this is assumed to work best with ...
    cellsHigh = 80
```

```
t = datetime;
disp('Current Time:')
disp(t)
disp('Estimated Completion Time:')
disp(t+seconds(durration))
disp(seconds(durration))

%% Define Materials

% define the mSiO2 material
if strcmp('mSiO2', material)

  nv = 1;   % # | index of refraction of vacuum

  % https://nvlpubs.nist.gov/nistpubs/jres/53/jresv53n3p185_A1b.pdf
  % ... https://refractiveindex.info/?shelf=glass&book=fused_silica&page=Malitson
  % n0: refractive index for fused silica (fused quartz, mSiO2)
  n0 = sqrt(0.6961663*l_v^2/(l_v^2-0.0684043^2)...
     + 0.4079426*l_v^2/(l_v^2-0.1162414^2)...
     + 0.8974794*l_v^2/(l_v^2-9.896161^2)+1);
  l_m = l_v/n0;

  % q: the 6x6 stress-optical coefficient matrix, and the values ... given below
  %  are used to create the matrix for mSiO2 at 546.38 nm. This ... values for
  %  q should be close to accurate for other wavelenghts aswell. It was
  %  hard to find wavelength specific values for some other wavelengths.

  q44 = 0; % Pa^-1 | this is assumed because it is not given in the ... data chart, and based on the distortion

  % interpolate for the wavelength
  lambda = [0.54638 0.43596 0.36512 0.25373]; % um | wavelength
  q11v = [0.33 0.22 0.11 -0.20]*1e-12; % Pa^-1
  q12v = [2.67 2.59 2.52 2.35]*1e-12; % Pa^-1

  q11 = interp1(lambda,q11v,l_v,'spline');
  q12 = interp1(lambda,q12v,l_v,'spline');

  % combine the idividual components of q to form the q matrix
  q = zeros(6);
  q(4:6,4:6) = eye(3)*q44;
```

```
108   q(1:3,1:3) = eye(3)*(q11-q12)+q12;
109 else
110   error('Currently only works with mSiO2')
111 end
112
113 % convert to si units
114 l_v = l_v*1e-6; % micrometers to meters
115 l_m = l_m*1e-6; % micrometers to meters
116
117 %% Create Birefringence Matrix
118
119 if artificialdata
120     disp('creating artificial stress data')
121 %             xStp = 170/cellsWide*0.003; % m
122 %             zStp = 11/cellsHigh*0.003; % m
123     xStp = 0.0032; % m, based on the data
124     zStp = xStp; % m
125 %             stress = create_slice(cellsWide,cellsHigh)*stressScale;
126     stress = create_slice(177,11)*stressScale;
127 else
128     Ms = csvread(filename,1,0); % read stress data
129
130     % fix the slice by filling holes that are in it
131     %   This makes the slice flat and uniform, whin in fact it is ...
          not, this is
132     %   an approximation and probably should be changed
133     layers = 11; % known value
134     [M3] = create_and_fill_matrix(Ms, layers);
135     [M3_1,M3_2,M3_3] = size(M3);
136
137     % convert to si units
138     M3(:,:,1:3) = M3(:,:,1:3)*1e-3; % milemeters to meters
139     M3(:,:,4:9) = M3(:,:,4:9)*1e6; % MPa to Pa
140
141 % rotate stress grid about x such that the primary axis is the z axis
142     rotM = xrot(pi/2);
143     for i = 1:M3_1
144         for j = 1:M3_2
145             M3(i,j,1:3) = rotM*reshape(M3(i,j,1:3),[3,1]);
146             M3(i,j,4:end) = trvo(rotM*trvo(M3(i,j,4:end))*rotM');
147         end
148     end
149
150     % scale the stress
```

```
151     stress = M3(:,:,4:9)*stressScale;
152     xStp = abs(diff(M3(1,1:2,1)));
153     zStp = abs(diff(M3(1:2,1,3)));
154 end
155 % Create a 3D grid of stress points from the 2d slice given.
156 [obj,xSpace,zSpace,cellsWide,cellsHigh] = ...
        createObjectFromSlice(stress,xStp,zStp,cellsWide,cellsHigh,statfile);
157
158 [Xq,Yq] = ...
        meshgrid((linspace(1,cellsWide,1000)-cellsWide/2)*xSpace,(linspace(1,cellsWide,1000
159 [Xp,Yp] = ...
        meshgrid(([1:cellsWide]-cellsWide/2)*xSpace,([1:cellsWide]-cellsWide/2)*xSpace);
160
161 %%%%%%%%%% Calculate Birefringance Matrix %%%%%%%%%%
162 biref_grid = zeros(cellsWide,cellsWide,cellsHigh,6);
163 for i = 1:cellsWide
164     if mod(i,50) == 0
165         fileID = fopen(statfile,'a');
166         fprintf(fileID, [datestr(now,'yyyy-mm-dd HH-MM-SS'),' ...
                ','calcBirefringanceMat: ', num2str(i), ...
                '/',num2str(cellsWide),'\n']);
167         fclose(fileID);
168     end
169     ii = (i-ceil(cellsWide/2))*xSpace;
170     for j = 1:cellsWide
171         jj = (j-ceil(cellsWide/2))*xSpace;
172
173         % if we are not within the calcFract radius, ignore the data ...
                points
174         if (sqrt(ii^2+jj^2) > calcFract*xSpace*floor(cellsWide/2)) ||...
175                 max(max(isnan(obj(i,j,:,:))))
176             biref_grid(i,j,:,:) = NaN;
177             continue
178         end
179
180         for k = 1:cellsHigh
181             stress_t=trvo(reshape(obj(i,j,k,:),[6 1]));
182             [V,D]=eig(stress_t); % V eigenvectors, D eigenvalue matrix
183             % biref: birefingance along principal access
184             biref = q*[D(1,1), D(2,2), D(3,3), 0, 0, 0]';
185             % rotate elipsoid back to axis of grid
186             % biref_grid: birefingance relative to the grid axis.
187             biref_grid(i,j,k,:) = trvo(V*trvo(biref)*V');
188         end
```

```
189     end
190 end
191 
192 QBER_avg_HV = zeros(size(vtilt));
193 QBER_avg_DA = zeros(size(vtilt));
194 QBER_avg_HV_cor = zeros(size(vtilt));
195 QBER_avg_DA_cor = zeros(size(vtilt));
196 unitaries = zeros(2,2,length(vtilt));
197 unitariesAperture = zeros(2,2,length(vtilt));
198 unitaries_og_app = zeros(2,2,length(vtilt));
199 
200 %% Calculate Polarization Distortion
201 
202 for v = 1:length(vtilt)
203 %     toc
204     tilt = vtilt(v);
205     theta = deg2rad(tilt);
206     theta_m = asin(sin(theta)/n0); % the angle in the medium
207     if translationCompensation
208         beam_displacement = -(xStp*11)*atan(theta_m); %focus on the ...
                very centre of the window
209     else
210         beam_displacement = atan(theta)*pivot_l; % lateral ...
                displacemnt of beam from centre of window
211     end
212     fig = 1;
213 
214     %%%%%%%%%% Account for Window Rotation %%%%%%%%%%
215 
216     radius_grid = floor(aperture/xSpace/2)+1;
217     pos_grid_y = floor(-beam_displacement/xSpace)+cellsWide/2;
218     pos_grid_x = floor(cellsWide/2);
219 
220     % one ray per surface cell
221 
222     horzShift_max = tan(theta_m)*zSpace*cellsHigh;
223     xNext = xSpace/2;
224     zNext = zSpace;
225 
226     lengthInBlock = zeros(cellsHigh,2);
227     for layer = 1:cellsHigh
228         horz = 1;
229         while zNext*tan(theta_m)>xNext % basically if we need to step ...
                in x
```

```
230             zChange = xNext/tan(theta_m);
231             lengthInBlock(layer,horz)=norm([xNext,zChange]);
232
233             zNext =zNext-xNext/tan(theta_m);
234             xNext = xSpace;
235             horz=horz+1;
236         end
237         % if the while fails, that means we need to step in z
238         xChange=zNext*tan(theta_m);
239         lengthInBlock(layer,horz)=norm([xChange,zNext]);
240         xNext = xNext-xChange;
241         zNext = zSpace;
242     end
243
244     temp = size(lengthInBlock); shiftedMax =temp(2); temp = [];% ...
        clear temp;
245
246     % calculated the rotated version of birefingance
247     gamma_grid=zeros(cellsWide,cellsWide,cellsHigh); % gamma, ...
        retardance phase
248     M_grid_rotated=zeros(cellsWide,cellsWide,2,2); % Jones matrix for ...
        each group
249     J_block = zeros(cellsWide,cellsWide,cellsHigh,2,2);
250     J_ray = zeros(cellsHigh,2,2);
251     biref_principle = zeros(cellsWide,cellsWide,cellsHigh,6);
252
253     B0=1/n0^2; % defince B0
254     for i = 1:cellsWide
255         if mod(i,50) == 0
256             fileID = fopen(statfile,'a');
257             fprintf(fileID, [datestr(now,'yyyy-mm-dd HH-MM-SS'),' ...
                ',num2str(vtilt(v)),' ','calcBirefringanceRot: ', ...
                num2str(i), '/',num2str(cellsWide),'\n']);
258             % fprintf(fileID,'%6.2f %12.8f\r\n',A);
259             fclose(fileID);
260         end
261         ii = (i-ceil(cellsWide/2))*xSpace;
262         for j = 1:cellsWide
263             jj = (j-ceil(cellsWide/2))*xSpace;
264
265             % if we are not within the calcFract radius, ignore the ...
                data points
266             if ((sqrt(ii^2+jj^2) > ...
                calcFract*xSpace*floor(cellsWide/2)) ||...
```

```
267                     (sqrt((ii+horzShift_max)^2+jj^2) > ...
                            xSpace*floor(cellsWide/2)))
268                 M_grid_rotated(i,j,:,:) = NaN;
269                 gamma_grid(i,j,:)=NaN;
270                 J_block(i,j,:,:,:)=NaN;
271                 continue
272             end
273
274             M_grid_rotated(i,j,:,:)=eye(2);
275             g=0; % 'global' shift
276             for k = 1:cellsHigh
277                 for s = 0:(shiftedMax-1)% 'local' shift
278                     L = lengthInBlock(k,s+1);
279                     if 0 ~= L
280                         biref_rot = ...
                                trvo(xrot(theta_m)*trvo(biref_grid(i,j,k,:))*xrot(theta_m)'
281
282                         gamma = ...
                                1/2*atan2(2*biref_rot(6),(biref_rot(1) - ...
                                biref_rot(2))); % i think my x and y might ...
                                be switched, which makes things interesting
283                         gamma_grid(i,j,k) = gamma; % just to save it ...
                                for later
284
285                         biref_principle(i,j,k,:) = trvo(zrot(-gamma)...
286                             *trvo(biref_rot)...
287                             *zrot(-gamma)');
288
289                         % refractive index differential for beam ...
                                along z axis
290                         Δ_n1 = -1/2*n0^3*biref_principle(i,j,k,1);
291                         Δ_n2 = -1/2*n0^3*biref_principle(i,j,k,2);
292
293                         % phase change for each axis
294                         del_1 = 2*pi*Δ_n1*L/l_m;
295                         del_2 = 2*pi*Δ_n2*L/l_m;
296
297                         % compute Jones matrices
298                         J = [exp(1i*del_1) 0; 0 exp(1i*del_2)];
299                         R = [cos(-gamma) -sin(-gamma); sin(-gamma) ...
                                cos(-gamma)];
300                         M_grid_rotated(i,j,:,:) = ...
                                R'*J*R*reshape(M_grid_rotated(i,j,:,:),[2,2]);
301
```

```
302                         if 0 ≠ s
303                             g = g+1;
304                         end
305                         if (i==ceil(pos_grid_y) && ...
                                j==ceil(pos_grid_x)) %????? choose centre
306                             J_ray(k,:,:)=R'*J*R;
307                         end
308                     end
309                 end
310                 J_block(i,j,k,:,:) = M_grid_rotated(i,j,:,:);
311             end
312         end
313     end
314
315     %%%%%%%%%% Calculate Retardance Summation %%%%%%%%%%
316
317     retardance_sum_rotated=zeros(cellsWide,cellsWide,2);
318     for i = 1:cellsWide
319         if mod(i,50) == 0
320             fileID = fopen(statfile,'a');
321             fprintf(fileID, [datestr(now,'yyyy-mm-dd HH-MM-SS'),' ...
                    ',num2str(vtilt(v)),' ','calcRetardanceSum: ', ...
                    num2str(i), '/',num2str(cellsWide),'\n']);
322             % fprintf(fileID,'%6.2f %12.8f\r\n',A);
323             fclose(fileID);
324         end
325         for j = 1:cellsWide
326             JM = reshape(M_grid_rotated(i,j,:,:),2,2);
327             JM1 = real(-1i*log(JM(1,1)));
328             JM2 = real(-1i*log(JM(2,2)));
329             retardance_sum_rotated(i,j,1) = atan2(JM2,JM1);
330             retardance_sum_rotated(i,j,2) = JM1-JM2;
331         end
332     end
333
334     %%%%%%%%%% Calculate QBER %%%%%%%%%%
335
336     % Define Input States
337     hVec = [1;0];               % Horizontal Polarization
338     vVec = [0;1];               % Vertical  Polarization
339     dVec = 1/sqrt(2)*[1;1];     % Diagonal Polarization
340     aVec = 1/sqrt(2)*[1;-1];    % Anti-diagonal Polarization
341     rVec = 1/sqrt(2)*[1;-1i];   % Right Circular Polarization
342     lVec = 1/sqrt(2)*[1;1i];    % Left Circular Polarization
```

```
343
344     % Define QBER Matrix Holders For Total Window
345     QBER_grid_rotated=zeros(cellsWide,cellsWide,1);
346     QBER_grid_rot_HV=zeros(cellsWide,cellsWide,1);
347     QBER_grid_rot_DA=zeros(cellsWide,cellsWide,1);
348     QBER_grid_rot_H=zeros(cellsWide,cellsWide,1);
349     QBER_grid_rot_V=zeros(cellsWide,cellsWide,1);
350     QBER_grid_rot_D=zeros(cellsWide,cellsWide,1);
351     QBER_grid_rot_A=zeros(cellsWide,cellsWide,1);
352     for i = 1:cellsWide
353         if mod(i,50) == 0
354             fileID = fopen(statfile,'a');
355             fprintf(fileID, [datestr(now,'yyyy-mm-dd HH-MM-SS'),' ...
                    ',num2str(vtilt(v)),' ','calcQBERRotGrid: ', ...
                    num2str(i), '/',num2str(cellsWide),'\n']);
356             fclose(fileID);
357         end
358         for j = 1:cellsWide
359             JM = reshape(M_grid_rotated(i,j,:,:),2,2);
360             QBER_H=(vVec'*JM*hVec);
361             QBER_V=(hVec'*JM*vVec);
362             QBER_D=(aVec'*JM*dVec);
363             QBER_A=(dVec'*JM*aVec);
364             QBER_grid_rotated(i,j) = ...
                    (QBER_H*QBER_H'+QBER_V*QBER_V'+QBER_D*QBER_D'+QBER_A*QBER_A')/4;
365             QBER_grid_rot_HV(i,j) = (QBER_H*QBER_H'+QBER_V*QBER_V')/2;
366             QBER_grid_rot_DA(i,j) = (QBER_D*QBER_D'+QBER_A*QBER_A')/2;
367             QBER_grid_rot_H(i,j) = QBER_H*QBER_H';
368             QBER_grid_rot_V(i,j) = QBER_V*QBER_V';
369             QBER_grid_rot_D(i,j) = QBER_D*QBER_D';
370             QBER_grid_rot_A(i,j) = QBER_A*QBER_A';
371         end
372     end
373
374     QBER_block = zeros(cellsWide,cellsWide,cellsHigh);
375     for i = 1:cellsWide
376         if mod(i,50) == 0
377             fileID = fopen(statfile,'a');
378             fprintf(fileID, [datestr(now,'yyyy-mm-dd HH-MM-SS'),' ...
                    ',num2str(vtilt(v)),' ','calcQBERBlock: ', num2str(i), ...
                    '/',num2str(cellsWide),'\n']);
379             fclose(fileID);
380         end
381         for j = 1:cellsWide
```

```
382             for k = 1:cellsHigh
383                 JM = reshape(J_block(i,j,k,:,:),2,2);
384                 QBER_H=(vVec'*JM*hVec);
385                 QBER_V=(hVec'*JM*vVec);
386                 QBER_D=(aVec'*JM*dVec);
387                 QBER_A=(dVec'*JM*aVec);
388                 QBER_block(i,j,k) = ...
                        real(QBER_H*QBER_H'+QBER_V*QBER_V'+QBER_D*QBER_D'+QBER_A*QBER_A')/4
389             end
390         end
391     end
392
393     %%%%%%%%%% Calculate Compensation Unitary %%%%%%%%%%
394
395     % The poln.exe function is a program that was developed to solved for
396     % the optimal compensation matrix. Physically the compensation matrix
397     % would be implimented via quarter and half wavelapte.
398
399     output = [hVec'; dVec'; vVec'; aVec'];
400     % create the data matrix to feed poln.exe
401     polnFeedMat = zeros(6,4);
402     for i = 1:cellsWide
403         if mod(i,50) == 0
404             fileID = fopen(statfile,'a');
405             fprintf(fileID, [datestr(now,'yyyy-mm-dd HH-MM-SS'),' ...
                    ',num2str(vtilt(v)),' ','createPolnFeed1: ', ...
                    num2str(i), '/',num2str(cellsWide),'\n']);
406             fclose(fileID);
407         end
408         for j = 1:cellsWide
409             JM = reshape(M_grid_rotated(i,j,:,:),2,2);
410             if ~isnan(JM)
411                 input = [JM*hVec, JM*vVec, JM*dVec, JM*aVec, JM*rVec, ...
                        JM*lVec];
412                 for m = 1:6
413                     for n = 1:4
414                         measured = output(n,:)*input(:,m);
415                         polnFeedMat(m,n) = ...
                                polnFeedMat(m,n)+measured*measured';
416                     end
417                 end
418             end
419         end
420     end
```

```
421
422     % turn polnFeedMat from a sum of probabilities to counts
423     polnFeedMat = round(polnFeedMat*1e8/max(max(polnFeedMat)));
424     polnFeedStr = num2str(polnFeedMat);
425
426     % create document to feed poln.exe
427     in1 = '0 0 0 0 -4';
428     in2 = polnFeedStr(1,:);
429     in3 = polnFeedStr(2,:);
430     in4 = polnFeedStr(3,:);
431     in5 = polnFeedStr(4,:);
432     in6 = polnFeedStr(5,:);
433     in7 = polnFeedStr(6,:);
434     polnFeed = ...
            [in1,'\n',in2,'\n',in3,'\n',in4,'\n',in5,'\n',in6,'\n',in7];
435     fileID = fopen('polnFeed.txt','w');
436     fprintf(fileID,polnFeed);
437     fclose(fileID);
438
439     % run poln.exe with the data to calculate the optimal unitary to ...
            compensate
440     % for the distortion
441     [status2,cmdout2]=system('poln.exe < polnFeed.txt');
442     strStart = 'Modelled wave plates unitary: ';
443     strEnd = 'Predicted output density matrix (H): ';
444     idxStart = strfind(cmdout2,strStart);
445     idxEnd = strfind(cmdout2,strEnd);
446     unitary = ...
            round(str2num(cmdout2(idxStart+length(strStart):idxEnd-2)),6);
447     unitaries(:,:,v) = unitary;
448     % unitary = ...
            round(str2num(cmdout2(idxStart+length(strStart):idxEnd-2)));
449
450     % calculate combined QBER within the input aperture
451     [X_mask,Y_mask]=meshgrid([1:cellsWide],[1:cellsWide]);
452     Z_mask = sqrt((X_mask-pos_grid_x).^2 + (Y_mask-pos_grid_y).^2); % ...
            this is an error but other things have compensated for it
453     mask_grid=zeros(cellsWide)+NaN;
454     mask_grid(Z_mask<=radius_grid)=1;
455     QBER_HV_cutout=QBER_grid_rot_HV.*mask_grid;
456     QBER_DA_cutout=QBER_grid_rot_DA.*mask_grid;
457     QBER_avg_HV(v)=nanmean(nonzeros(QBER_HV_cutout));
458     QBER_avg_DA(v)=nanmean(nonzeros(QBER_DA_cutout));
459
```

```
460     output = [hVec'; dVec'; vVec'; aVec'];
461
462     % create the data matrix to feed poln.exe
463     polnFeedMatAperture = zeros(6,4);
464     for i = 1:cellsWide
465         if mod(i,50) == 0
466             fileID = fopen(statfile,'a');
467             fprintf(fileID, [datestr(now,'yyyy-mm-dd HH-MM-SS'),' ...
                    ',num2str(vtilt(v)),' ','createPolnFeed2: ', ...
                    num2str(i), '/',num2str(cellsWide),'\n']);
468             % fprintf(fileID,'%6.2f %12.8f\r\n',A);
469             fclose(fileID);
470         end
471         for j = 1:cellsWide
472             JM = reshape(M_grid_rotated(i,j,:,:),2,2);
473             if (~isnan(JM) & ~isnan(mask_grid(i,j))) % needs to be ...
                    single &
474                 input = [JM*hVec, JM*vVec, JM*dVec, JM*aVec, JM*rVec, ...
                        JM*lVec];
475                 for m = 1:6
476                     for n = 1:4
477                         measured = output(n,:)*input(:,m);
478                         polnFeedMatAperture(m,n) = ...
                                polnFeedMatAperture(m,n)+measured*measured';
479                     end
480                 end
481             end
482         end
483     end
484
485     % turn polnFeedMat from a sum of probabilities to counts
486     polnFeedMatAperture = ...
            round(polnFeedMatAperture*1e8/max(max(polnFeedMatAperture)));
487     polnFeedStrAperture = num2str(polnFeedMatAperture);
488
489     % create document to feed poln.exe
490     in1 = '0 0 0 0 -4';
491     in2 = polnFeedStrAperture(1,:);
492     in3 = polnFeedStrAperture(2,:);
493     in4 = polnFeedStrAperture(3,:);
494     in5 = polnFeedStrAperture(4,:);
495     in6 = polnFeedStrAperture(5,:);
496     in7 = polnFeedStrAperture(6,:);
497     polnFeedAperture = ...
```

```
        [in1,'\n',in2,'\n',in3,'\n',in4,'\n',in5,'\n',in6,'\n',in7];
498     fileID = fopen('polnFeedAperture.txt','w');
499     fprintf(fileID,polnFeedAperture);
500     fclose(fileID);
501
502     % run poln.exe with the data to calucate the optimal unitary to ...
            compensate
503     % for the distortion
504     [status2,cmdout2]=system('poln.exe < polnFeedAperture.txt');
505     strStart = 'Modelled wave plates unitary: ';
506     strEnd = 'Predicted output density matrix (H): ';
507     idxStart = strfind(cmdout2,strStart);
508     idxEnd = strfind(cmdout2,strEnd);
509     unitaryAperture = ...
            round(str2num(cmdout2(idxStart+length(strStart):idxEnd-2)),6);
510     unitariesAperture(:,:,v) = unitaryAperture;
511
512     % it should be zero, so if it is not, let us know
513     if max(max(max(abs(biref_principle(:,:,:,6)))))>eps
514          warning('max(max(max(abs(biref_principle(:,:,:,6)))))>eps')
515          warning(num2str(max(max(max(abs(biref_principle(:,:,:,6)))))))
516     end
517
518     %%%%%%%%%% Compensate with Aperture Unitary %%%%%%%%%%
519
520     QBER_grid_rot_HV_cor=zeros(cellsWide,cellsWide,1)+NaN;
521     QBER_grid_rot_DA_cor=zeros(cellsWide,cellsWide,1)+NaN;
522     for i = 1:cellsWide
523         if mod(i,50) == 0
524             fileID = fopen(statfile,'a');
525             fprintf(fileID, [datestr(now,'yyyy-mm-dd HH-MM-SS'),' ...
                    ',num2str(vtilt(v)),' ','compWithAppUni: ', ...
                    num2str(i), '/',num2str(cellsWide),'\n']);
526             % fprintf(fileID,'%6.2f %12.8f\r\n',A);
527             fclose(fileID);
528         end
529         for j = 1:cellsWide
530             if (~isnan(mask_grid(i,j)))
531                 JM = ...
                        unitaryAperture*reshape(M_grid_rotated(i,j,:,:),2,2);
532                 QBER_H=(vVec'*JM*hVec);
533                 QBER_V=(hVec'*JM*vVec);
534                 QBER_D=(aVec'*JM*dVec);
535                 QBER_A=(dVec'*JM*aVec);
```

```
536                 QBER_grid_rot_HV_cor(i,j) = ...
                        (QBER_H*QBER_H'+QBER_V*QBER_V')/2;
537                 QBER_grid_rot_DA_cor(i,j) = ...
                        (QBER_D*QBER_D'+QBER_A*QBER_A')/2;
538             end
539         end
540     end
541
542     QBER_avg_HV_cor(v)=nanmean(nonzeros(QBER_grid_rot_HV_cor));
543     QBER_avg_DA_cor(v)=nanmean(nonzeros(QBER_grid_rot_DA_cor));
544
545
546     og_app_un = ...
          reshape(nanmean(nanmean(mask_grid.*M_grid_rotated(:,:,:,:))),2,2); ...
          % fast version
547
548     unitaries_og_app(:,:,v) = og_app_un;
549 end
550
551 diary off
```

Beam Steering Matlab Code

The following is the core function used to implement beam reflections and refractions.

```
function [k1,s0,s1,p0,p1,cos_theta_i,J] = reflect_refract(k0,d1,n0,n1)
    % ray_reflection(k0,d1,n0,n1)=[k1,s0,s1,p0,p1,cos_theta_i,J]
    % calculates parameters for a ray
    % reflected from a surface defined by d1 (normal vector pointing ...
       into surface)
    % procudces the (3x3 matrix) jones matrix for
    % ray reflection on a surface, where beam is incident at the ...
       angle theta from the surface nforma,
    % beam k-vector: input beam k0, exit beam  k1,
    % s-polarization vectors: s0 input,  s1 output,
    % p-polarization vectors: p0 input, p1 output.
    % entering in a medium with refractive index n0,
    % reflected from medium with refractive index n1.
    % todo, there can be an issue it the surface is definded facing the
    % opposite direction (-ve) we should be able to redefine this ...
       such that
    % it uses the incoming beam direction and always is the right ...
       direction
    % maybe use the sign of the dot product of the normal and the ray

    d1=d1/norm(d1);     % surface normal
    k0 = k0/norm(k0);   % incident light

    kr=k0-2*d1.*dot(d1,k0); %reflected beam direction

    r = n0/n1;
    c = -dot(d1,k0);
    kt = r*k0 + (r*c - sqrt(1-r^2*(1-c^2)))*d1; % transmitted beam ...
       direction

    % incident angle from surface normal
```

```
27      cos_theta_i = abs(dot(d1,k0));
28      theta_i = acos(cos_theta_i);
29
30      % snell's law
31      sin_theta_t = real(sin(theta_i)*n0/n1);
32      cos_theta_t = sqrt(1 - sin_theta_t.^2);
33      % Fresnel Coefficients ...
           https://en.wikipedia.org/wiki/Fresnel_equations
34      rs = (n0*cos_theta_i - n1*cos_theta_t)./(n0*cos_theta_i + ...
           n1*cos_theta_t);
35      rp = (n1*cos_theta_i - n0*cos_theta_t)./(n0*cos_theta_t + ...
           n1*cos_theta_i);
36      ts = (2*n0*cos_theta_i)./(n0*cos_theta_i+n1*cos_theta_t);
37      tp = (2*n0*cos_theta_i)./(n1*cos_theta_i+n0*cos_theta_t);
38
39      Rs = abs(rs).^2;
40      Rp = abs(rp).^2;
41      R_eff = real(Rs + Rp)/2;
42
43      Ts = (n1*cos_theta_t)/(n0*cos_theta_i)*abs(ts).^2;
44      Tp = (n1*cos_theta_t)/(n0*cos_theta_i)*abs(tp).^2;
45      T_eff = real(Ts + Tp)/2;
46
47
48      if T_eff > R_eff    % transmission
49          J = [ts 0 0; 0 tp  0; 0 0 1]; % Jones Matrix
50          k1 = kt;
51      else                % reflection
52          J = [rs 0 0; 0 rp  0; 0 0 1]; % Jones Matrix
53          k1 = kr;
54      end
55
56      % incident and exiting s and p vectors
57      s0=cross(k0,k1)/norm(cross(k0,k1)); %defintion from paper 2011 / ...
           Vol. 50, No. 18 / APPLIED OPTICS
58      p0=cross(k0,s0);
59      s1=s0;
60      p1=cross(k1,s1);
61  end
```